



Universiteit Gent  
Faculteit Wetenschappen  
Vakgroep Fysica en Sterrenkunde

<sup>2</sup> No title yet

<sup>3</sup> No sub-title neither, obviously...

---

<sup>4</sup> Alexis Fagot

5



Thesis to obtain the degree of  
Doctor of Philosophy in Physics  
Academic years 2012-2017





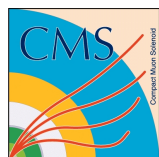


Universiteit Gent  
Faculteit Wetenschappen  
Vakgroep Fysica en Sterrenkunde

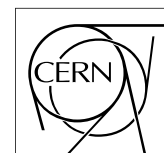
Promotoren: Dr. Michael Tytgat  
Prof. Dr. Dirk Ryckbosch

Universiteit Gent  
Faculteit Wetenschappen  
Vakgroep Fysica en Sterrenkunde  
Proeftuinstraat 86, B-9000 Gent, België  
Tel.: +32 9 264.65.28  
Fax.: +32 9 264.66.97

17



Thesis to obtain the degree of  
Doctor of Philosophy in Physics  
Academic years 2012-2017





## Acknowledgements

<sup>19</sup> Ici on remerciera tous les gens que j'ai pu croiser durant cette aventure et qui m'ont permis de passer  
<sup>20</sup> un bon moment

<sup>21</sup> *Gent, ici la super date de la mort qui tue de la fin d'écriture*  
<sup>22</sup> *Alexis Fagot*



# Table of Contents

24	<b>Acknowledgements</b>	i
25	<b>Nederlandse samenvatting</b>	xvii
26	<b>English summary</b>	xix
27	<b>1 Introduction</b>	1-1
28	1.1 A story of High Energy Physics . . . . .	1-1
29	1.2 Organisation of this study . . . . .	1-1
30	<b>2 Investigating the TeV scale</b>	2-1
31	2.1 The Standard Model of Particle Physics . . . . .	2-1
32	2.2 The Large Hadron Collider and the Compact Muon Solenoid . . . . .	2-1
33	2.3 Muon Phase-II Upgrade . . . . .	2-1
34	<b>3 Amplification processes in gaseous detectors</b>	3-1
35	3.1 Signal formation . . . . .	3-1
36	3.2 Gas transport parameters . . . . .	3-1
37	<b>4 Resistive Plate Chambers</b>	4-1
38	4.1 Principle . . . . .	4-1
39	4.2 Rate capability of Resistive Plate Chambers . . . . .	4-3
40	4.2.1 Operation modes . . . . .	4-4
41	4.3 High time resolution . . . . .	4-5
42	4.3.1 Electron drift velocity . . . . .	4-5
43	4.4 Resistive Plate Chambers at CMS . . . . .	4-5
44	4.4.1 Overview . . . . .	4-5
45	4.4.2 The present RPC system . . . . .	4-5
46	4.4.3 Pulse processing of CMS RPCs . . . . .	4-6
47	<b>5 Longevity studies and Consolidation of the present CMS RPC subsystem</b>	5-1
48	5.1 Testing detectors under extreme conditions . . . . .	5-1
49	5.1.1 The Gamma Irradiation Facilities . . . . .	5-3
50	5.1.1.1 GIF . . . . .	5-3
51	5.1.1.2 GIF++ . . . . .	5-5
52	5.2 Preliminary tests at GIF . . . . .	5-7
53	5.2.1 Resistive Plate Chamber test setup . . . . .	5-7
54	5.2.2 Data Acquisition . . . . .	5-9
55	5.2.3 Geometrical acceptance of the setup layout to cosmic muons . . . . .	5-9
56	5.2.3.1 Description of the simulation layout . . . . .	5-10
57	5.2.3.2 Simulation procedure . . . . .	5-12

---

58	5.2.3.3	Results . . . . .	5-13
59	5.2.4	Photon flux at GIF . . . . .	5-13
60	5.2.4.1	Expectations from simulations . . . . .	5-13
61	5.2.4.2	Dose measurements . . . . .	5-18
62	5.2.5	Results and discussions . . . . .	5-19
63	5.3	Longevity tests at GIF++ . . . . .	5-20
64	5.3.1	Description of the Data Acquisition . . . . .	5-23
65	5.3.2	RPC current, environmental and operation parameter monitoring . . . . .	5-24
66	5.3.3	Measurement procedure . . . . .	5-25
67	5.3.4	Longevity studies results . . . . .	5-25
68	<b>6</b>	<b>Investigation on high rate RPCs</b>	<b>6-1</b>
69	6.1	Rate limitations and ageing of RPCs . . . . .	6-1
70	6.1.1	Low resistivity electrodes . . . . .	6-1
71	6.1.2	Low noise front-end electronics . . . . .	6-1
72	6.2	Construction of prototypes . . . . .	6-1
73	6.3	Results and discussions . . . . .	6-1
74	<b>7</b>	<b>Conclusions and outlooks</b>	<b>7-1</b>
75	7.1	Conclusions . . . . .	7-1
76	7.2	Outlooks . . . . .	7-1
77	<b>A</b>	<b>A data acquisition software for CAEN VME TDCs</b>	<b>A-1</b>
78	A.1	GIF++ DAQ file tree . . . . .	A-1
79	A.2	Usage of the DAQ . . . . .	A-2
80	A.3	Description of the readout setup . . . . .	A-3
81	A.4	Data read-out . . . . .	A-3
82	A.4.1	V1190A TDCs . . . . .	A-4
83	A.4.2	DataReader . . . . .	A-6
84	A.4.3	Data quality flag . . . . .	A-10
85	A.5	Communications . . . . .	A-12
86	A.5.1	V1718 USB Bridge . . . . .	A-13
87	A.5.2	Configuration file . . . . .	A-13
88	A.5.3	WebDCS/DAQ intercommunication . . . . .	A-17
89	A.5.4	Example of inter-process communication cycle . . . . .	A-18
90	A.6	Software export . . . . .	A-18
91	<b>B</b>	<b>Details on the offline analysis package</b>	<b>B-1</b>
92	B.1	GIF++ Offline Analysis file tree . . . . .	B-1
93	B.2	Usage of the Offline Analysis . . . . .	B-2
94	B.2.1	Output of the offline tool . . . . .	B-3
95	B.2.1.1	ROOT file . . . . .	B-3
96	B.2.1.2	CSV files . . . . .	B-5
97	B.3	Analysis inputs and information handling . . . . .	B-6
98	B.3.1	Dimensions file and IniFile parser . . . . .	B-6
99	B.3.2	TDC to RPC link file and Mapping . . . . .	B-7
100	B.4	Description of GIF++ setup within the Offline Analysis tool . . . . .	B-9
101	B.4.1	RPC objects . . . . .	B-9
102	B.4.2	Trolley objects . . . . .	B-10
103	B.4.3	Infrastructure object . . . . .	B-11

---

104	B.5 Handeling of data . . . . .	B-12
105	B.5.1 RPC hits . . . . .	B-13
106	B.5.2 Clusters of hits . . . . .	B-14
107	B.6 DAQ data Analysis . . . . .	B-15
108	B.6.1 Determination of the run type . . . . .	B-16
109	B.6.2 Beam time window calculation for efficiency runs . . . . .	B-17
110	B.6.3 Data loop and histogram filling . . . . .	B-18
111	B.6.4 Results calculation . . . . .	B-19
112	B.6.4.1 Rate normalisation . . . . .	B-19
113	B.6.4.2 Rate and activity . . . . .	B-21
114	B.6.4.3 Strip masking tool . . . . .	B-23
115	B.6.4.4 Output CSV files filling . . . . .	B-25
116	B.7 Current data Analysis . . . . .	B-29



# List of Figures

117

118	2.1	Absorbed dose in the CMS cavern after an integrated luminosity of 3000 fb. R is the transverse distance from the beamline and Z is the distance along the beamline from the Interaction Point at Z=0. . . . .	2-2
119			
120			
121	2.2	A quadrant of the muon system, showing DTs (yellow), RPCs (light blue), and CSCs (green). The locations of new forward muon detectors for Phase-II are contained within the dashed box and indicated in red for GEM stations (ME0, GE1/1, and GE2/1) and dark blue for improved RPC (iRPC) stations (RE3/1 and RE4/1). . . . .	2-2
122			
123			
124			
125	2.3	RMS of the multiple scattering displacement as a function of muon $p_T$ for the proposed forward muon stations. All of the electromagnetic processes such as bremsstrahlung and magnetic field effect are included in the simulation. . . . .	2-3
126			
127			
128	4.1	Different phases of the avalanche development in the RPC gas volume subjected to a constant electric field $E_0$ . a) An avalanche is initiated by the primary ionisation caused by the passage of a charged particle through the gas volume. b) Due to its growing size, the avalanche starts to locally influence the electric field. c) The electrons, lighter than the cations reach the anode first. d) The ions reach the cathode. While the charges have not recombined, the electric field in the small region around the avalanche stays affected and locally blind the detector. . . . .	4-2
129			
130			
131			
132			
133			
134			
135	4.2	Movement of the charge carriers in an RPC. Figure 4.2a Voltage across an RPC whose electrode have a relative permittivity of 5 at the moment the tension s applied. Figure 4.2b After the charge carriers moved, the electrodes are charged and there is no voltage drop over the electrodes anymore. The full potential is applied on the gas gap only. Figure 4.2c The streamer discharge initiated by a charged particle transports electrons and cations towards the anode and cathode respectively. . . . .	4-4
136			
137			
138			
139			
140			
141	4.3	Signals from the RPC strips are shaped by the FEE described on Figure 4.3a. Output LVDS signals are then read-out by a TDC module connected to a computer or converted into NIM and sent to scalers. Figure 4.3b describes how these converted signals are put in coincidence with the trigger. . . . .	4-7
142			
143			
144			
145	4.4	Description of the principle of a CFD. A comparison of threshold triggering (left) and constant fraction triggering (right) is shown in Figure 4.4a. Constant fraction triggering is obtained thanks to zero-crossing technique as explained in Figure 4.4b. The signal arriving at the input of the CFD is split into three components. A first one is delayed and connected to the inverting input of a first comparator. A second component is connected to the noninverting input of this first comparator. A third component is connected to the noninverting input of another comparator along with a threshold value connected to the inverting input. Finally, the output of both comparators is fed through an AND gate. . . . .	4-8
146			
147			
148			
149			
150			
151			
152			
153			

154	5.1	(5.1a) Extrapolation from 2016 data of single hit rate per unit area in the barrel 155 region. (5.1b) Extrapolation from 2016 data of single hit rate per unit area in the 156 endcap region. . . . .	5-2
157	5.2	Background Fluka simulation compared to 2016 Data at $L = 10^{34} \text{ cm}^{-2} \cdot \text{s}^{-1}$ in 158 the fourth endcap disk region. A mismatch in between simulation and data can be 159 observed. [To be understood.] . . . . .	5-3
160	5.3	Layout of the test beam zone called X5c GIF at CERN. Photons from the radioactive 161 source produce a sustained high rate of random hits over the whole area. The zone is 162 surrounded by 8 m high and 80 cm thick concrete walls. Access is possible through 163 three entry points. Two access doors for personnel and one large gate for material. 164 A crane allows installation of heavy equipment in the area. . . . .	5-4
165	5.4	$^{137}\text{Cs}$ decays by $\beta^-$ emission to the ground state of $^{137}\text{Ba}$ (BR = 5.64%) and via the 166 662 keV isomeric level of $^{137}\text{Ba}$ (BR = 94.36%) whose half-life is 2.55 min. . . . .	5-5
167	5.5	Floor plan of the GIF++ facility. When the facility downstream of the GIF++ takes 168 electron beam, a beam pipe is installed along the beam line (z-axis). The irradiator 169 can be displaced laterally (its center moves from $x = 0.65$ m to 2.15 m), to increase 170 the distance to the beam pipe. . . . .	5-5
171	5.6	Simulated unattenuated current of photons in the xz plane (Figure 5.6a) and yz plane 172 (Figure 5.6b) through the source at $x = 0.65$ m and $y = 0$ m. With angular correction 173 filters, the current of 662 keV photons is made uniform in xy planes. . . . .	5-6
174	5.7	Description of the RPC setup. Dimensions are given in mm. A tent containing RPCs 175 is placed at 1720 mm from the source container. The source is situated in the center 176 of the container. RE-4-2-BARC-161 chamber is 160 mm inside the tent. This way, 177 the distance between the source and the chambers plan is 2060 mm. Figure 5.7a 178 provides a side view of the setup in the xz plane while Figure 5.7b shows a top view 179 in the yz plane. . . . .	5-7
180	5.8	RE-4-2-BARC-161 chamber is inside the tent as described in Figure 5.7. In the top 181 right, the two scintillators used as trigger can be seen. This trigger system has an 182 inclination of 10° relative to horizontal and is placed above half-partition B2 of the 183 RPCs. PMT electronics are shielded thanks to lead blocks placed in order to protect 184 them without stopping photons from going through the scintillators and the chamber.	5-8
185	5.9	Hit distributions over all 3 partitions of RE-4-2-BARC-161 chamber is showed on 186 these plots. Top, middle and bottom figures respectively correspond to partitions A, 187 B, and C. These plots show that some events still occur in other half-partitions than 188 B2, which corresponds to strips 49 to 64, in front of which the trigger is placed, con- 189 tributing to the inefficiency of detection of cosmic muons. In the case of partitions 190 A and C, the very low amount of data can be interpreted as noise. On the other hand, 191 it is clear that a little portion of muons reach the half-partition B1, corresponding to 192 strips 33 to 48. . . . .	5-9
193	5.10	Results are derived from data taken on half-partition B2 only. On the 18 <sup>th</sup> of June 194 2014, data has been taken on chamber RE-2-BARC-161 at building 904 (Prevessin 195 Site) with cosmic muons providing us a reference efficiency plateau of $(97.54 \pm$ 196 $0.15)\%$ represented by a black curve. A similar measurement has been done at GIF 197 on the 21 <sup>st</sup> of July with the same chamber giving a plateau of $(78.52 \pm 0.94)\%$ 198 represented by a red curve. . . . .	5-10

---

199	5.11	Representation of the layout used for the simulations of the test setup. The RPC is represented as a yellow trapezoid while the two scintillators as blue cuboids looking at the sky. A green plane corresponds to the muon generation plane within the simulation. Figure 5.7a shows a global view of the simulated setup. Figure 5.7b shows a zommed view that allows to see the 2 scintillators as well as the full RPC plane. . . . .	5-11
200			
201			
202			
203			
204	5.12	$\gamma$ flux $F(D)$ is plot using values from table 5.1. As expected, the plot shows similar attenuation behaviours with increasing distance for each absorption factors. . . . .	5-14
205			
206	5.13	Figure 5.13a shows the linear approximation fit done via formulae 5.7 on data from table 5.2. Figure 5.13b shows a comparison of this model with the simulated flux using a and b given in figure 5.13a in formulae 5.4 and the reference value $D_0 = 50\text{cm}$ and the associated flux for each absorption factor $F_0^{ABS}$ from table 5.1 . . . . .	5-16
207			
208			
209			
210	5.14	Dose measurements has been done in a plane corresponding to the tents front side. This plan is 1900 mm away from the source. As explained in the first chapter, a lens-shaped lead filter provides a uniform photon flux in the vertical plan orthogonal to the beam direction. If the second line of measured fluxes is not taken into account because of lower values due to experimental equipments in the way between the source and the tent, the uniformity of the flux is well showed by the results. . . . .	5-18
211			
212			
213			
214			
215			
216	5.15	. . . . .	5-19
217	5.16	Evolution of the maximum efficiency for RE2 (5.16a) and RE4 (5.16b) chambers with increasing extrapolated $\gamma$ rate per unit area at working point. Both irradiated (blue) and non irradiated (red) chambers are shown. . . . .	5-21
218			
219			
220	5.17	Evolution of the working point for RE2 (5.17a) and RE4 (5.17b) with increasing extrapolated $\gamma$ rate per unit area at working point. Both irradiated (blue) and non irradiated (red) chambers are shown. . . . .	5-21
221			
222			
223	5.18	Evolution of the maximum efficiency at HL-LHC conditions, i.e. a background hit rate per unit area of 300 Hz/cm <sup>2</sup> , with increasing integrated charge for RE2 (5.18a) and RE4 (5.18b) detectors. Both irradiated (blue) and non irradiated (red) chambers are shown. The integrated charge for non irradiated detectors is recorded during test beam periods and stays small with respect to the charge accumulated in irradiated chambers. . . . .	5-22
224			
225			
226			
227			
228			
229	5.19	Comparison of the efficiency sigmoid before (triangles) and after (circles) irradiation for RE2 (5.19a) and RE4 (5.19b) detectors. Both irradiated (blue) and non irradiated (red) chambers are shown. . . . .	5-22
230			
231			
232	5.20	Evolution of the Bakelite resistivity for RE2 (5.20a) and RE4 (5.20b) detectors. Both irradiated (blue) and non irradiated (red) chambers are shown. . . . .	5-23
233			
234	5.21	Evolution of the noise rate per unit area for the irradiated chamber RE2-2-BARC-9 only. . . . .	5-23
235			
236	A.1	(A.1a) View of the front panel of a V1190A TDC module [29]. (A.1b) View of the front panel of a V1718 Bridge module [30]. (A.1c) View of the front panel of a 6U 6021 VME crate [31]. . . . .	A-3
237			
238			
239	A.2	Module V1190A <i>Trigger Matching Mode</i> timing diagram [29]. . . . .	A-4
240	A.3	Structure of the ROOT output file generated by the DAQ. The 5 branches ( <code>EventNumber</code> , <code>number_of_hits</code> , <code>Quality_flag</code> , <code>TDC_channel</code> and <code>TDC_TimeStamp</code> ) are visible on the left panel of the ROOT browser. On the right panel is visible the histogram corresponding to the variable <code>nHits</code> . In this specific example, there were approximately 50k events recorded to measure the gamma irradiation rate on the detectors. Each event is stored as a single entry in the <code>TTree</code> . . . . .	A-10
241			
242			
243			
244			
245			

- 
- 246     A.4 The effect of the quality flag is explained by presenting the content of `TBranch`  
 247       `number_of_hits` of a data file without `Quality_flag` in Figure A.4a and the con-  
 248       tent of the same `TBranch` for data corresponding to a `Quality_flag` where all TDCs  
 249       were labelled as `GOOD` in Figure A.4b taken with similar conditions. It can be noted  
 250       that the number of entries in Figure A.4b is slightly lower then in Figure A.4a due  
 251       to the excluded events. . . . . A-12
- 252     A.5 Using the same data as previously showed in Figure A.4, the effect of the quality  
 253       flag is explained by presenting the reconstructed hit multiplicity of a data file with-  
 254       out `Quality_flag` in Figure A.5a and the reconstructed content of the same RPC  
 255       partition for data corresponding to a `Quality_flag` where all TDCs were labelled as  
 256       `GOOD` in Figure A.5b taken with similar conditions. The artificial high content of bin  
 257       0 is completely suppressed. . . . . A-12
- 258     A.6 WebDCS DAQ scan page. On this page, shifters need to choose the type of scan  
 259       (Rate, Efficiency or Noise Reference scan), the gamma source configuration at the  
 260       moment of data taking, the beam configuration, and the trigger mode. These in-  
 261       formation will be stored in the DAQ ROOT output. Are also given the minimal  
 262       measurement time and waiting time after ramping up of the detectors is over before  
 263       starting the data acquisition. Then, the list of HV points to scan and the number of  
 264       triggers for each run of the scan are given in the table underneath. . . . . A-14
- 265     B.1 Example of expected hit time distributions in the cases of efficiency (Figure B.1a)  
 266       and noise/gamma rate per unit area (Figure B.1b) measurements as extracted from  
 267       the raw ROOT files. The unit along the x-axis corresponds to ns. The fact that  
 268       "the" muon peak is not well defined in Figure B.1a is due to the contribution of all  
 269       the RPCs being tested at the same time that don't necessarily have the same signal  
 270       arrival time. Each individual peak can have an offset with the ones of other detectors.  
 271       The inconsitancy in the first 100 ns of both time distributions is an artefact of the  
 272       TDCs and are systematically rejected during the analysis. . . . . B-16
- 273     B.2 The effect of the quality flag is explained by presenting the reconstructed hit multi-  
 274       plicity of a data file without `Quality_flag`. The artificial high content of bin 0 is the  
 275       effect of corrupted data. . . . . B-19
- 276     B.3 Display of the masking tool page on the webDCS. The window on the left allows the  
 277       shifter to edit `ChannelsMapping.csv`. To mask a channel, it only is needed to set the  
 278       3rd field corresponding to the strip to mask to 0. It is not necessary for older mapping  
 279       file formats to add a 1 for each strip that is not masked as the code is versatile and  
 280       the default behaviour is to consider missing mask fields as active strips. The effect  
 281       of the mask is directly visible for noisy channels as the corresponding bin turns red.  
 282       The global effect of masking strips will be an update of the rate value showed on the  
 283       histogram that will take into consideration the rejected channels. . . . . B-24

## List of Tables

284

285	4.1	Properties of the most used electrode materials for RPCs. . . . .	4-3
286	5.1	Total photon flux ( $E\gamma \leq 662$ keV) with statistical error predicted considering a $^{137}\text{Cs}$ activity of 740 GBq at different values of the distance $D$ to the source along the x-axis of irradiation field [25]. . . . .	5-13
287	5.2	Correction factor $c$ is computed thanks to formulae 5.5 taking as reference $D_0 =$ 50 cm and the associated flux $F_0^{ABS}$ for each absorption factor available in table 5.1.	5-15
288	5.3	The data at $D_0$ in 1997 is taken from [25]. In a second step, using Equations 5.8 and 5.9, the flux at $D$ can be estimated in 1997. Then, taking into account the attenuation of the source activity, the flux at $D$ can be estimated at the time of the tests in GIF in 2014. Finally, assuming a sensitivity of the RPC to $\gamma$ $s = 2 \cdot 10^{-3}$ , an estimation of the hit rate per unit area is obtained. . . . .	5-17
295	A.1	Inter-process communication cycles in between the webDCS and the DAQ through file string signals. . . . .	A-19



# List of Acronyms

## List of Acronyms

### A

304 **AFL**

Almost Full Level

### B

309 **BARC**

Bhabha Atomic Research Centre

310 **BLT**

Block Transfer

311 **BR**

Branching Ratio

### C

316 **CAEN**

Costruzioni Apparecchiature Elettroniche Nucleari S.p.A.

317 **CERN**

European Organization for Nuclear Research

318 **CFD**

Constant Fraction Discriminator

319 **CMS**

Compact Muon Solenoid

320 **CSC**

Cathode Strip Chamber

### D

325 **DAQ**

Data Acquisition

326 **DCS**

Detector Control Software

327 **DQM**

Data Quality Monitoring

328 **DT**

Drift Tube

### F

333	<b>FEE</b>	Front-End Electronics
334	<b>FEB</b>	Front-End Board
335		
336	<b>G</b>	
338		
339	<b>GE-/-</b>	Find a good description
340	<b>GE1/1</b>	Find a good description
341	<b>GE2/1</b>	Find a good description
342	<b>GEANT</b>	GEometry ANd Tracking - a series of software toolkit platforms developed by CERN
343		
344	<b>GEM</b>	Gas Electron Multiplier
345	<b>GIF</b>	Gamma Irradiation Facility
346	<b>GIF++</b>	new Gamma Irradiation Facility
347		
348	<b>H</b>	
349		
350		
351	<b>HL-LHC</b>	High Luminosity LHC
352	<b>HPL</b>	High-pressure laminate
353	<b>HV</b>	High Voltage
354		
355		
356	<b>I</b>	
357		
358	<b>iRPC</b>	improved RPC
359	<b>IRQ</b>	Interrupt Request
360		
361		
362	<b>L</b>	
363		
364	<b>LHC</b>	Large Hadron Collider
365	<b>LS1</b>	First Long Shutdown
366	<b>LS3</b>	Third Long Shutdown
367	<b>LV</b>	Low Voltage
368	<b>LVDS</b>	Low-Voltage Differential Signaling
369		
370		
371	<b>M</b>	
372		
373	<b>MC</b>	Monte Carlo
374	<b>MCNP</b>	Monte Carlo N-Particle
375	<b>ME-/-</b>	Find good description

---

376	ME0	Find good description
377		
378		
379	<b>N</b>	
380		
381	NIM	Nuclear Instrumentation Module logic signals
382		
383		
384	<b>P</b>	
385		
386	PMT	PhotoMultiplier Tube
387		
388		
389	<b>R</b>	
390		
391	RE-/-	Find a good description
392	RE2/2	Find a good description
393	RE3/1	Find a good description
394	RE3/2	Find a good description
395	RE4/1	Find a good description
396	RE4/2	Find a good description
397	RE4/3	Find a good description
398	RMS	Root Mean Square
399	ROOT	a framework for data processing born at CERN
400	RPC	Resistive Plate Chamber
401		
402		
403	<b>S</b>	
404		
405	SPS	Super Proton Synchrotron
406		
407		
408	<b>T</b>	
409		
410	TDC	Time-to-Digital Converter
411		
412		
413	<b>W</b>	
414		
415	webDCS	Web Detector Control System



417

## Nederlandse samenvatting –Summary in Dutch–

418

419 Le resume en Neerlandais (j'aurais peut-être de apprendre la langue juste pour ca...).



## English summary

<sup>421</sup> Le meme résume mais en Anglais (on commencera par la hein!).



# 1

## Introduction

422

423

<sup>424</sup> **1.1 A story of High Energy Physics**

<sup>425</sup> **1.2 Organisation of this study**



# 2

426

427

## Investigating the TeV scale

428

### 2.1 The Standard Model of Particle Physics

429

### 2.2 The Large Hadron Collider and the Compact Muon Solenoid

430

### 2.3 Muon Phase-II Upgrade

431

After the more than two years lasting First Long Shutdown (LS1), the Large Hadron Collider (LHC) delivered its very first Run-II proton-proton collisions early 2015. LS1 gave the opportunity to the LHC and to its experiments to undergo upgrades. The accelerator is now providing collisions at center-of-mass energy of 13 TeV and bunch crossing rate of 40 MHz, with a peak luminosity exceeding its design value. During the first and upcoming second LHC Long Shutdown, the Compact Muon Solenoid (CMS) detector is also undergoing a number of upgrades to maintain a high system performance [1].

438

From the LHC Phase-2 or High Luminosity LHC (HL-LHC) period onwards, i.e. past the Third Long Shutdown (LS3), the performance degradation due to integrated radiation as well as the average number of inelastic collisions per bunch crossing, or pileup, will rise substantially and become a major challenge for the LHC experiments, like CMS that are forced to address an upgrade program for Phase-II [2]. Simulations of the expected distribution of absorbed dose in the CMS detector under HL-LHC conditions, show in figure 5.14 that detectors placed close to the beamline will have to withstand high irradiation, the radiation dose being of the order of a few tens of Gy.

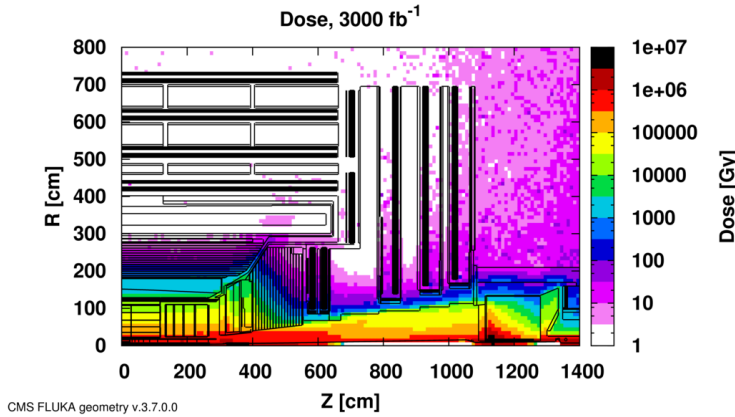


*Figure 2.1: Absorbed dose in the CMS cavern after an integrated luminosity of 3000 fb<sup>-1</sup>. R is the transverse distance from the beamline and Z is the distance along the beamline from the Interaction Point at Z=0.*

445     The measurement of small production cross-section and/or decay branching ratio processes, such  
 446     as the Higgs boson coupling to charge leptons or the  $B_s \rightarrow \mu^+\mu^-$  decay, is of major interest and  
 447     specific upgrades in the forward regions of the detector will be required to maximize the physics  
 448     acceptance on the largest possible solid angle. To ensure proper trigger performance within the  
 449     present coverage, the muon system will be completed with new chambers. In figure 2.2 one can  
 450     see that the existing Cathode Strip Chambers (CSCs) will be completed by Gas Electron Multipliers  
 451     (GEMs) and Resistive Plate Chambers (RPCs) in the pseudo-rapidity region  $1.6 < |\eta| < 2.4$  to  
 452     complete its redundancy as originally scheduled in the CMS Technical Proposal [3].

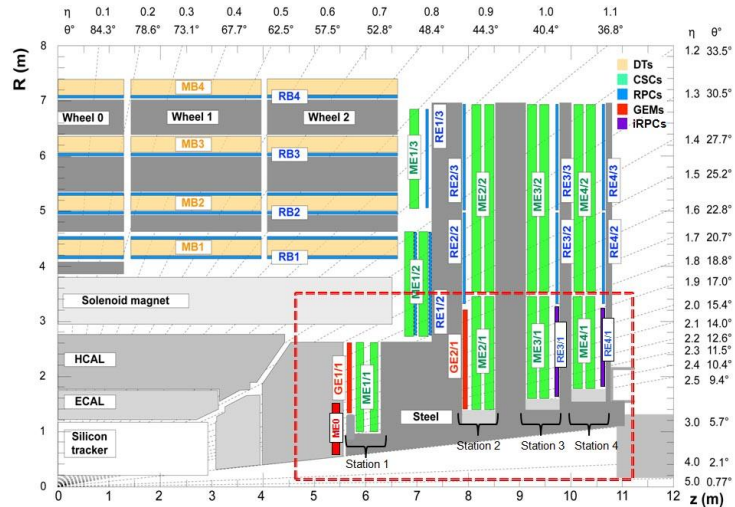


*Figure 2.2: A quadrant of the muon system, showing DTs (yellow), RPCs (light blue), and CSCs (green). The locations of new forward muon detectors for Phase-II are contained within the dashed box and indicated in red for GEM stations (ME0, GE1/1, and GE2/1) and dark blue for improved RPC (iRPC) stations (RE3/1 and RE4/1).*

453     RPCs are used by the CMS first level trigger for their good timing performances. Indeed, a very

good bunch crossing identification can be obtained with the present CMS RPC system, given their fast response of the order of 1 ns. In order to contribute to the precision of muon momentum measurements, muon chambers should have a spatial resolution less or comparable to the contribution of multiple scattering [1]. Most of the plausible physics is covered only considering muons with  $p_T < 100$  GeV thus, in order to match CMS requirements, a spatial resolution of  $\mathcal{O}(\text{few mm})$  the proposed new RPC stations, as shown by the simulation in figure 2.3. According to preliminary designs, RE3/1 and RE4/1 readout pitch will be comprised between 3 and 6 mm and 5  $\eta$ -partitions could be considered.

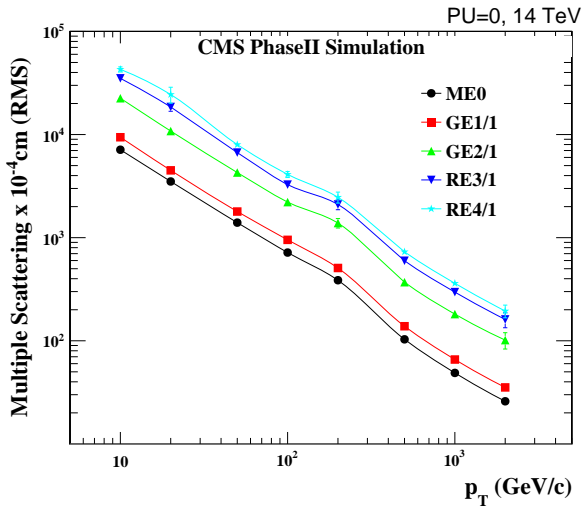


Figure 2.3: RMS of the multiple scattering displacement as a function of muon  $p_T$  for the proposed forward muon stations. All of the electromagnetic processes such as bremsstrahlung and magnetic field effect are included in the simulation.



# 3

462

463

## Amplification processes in gaseous detectors

464

### **3.1 Signal formation**

465

### **3.2 Gas transport parameters**



# 4

466

467

## Resistive Plate Chambers

468 A Resistive Plate Chamber (RPC) is a gaseous detector using the same physical processes described  
469 in Chapter 3. It has been developed in 1981 by Santonico and Cardarelli [4], under the name of  
470 *Resistive Plate Counter*, as an alternative to the local-discharge spark counters proposed in 1978  
471 by Pestov and Fedotovich [5, 6]. Working with spark chambers implied using high-pressure gas  
472 and high mechanical precision which the RPC simplified by formerly using a gas mixture of argon  
473 and butane flowed at atmospheric pressure and a constant and uniform electric field propagated  
474 in between two parallel electrode plates. Moreover, a significant increase in rate capability was  
475 introduced by the use of electrode plate material with high bulk resistivity, preventing the discharge  
476 from growing throughout the whole gas gap. Indeed, the effect of using resistive electrodes is that  
477 the constant electric field is locally canceled out by the development of the discharge, limiting its  
478 growth.

479 Through its development history, different operating modes [7–9] and new detector designs [10–  
480 12] have been discovered, leading to further improvement of the rate capability of such a detector.  
481 Moreover, the addition of  $SF_6$  into the gas mix improved the stability of operation of the RPC [13,  
482 14].

483 The low developing costs and easily achievable large detection areas offered by RPCs, as well  
484 as the wide range of possible designs, made them a natural choice to as muon chambers and/or  
485 trigger detectors in multipurpose experiments such as CMS [1] or ATLAS [15], time-of-flight detec-  
486 tors in ALICE [16], calorimeter with CALICE [17] or even detectors for volcanic muography with  
487 ToMuVol [18].

### 488 4.1 Principle

489 RPCs are ionisation detectors composed of two parallel resistive plate electrodes in between which  
490 a constant electric field is set. The space in between the electrodes, referred as *gap*, is filled with a  
491 dense gas that is used to generate primary ionization into the gas volume. The free charge carriers  
492 (electrons and cations) created by the ionization of the gas molecules are then accelerated towards

493 the electrodes by the electric field, as shown in Figure 4.1 [19].

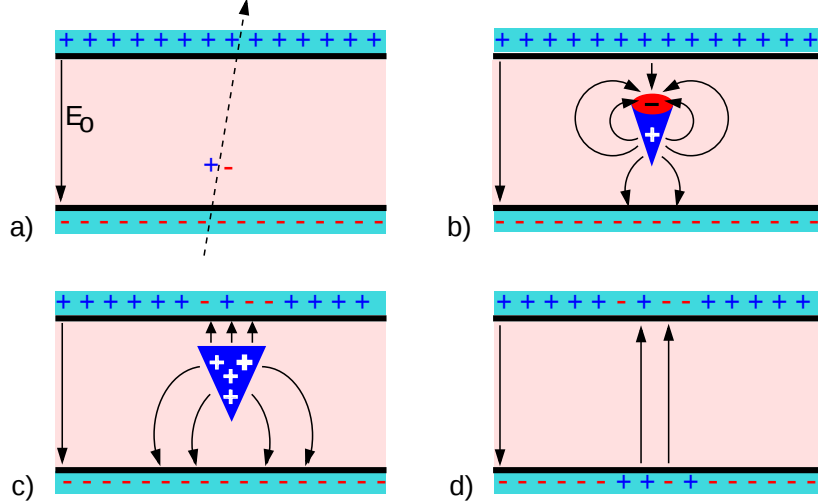


Figure 4.1: Different phases of the avalanche development in the RPC gas volume subjected to a constant electric field  $E_0$ . a) An avalanche is initiated by the primary ionisation caused by the passage of a charged particle through the gas volume. b) Due to its growing size, the avalanche starts to locally influence the electric field. c) The electrons, lighter than the cations reach the anode first. d) The ions reach the cathode. While the charges have not recombined, the electric field in the small region around the avalanche stays affected and locally blind the detector.

494 RPCs being passive detectors, a current on pick-up copper read-out placed outside of the gas  
 495 volume is induced by the charge accumulation during the growth of the avalanche. As a result,  
 496 the time resolution of the detector is substantially increased as the output signal is generated while  
 497 the electrons are still in movement. The advantage of a constant electric field, over multi-wire  
 498 proportional chambers, is that the electrons are being fully accelerated from the moment charge  
 499 carriers are freed and feel the full strength of the electric field that doesn't depend on the distance to  
 500 the readout and that the output signal doesn't need for the electrons to be physically collected.

501 The typical gas mixture RPCs are operated with is generally composed of 3 gas compounds.

- 502 • Tetrafluoroethane ( $C_2F_4H_2$ ), also referred to as *Freon*, is the principal compound of the RPC  
 503 gas mixtures, with a typical fraction above 90%. It is used for it's high effective Townsend  
 504 coefficient and the great average fast charge that allows to operate the detector with a high  
 505 threshold with respect to argon, for example, that has similar effective Townsend coefficient  
 506 but suffers from a lower fast charge. To operate with similar conditions, argon would require a  
 507 higher electric field leading to a higher fraction of streamers, thus limiting the rate capability  
 508 of the detector [21].
- 509 • Isobutane (i- $C_4H_{10}$ ), only present in a few percent in the gas mixtures, is used for its UV  
 510 quenching properties [22] helping to prevent streamers due to UV photon emission during the  
 511 avalanche growth.
- 512 • Sulfur hexafluoride, ( $SF_6$ ), referred to simply as *SF6*, is used in very little quantities for its  
 513 high electronegativity. Excess of electrons are being absorbed by the compound and streamers

514        are suppressed [14]. Nevertheless, a fraction of  $SF_6$  higher than 1% will not bring any extra  
 515        benefice in terms of streamer cancelation power but will lead to higher operating voltage.

516        After an avalanche developed in the gas, a time long compared to the development of a discharge  
 517        is needed to recombine the charge carriers in the electrode material due to their resistivity. This  
 518        property has the advantage of affecting the local electric field and avoiding sparks in the detector  
 519        but, on the other hand, the rate capability is intrinsically limited by the time constant  $\tau_{RPC}$  of the  
 520        detector. Using a quasi-static approximation of Maxwell's equations for weakly conducting media,  
 521        it can be shown that the time constant  $\tau_{RPC}$  necessary to the charge recombination at the interface  
 522        in between the electrode and the gas volume is given by the Formula 4.1 [20].

$$\tau_{RPC} = \frac{\epsilon_{electrode} + \epsilon_{gas}}{\sigma_{electrode} + \sigma_{gas}} \quad (4.1)$$

523        A gas can be assimilated to vacuum, leading to  $\epsilon_{gas} = \epsilon_0$  and  $\sigma_{gas} = 0$ , and the electrodes  
 524        permittivity and conductivity can be written as  $\epsilon_{electrode} = \epsilon_r \epsilon_0$  and  $\sigma_{electrode} = 1/\rho_{electrode}$ ,  
 525        showing the strong dependence of the time constant to the electrodes resistivity in Formula 4.2.

$$\tau_{RPC} = (\epsilon_r + 1)\epsilon_0 \times \rho_{electrode} \quad (4.2)$$

526        Very few materials with a low enough resistivity exist in nature. The resistivity targeted to build  
 527        RPCs ranges from  $10^9$  to  $10^{12} \Omega \cdot \text{cm}$ . The most common RPC electrode materials are displayed in  
 528        Table 4.1. When the doped glass and ceramics can offer short time constants of the order of 1 ms,  
 529        the developing cost of such materials is quite high due to the very low demand. Thus, High-pressure  
 530        laminate (HPL) is often the choice for high rate experiments using very large RPC detection areas.  
 531        Other experiments working at cosmic muon fluxes can safely operate with ordinary float glass.

Material	$\rho_{electrode} (\Omega \cdot \text{cm})$	$\epsilon_r$	$\tau_{RPC} (\text{ms})$
Float glass	$10^{12}$	~7	~700
High-pressure laminate	$10^{10}$ to $10^{12}$	~6	~6 to 600
Doped glass (LR S)	$10^9$ to $10^{11}$	~10	~1 to 100
Doped ceramics (SiN/SiC)	$10^9$	~8.5	~1
Doped ceramics (Ferrite)	$10^8$ to $10^{12}$	~20	~0.2 to 2000

Table 4.1: Properties of the most used electrode materials for RPCs.

532        [Talk about the active volume inside of the gas gap : due to the exponential growth of the  
 533        avalanche, only the first few percent of the gas volume will be able to give enough gain to see a  
 534        strong enough signal.]

## 535        4.2 Rate capability of Resistive Plate Chambers

536        As already previously discussed, the electrode material plays a key role in the max intrinsic rate  
 537        capability of RPCs. R&D is being done to develop at always cheaper costs material with lower  
 538        resistivity. Nevertheless, the amount of charge released, i.e. the size of the discharge, if reduced  
 539        leads to a smaller blind area in the detector, increasing the rate capability of the detector.

<sup>540</sup> **4.2.1 Operation modes**

<sup>541</sup> RPCs were developed early 1980s. At that time it was using an operating mode now referred to  
<sup>542</sup> as *streamer mode*. Streamers are large discharges that develop in between the 2 electrodes enough  
<sup>543</sup> to connect them and discharge them locally. Indeed, electrodes, though they are a unique volume  
<sup>544</sup> of resistive material, can be assimilated to capacitors. At the moment an electric field is applied  
<sup>545</sup> in between their outer surfaces, the charge carriers inside of the volume will start moving leading  
<sup>546</sup> eventually to a situation where there is no voltage across the electrodes. Finally, when a streamer  
<sup>547</sup> discharge occurs, the negative charge of the electrons on the anode and the positive charges of the  
<sup>548</sup> cations on the cathode will locally affect and reduce the electric field, quenching the streamer and  
<sup>549</sup> preventing a spark to connect the two electrodes and fully discharge them by release the full charge  
<sup>550</sup> contained in both of them. This can be understood through Figure 4.2 [7].

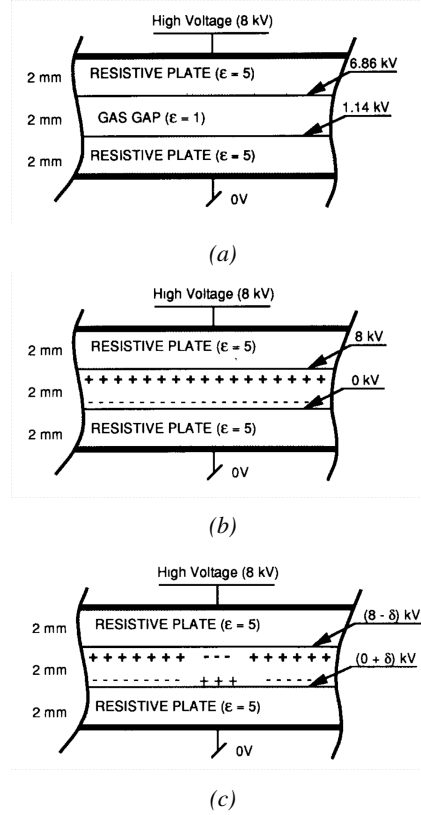


*Figure 4.2: Movement of the charge carriers in an RPC. Figure 4.2a: Voltage across an RPC whose electrode have a relative permittivity of 5 at the moment the tension s applied. Figure 4.2b: After the charge carriers moved, the electrodes are charged and there is no voltage drop over the electrodes anymore. The full potential is applied on the gas gap only. Figure 4.2c: The streamer discharge initiated by a charged particle transports electrons and cations towards the anode and cathode respectively.*

## 551    **4.3 High time resolution**

### 552    **4.3.1 Electron drift velocity**

## 553    **4.4 Resistive Plate Chambers at CMS**

### 554    **4.4.1 Overview**

555    The Resistive Plate Chambers (RPC) system, located in both barrel and endcap regions, provides a  
556    fast, independent muon trigger with a looser  $p_T$  threshold over a large portion of the pseudorapidity  
557    range ( $|\eta| < 1.6$ ) [add reconstruction].

558    During High-Luminosity LHC (HL-LHC) operations the expected conditions in terms of back-  
559    ground and pile-up will make the identification and correct  $P_T$  assignment a challenge for the Muon  
560    system. The goal of RPC upgrade is to provide additional hits to the Muon system with precise tim-  
561    ing. All these informations will be elaborated by the trigger system in a global way enhancing the  
562    performance of the trigger in terms of efficiency and rate control. The RPC Upgrade is based on two  
563    projects: an improved Link Board System and the extension of the RPC coverage up to  $|\eta| = 2.4$ .  
564    [FIXME 2.4 or 2.5?]

565    The Link Board system, that will be described in section xxx, is responsible to process, syn-  
566    chronize and zero-suppress the signals coming from the RPC front end boards. The Link Board  
567    components have been produced between 2006 and 2007 and will be subjected to aging and failure  
568    in the long term. The upgraded Link Board system will overcome the aging problems described in  
569    section xxx and will allow for a more precise timing information to the RPC hits from 25 to 1 ns [ref  
570    section xxx].

571    The extension of the RPC system up to  $|\eta| = 2.1$  was already planned in the CMS TDR [ref  
572    cmstdr] and staged because of budget limitations and expected background rates higher than the rate  
573    capability of the present CMS RPCs in that region. An extensive R&D program has been done in  
574    order to develop an improved RPC that fulfills the CMS requirements. Two new RPC layers in the  
575    innermost ring of stations 3 and 4 will be added with benefits to the neutron-induced background  
576    reduction and efficiency improvement for both trigger and offline reconstruction.

### 578    **4.4.2 The present RPC system**

579    The RPC system is organized in 4 stations called RB1 to RB4 in the barrel region, and RE1 to RE4  
580    in the endcap region. The innermost barrel stations, RB1 and RB2, are instrumented with 2 layers  
581    of RPCs facing the innermost (RB1in and RB2in) and outermost (RB1out and RB2out) sides of the  
582    DT chambers. Every chamber is then divided from the read-out point of view into 2 or 3  $\eta$  partitions  
583    called “rolls”. The RPC system consist of 480 barrel chambers and 576 endcap chambers. Details  
584    on the geometry are discussed in the paper [ref to geo paper].

585    The CMS RPC chamber is a double-gap, operated in avalanche mode to ensure reliable operation  
586    at high rates. Each RPC gap consists of two 2-mm-thick resistive High-Pressure Laminate (HPL)  
587    plates separated by a 2-mm-thick gas gap. The outer surface of the HPL plates is coated with a thin  
588    conductive graphite layer, and a voltage is applied. The RPCs are operated with a 3-component,  
589    non-flammable gas mixture consisting of 95.2% freon ( $C_2H_2F_4$ , known as R134a), 4.5% isobutane  
590    ( $i-C_4H_{10}$ ), and 0.3% sulphur hexafluoride ( $SF_6$ ) with a relative humidity of 40% - 50%. Readout  
591    strips are aligned in  $\eta$  between the 2 gas gaps. [Add a sentence on FEBs.]

592 The discriminated signals coming from the Front End boards feed via twisted cables (10 to 20 m  
 593 long) the Link Board System located in UXC on the balconies around the detector. The Link System  
 594 consist of the 1376 Link Boards (LBs) and the 216 Control Boards (CBs), placed in 108 Link Boxes.  
 595 The Link Box is a custom crate (6U high) with 20 slots (for two CBs and eighteen LBs). The Link  
 596 Box contains custom backplane to which the cables from the chambers are connected, as well as the  
 597 cables providing the LBs and CBs power supply and the cables for the RPC FEBs control with use  
 598 of the I2C protocol (trough the CB). The backplane itself contains only connectors (and no any other  
 599 electronic devices).

600 The Link Board has 96 input channels (one channel corresponds to one RPC strip). The input  
 601 signals are the  $\sim$ 100 ns binary pulses which are synchronous to the RPC hits, but not to the LHC  
 602 clock (which drives the entire CMS electronics). Thus the first step of the FEB signals processing  
 603 is synchronization, i.e. assignment of the signals to the BXes (25 ns periods). Then the data are  
 604 compressed with a simple zero-suppressing algorithm (the input channels are grouped into 8 bit  
 605 partitions, only the partitions with at least one nonzero bit are selected for each BX). Next, the non-  
 606 empty partitions are time-multiplexed i.e. if there are more than one such partition in a given BX,  
 607 they are sent one-by-one in consecutive BXes. The data from 3 neighbouring LBs are concentrated  
 608 by the middle LB which contains the optical transmitter for sending them to the USC over a fiber at  
 609 1.6 Gbps.

610 The Control Boards provide the communication of the control software with the LBs via the  
 611 FEC/CCU system. The CBs are connected into token rings, each ring consists of 12 CBs of one  
 612 detector tower and a FEC mezzanine board placed on the CCS board located in the VME crate in  
 613 the USC. In total, there are 18 rings in the entire Link System. The CBs also perform automatic  
 614 reloading of the LB's firmware which is needed in order to avoid accumulation of the radiation  
 615 induced SEUs in the LBs firmware.

616 Both LBs and CB are based on the Xilinx Spartan III FPGAs, the CB additionally contains  
 617 radiation-tolerant (FLASH based) FPGA Actel ProAsicPlus.

618 The High Voltage power system is located in USC, not exposed to radiation and easily accessible  
 619 for any reparation. A single HV channel powers 2 RPC chambers both in the barrel and endcap  
 620 regions. The Low Voltage boards are located in UXC on the balconies and provide the voltage to the  
 621 front end electronics.

#### 622 **4.4.3 Pulse processing of CMS RPCs**

623 Signals induced by cosmic particle in the RPC strips are shaped by standard CMS RPC Front-End  
 624 Electronics (FEE) following the scheme of Figure 4.3. On a first stage, analogic signals are amplified  
 625 and then sent to the Constant Fraction Discriminator (CFD) described in Figure 4.4. At the end of  
 626 the chain, 100 ns long pulses are sent in the LVDS output. These output signal are sent on one side to  
 627 a V1190A Time-to-Digital Converter (TDC) module from CAEN and on the other to an OR module  
 628 to count the number of detected signals. Trigger and hit coïncidences are monitored using scalers.  
 629 The TDC is used to store the data into ROOT files. These files are thus analysed to understand the  
 630 detectors performance.

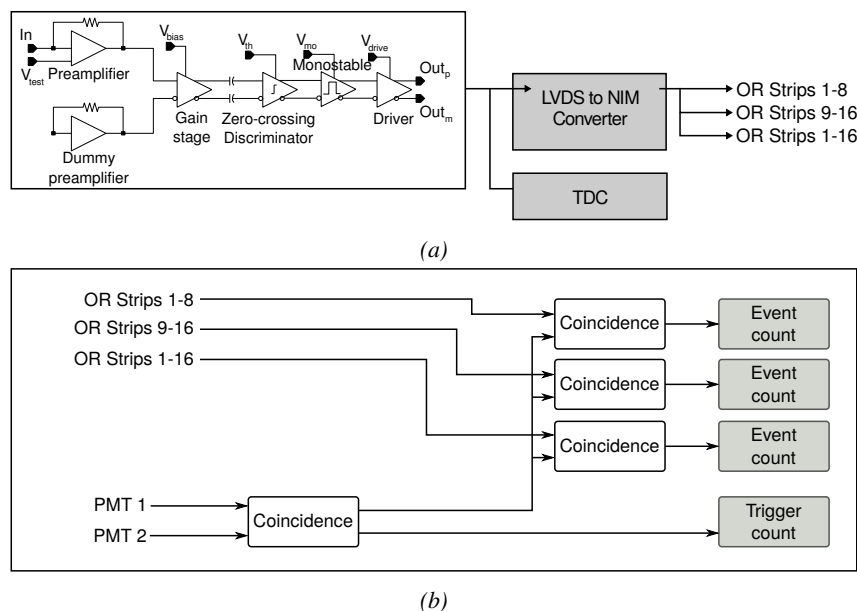
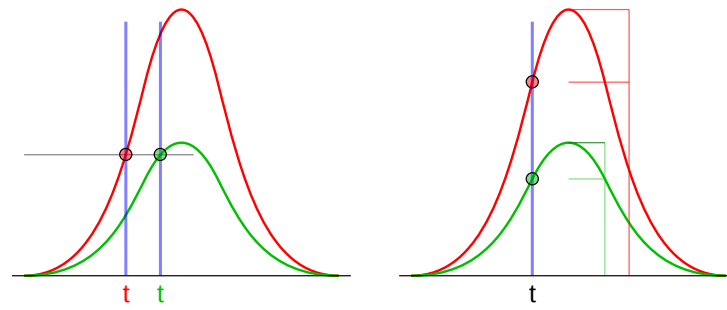
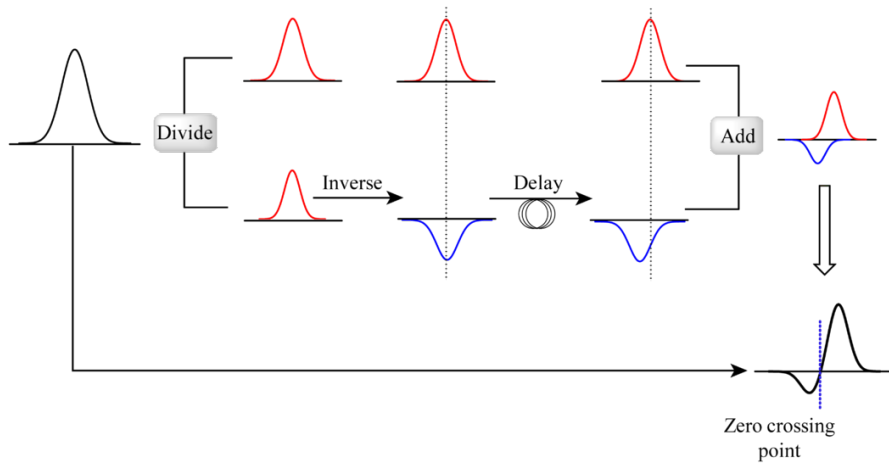


Figure 4.3: Signals from the RPC strips are shaped by the FEE described on Figure 4.3a. Output LVDS signals are then read-out by a TDC module connected to a computer or converted into NIM and sent to scalers. Figure 4.3b describes how these converted signals are put in coincidence with the trigger.



(a)



(b)

*Figure 4.4: Description of the principle of a CFD. A comparison of threshold triggering (left) and constant fraction triggering (right) is shown in Figure 4.4a. Constant fraction triggering is obtained thanks to zero-crossing technique as explained in Figure 4.4b. The signal arriving at the input of the CFD is split into three components. A first one is delayed and connected to the inverting input of a first comparator. A second component is connected to the noninverting input of this first comparator. A third component is connected to the noninverting input of another comparator along with a threshold value connected to the inverting input. Finally, the output of both comparators is fed through an AND gate.*

# 5

631

632

633

## Longevity studies and Consolidation of the present CMS RPC subsystem

634

### 5.1 Testing detectors under extreme conditions

635

The upgrade from LHC to HL-LHC will increase the peak luminosity from  $10^{34} \text{ cm}^{-2} \text{ s}^{-1}$  to reach  $5 \times 10^{34} \text{ cm}^{-2} \text{ s}^{-1}$ , increasing in the same way the total expected background to which the RPC system will be subjected to. Composed of low energy gammas and neutrons from  $p\text{-}p$  collisions, low momentum primary and secondary muons, puch-through hadrons from calorimeters, and particles produced in the interaction of the beams with collimators, the background will mostly affect the regions of CMS that are the closest to the beam line, i.e. the RPC detectors located in the endcaps.

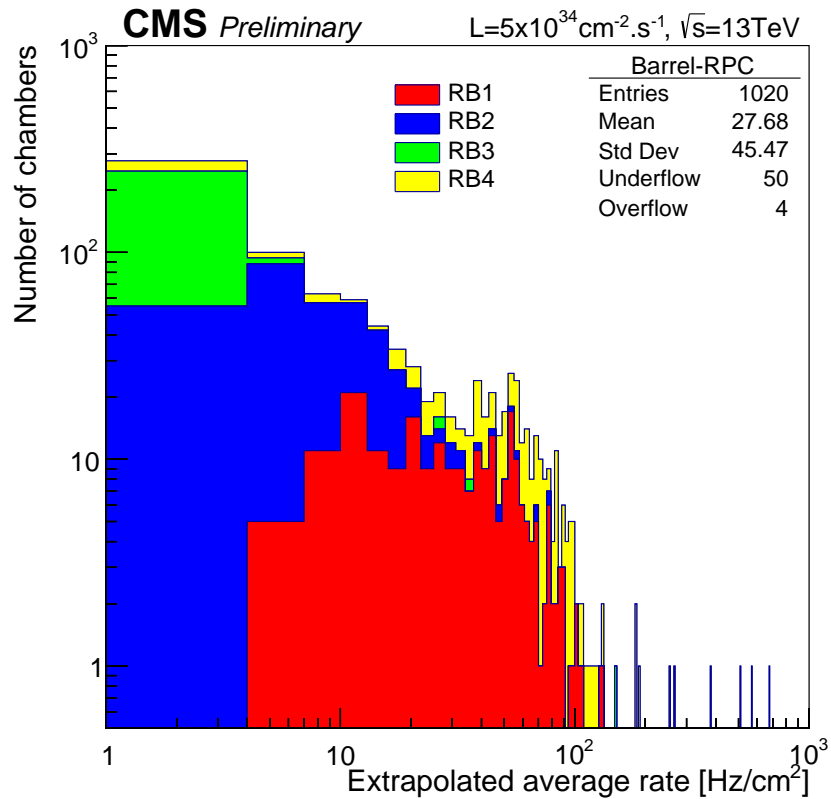
[To update.]

642

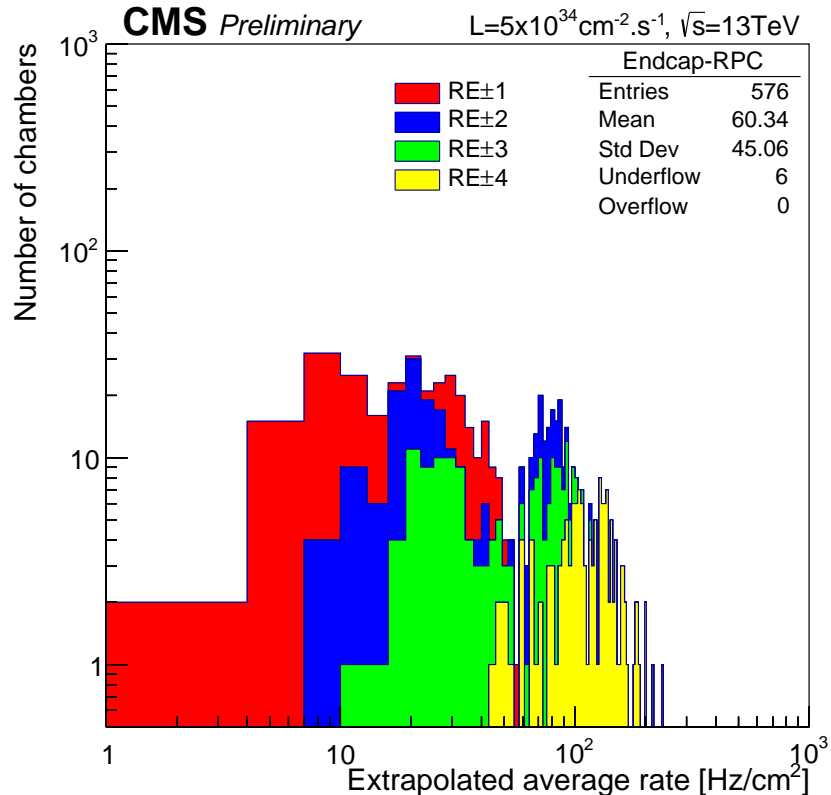
643

The 2016 data allowed to study the values of the background rate in all RPC system. In Figure 5.1, the distribution of the chamber background hit rate per unit area is shown at a luminosity of  $5 \times 10^{34} \text{ cm}^{-2} \cdot \text{s}^{-1}$  linearly extrapolating from data collected in 2016 [ref mentioning the linear dependency of rate vs lumi]. The maximum rate per unit area at HL-LHC conditions is expected to be of the order of  $600 \text{ Hz/cm}^2$  (including a safety factor 3). Nevertheless, Fluka simulations have conducted in order to understand the background at HL-LHC conditions. The comparison to the data has shown, in Figure 5.2, a discrepancy of a factor 2 even though the order of magnitude is consistent. [Understand mismatch.]

651



(a)



(b)

Figure 5.1: (5.1a) Extrapolation from 2016 data of single hit rate per unit area in the barrel region. (5.1b) Extrapolation from 2016 data of single hit rate per unit area in the endcap region.

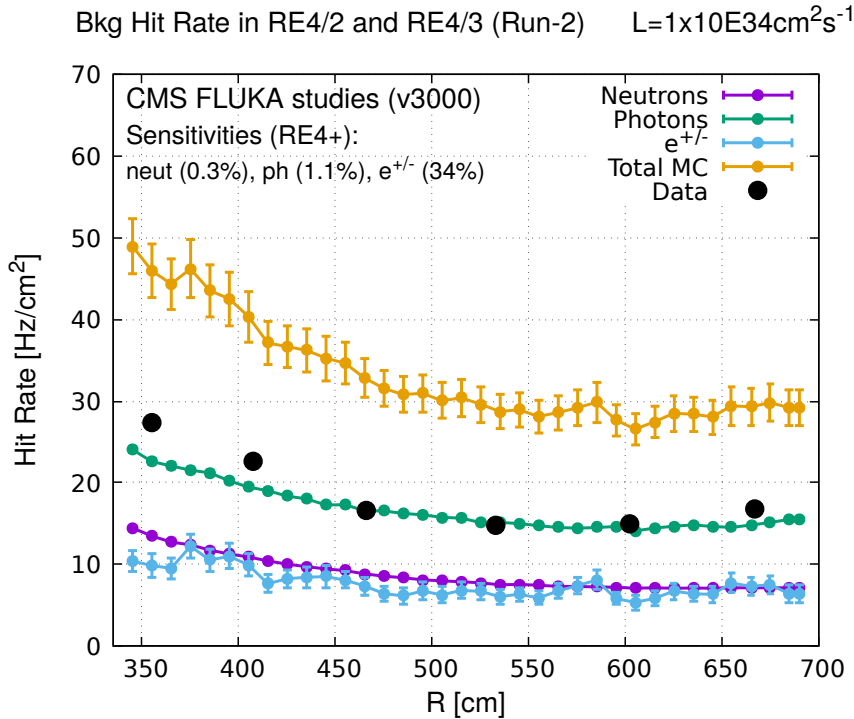


Figure 5.2: Background Fluka simulation compared to 2016 Data at  $L = 10^{34}\text{cm}^{-2}\cdot\text{s}^{-1}$  in the fourth endcap disk region. A mismatch in between simulation and data can be observed. [\[To be understood.\]](#)

In the past, extensive long-term tests were carried out at several gamma and neutron facilities certifying the detector performance. Both full size and small prototype RPCs have been irradiated with photons up to an integrated charge of  $\sim 0.05C/\text{cm}^2$  and  $\sim 0.4C/\text{cm}^2$ , respectively [23, 24]. During Run-I, the RPC system provided stable operation and excellent performance and did not show any aging effects for integrated charge of the order of  $0.01C/\text{cm}^2$ . Projections on currents from 2016 Data, has allowed to determine that the total integrated charge, by the end of HL-LHC, would be of the order of  $1C/\text{cm}^2$  (including a safety factor 3). [\[Corresponding figure needed.\]](#)

659

### 660 5.1.1 The Gamma Irradiation Facilities

#### 661 5.1.1.1 GIF

662 Located in the SPS West Area at the downstream end of the X5 test beam, the Gamma Irradiation  
663 Facility (GIF) was a test area in which particle detectors were exposed to a particle beam in presence  
664 of an adjustable gamma background [25]. Its goal was to reproduce background conditions these  
665 detectors would suffer in their operating environment at LHC. GIF layout is shown in Figure 5.3.  
666 Gamma photons are produced by a strong  $^{137}\text{Cs}$  source installed in the upstream part of the zone  
667 inside a lead container. The source container includes a collimator, designed to irradiate a  $6 \times 6\text{ m}^2$   
668 area at 5 m maximum to the source. A thin lens-shaped lead filter helps providing with a uniform  
669 outcoming flux in a vertical plane, orthogonal to the beam direction. The principal collimator hole  
670 provides a pyramidal aperture of  $74^\circ \times 74^\circ$  solid angle and provides a photon flux in a pyramidal vol-

ume along the beam axis. The photon rate is controled by further lead filters allowing the maximum rate to be limited and to vary within a range of four orders of magnitude. Particle detectors under test are then placed within the pyramidal volume in front of the source, perpendicularly to the beam line in order to profit from the homogeneous photon flux. Adjusting the background flux of photons can then be done by using the filters and choosing the position of the detectors with respect to the source.

676

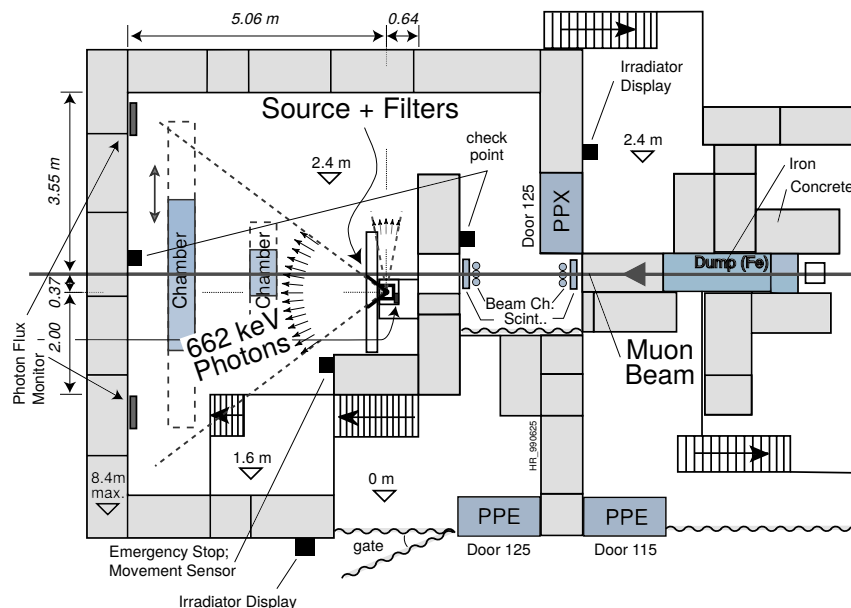


*Figure 5.3: Layout of the test beam zone called X5c GIF at CERN. Photons from the radioactive source produce a sustained high rate of random hits over the whole area. The zone is surrounded by 8 m high and 80 cm thick concrete walls. Access is possible through three entry points. Two access doors for personnel and one large gate for material. A crane allows installation of heavy equipment in the area.*

677 As described on Figure 5.4, the  $^{137}\text{Cs}$  source emits a 662 keV photon in 85% of the decays. An  
 678 activity of 740 GBq was measured on the 5<sup>th</sup> March 1997. To estimate the strength of the flux in  
 679 2014, it is necessary to consider the nuclear decay through time assiciated to the Cesium source  
 680 whose half-life is well known ( $t_{1/2} = (30.05 \pm 0.08)$  y). The GIF tests where done in between the  
 681 20<sup>th</sup> and the 31<sup>st</sup> of August 2014, i.e. at a time  $t = (17.47 \pm 0.02)$  y resulting in an attenuation of  
 682 the activity from 740 GBq in 1997 to 494 GBq in 2014.

683

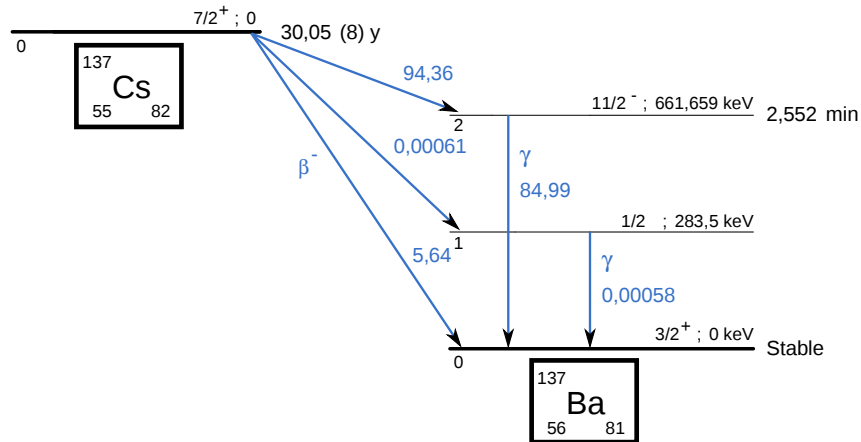


Figure 5.4:  $^{137}\text{Cs}$  decays by  $\beta^-$  emission to the ground state of  $^{137}\text{Ba}$  ( $BR = 5.64\%$ ) and via the 662 keV isomeric level of  $^{137}\text{Ba}$  ( $BR = 94.36\%$ ) whose half-life is 2.55 min.

#### 684 5.1.1.2 GIF++

685 The new Gamma Irradiation Facility (GIF++), located in the SPS North Area at the downstream end  
 686 of the H4 test beam, has replaced its predecessor during LS1 and has been operational since spring  
 687 2015 [26]. Like GIF, GIF++ features a  $^{137}\text{Cs}$  source of 662 keV gamma photons, their fluence being  
 688 controlled with a set of filters of various attenuation factors. The source provides two separated large  
 689 irradiation areas for testing several full-size muon detectors with continuous homogeneous irradiation,  
 690 as presented in Figure 5.5.

691

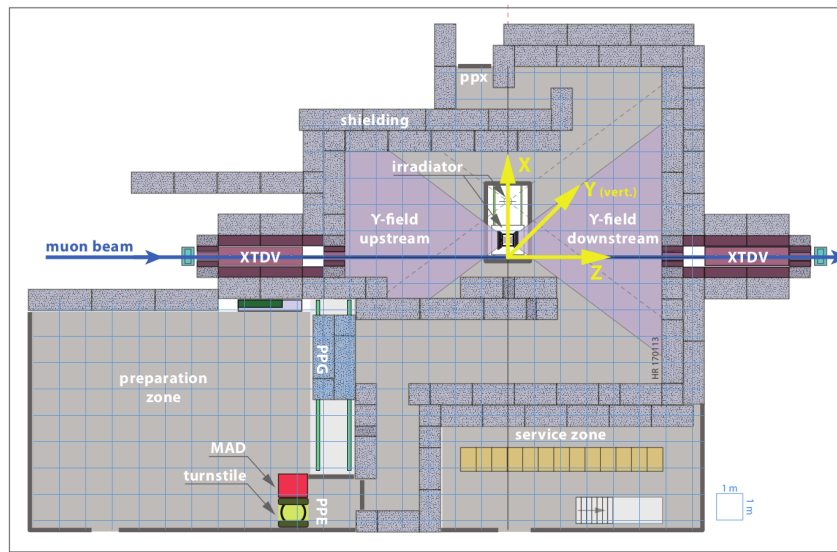


Figure 5.5: Floor plan of the GIF++ facility. When the facility downstream of the GIF++ takes electron beam, a beam pipe is installed along the beam line ( $z$ -axis). The irradiator can be displaced laterally (its center moves from  $x = 0.65$  m to 2.15 m), to increase the distance to the beam pipe.

692 The source activity was measured to be about 13.5 TBq in March 2016. The photon flux being  
 693 far greater than HL-LHC expectations, GIF++ provides an excellent facility for accelerated aging  
 694 tests of muon detectors.

695

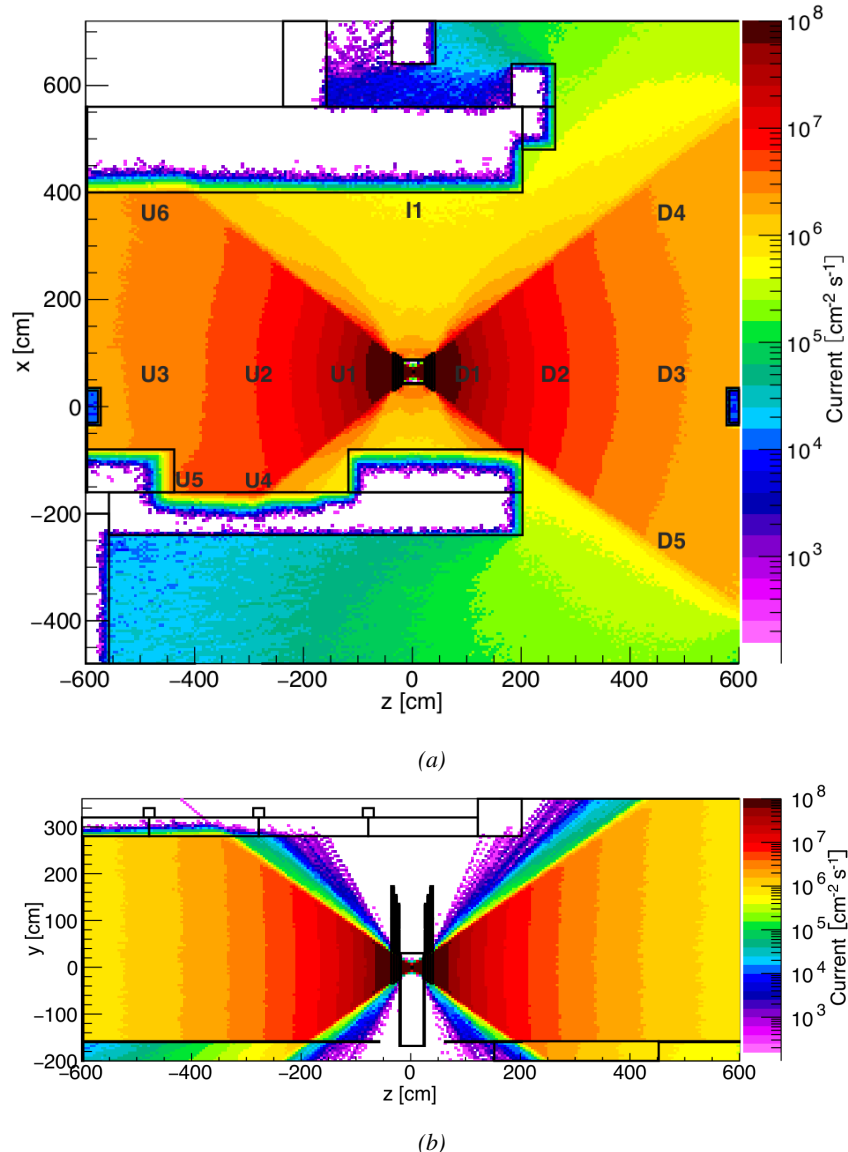


Figure 5.6: Simulated unattenuated current of photons in the xz plane (Figure 5.6a) and yz plane (Figure 5.6b) through the source at  $x = 0.65 \text{ m}$  and  $y = 0 \text{ m}$ . With angular correction filters, the current of 662 keV photons is made uniform in xy planes.

696 The source is situated in the muon beam line with the muon beam being available a few times a  
 697 year. The H4 beam, composed of muons with a momentum of about 150 GeV/c, passes through the  
 698 GIF++ zone and is used to study the performance of the detectors. Its flux is of 104 particles/ $\text{s cm}^2$

699 focused in an area similar to  $10 \times 10 \text{ cm}^2$ . Therefore, with properly adjusted filters, one can imitate  
 700 the HL-LHC background and study the performance of muon detectors with their trigger/readout  
 701 electronics in HL-LHC environment.

702

## 703 5.2 Preliminary tests at GIF

### 704 5.2.1 Resistive Plate Chamber test setup

705 During summer 2014, preliminary tests have been conducted in the GIF area on a newly produced  
 706 RE4/2 chamber labelled RE-4-2-BARC-161. This chamber has been placed into a trolley covered  
 707 with a tent. The position of the RPC inside the tent and of the tent related to the source is described  
 708 in Figure 5.7. To test this CMS RPC, three different absorber settings were used. First of all,  
 709 measurements were done with fully opened source. Then, to complete this preliminary study, the  
 710 gamma flux has been attenuated from a factor 2 and a factor 5. The expected gamma flux at the level  
 711 of our detector will be discussed in subsection ??.

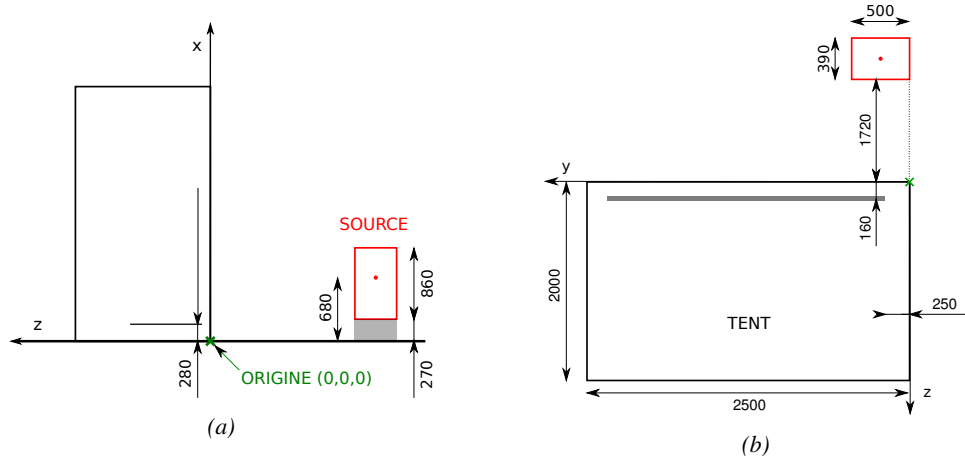
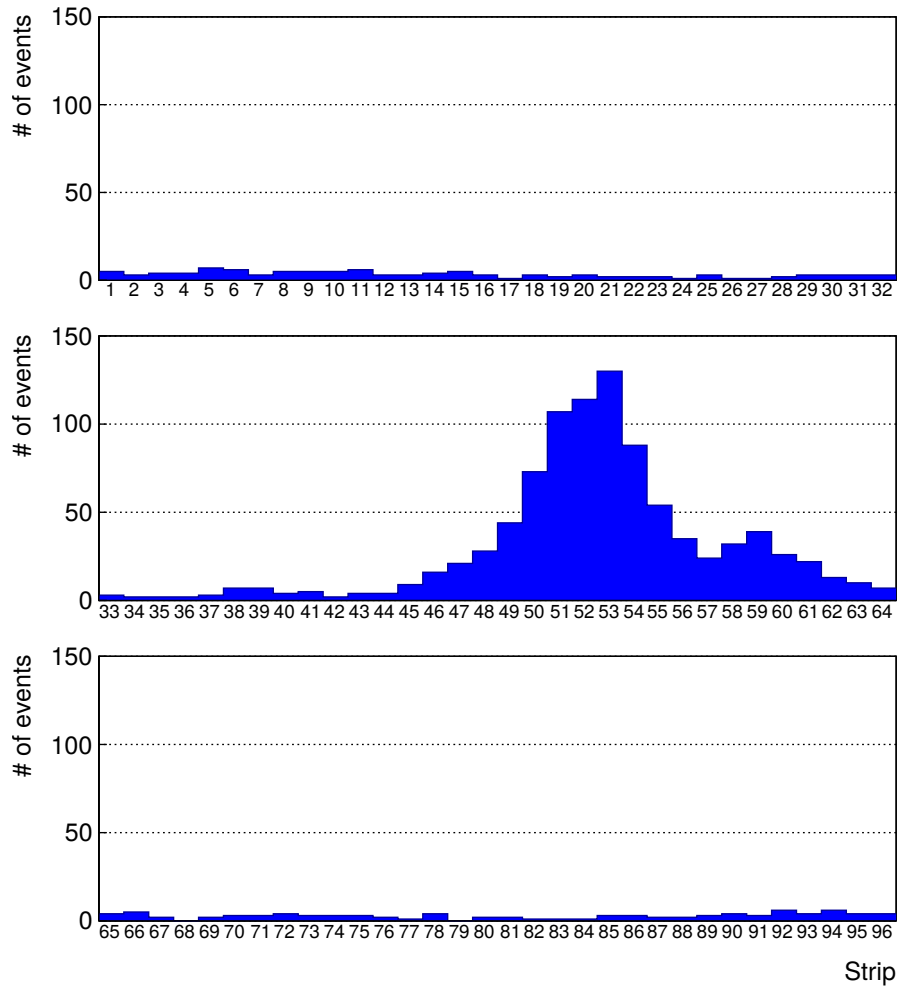


Figure 5.7: Description of the RPC setup. Dimensions are given in mm. A tent containing RPCs is placed at 1720 mm from the source container. The source is situated in the center of the container. RE-4-2-BARC-161 chamber is 160 mm inside the tent. This way, the distance between the source and the chambers plan is 2060 mm. Figure 5.7a provides a side view of the setup in the xz plane while Figure 5.7b shows a top view in the yz plane.



*Figure 5.8: RE-4-2-BARC-161 chamber is inside the tent as described in Figure 5.7. In the top right, the two scintillators used as trigger can be seen. This trigger system has an inclination of 10° relative to horizontal and is placed above half-partition B2 of the RPCs. PMT electronics are shielded thanks to lead blocks placed in order to protect them without stopping photons from going through the scintillators and the chamber.*

At the time of the tests, the beam not being operational anymore, a trigger composed of 2 plastic scintillators has been placed in front of the setup with an inclination of 10 deg with respect to the detector plane in order to look at cosmic muons. Using this particular trigger layout, shown on Figure 5.8, leads to a cosmic muon hit distribution into the chamber similar to the one in Figure 5.9. Measured without gamma irradiation, two peaks can be seen on the profil of partition B, centered on strips 52 and 59. Section ?? will help us understand that these two peaks are due respectively to forward and backward coming cosmic particles where forward coming particles are first detected by the scintillators and then the RPC while the backward coming muons are first detected in the RPC.



*Figure 5.9: Hit distributions over all 3 partitions of RE-4-2-BARC-161 chamber is showed on these plots. Top, middle and bottom figures respectively correspond to partitions A, B, and C. These plots show that some events still occur in other half-partitions than B2, which corresponds to strips 49 to 64, in front of which the trigger is placed, contributing to the inefficiency of detection of cosmic muons. In the case of partitions A and C, the very low amount of data can be interpreted as noise. On the other hand, it is clear that a little portion of muons reach the half-partition B1, corresponding to strips 33 to 48.*

### 5.2.2 Data Acquisition

### 5.2.3 Geometrical acceptance of the setup layout to cosmic muons

In order to profit from a constant gamma irradiation, the detectors inside of the GIF bunker need to be placed in a plane orthogonal to the beam line. The muon beam that used to be available was meant to test the performance of detectors under test. This beam not being active anymore, another solution to test detector performance had to be used. Thus, it has been decided to use cosmic muons detected through a telescope composed of two scintillators. Lead blocks were used as shielding to

727 protect the photomultipliers from gammas as can be seen from Figure 5.8.

728 An inclination has been given to the cosmic telescope to maximize the muon flux. A good com-  
 729 promise had to be found between good enough muon flux and narrow enough hit distribution to  
 730 be sure to contain all the events into only one half partitions as required from the limited available  
 731 readout hardware. Nevertheless, a consequence of the misplaced trigger, that can be seen as a loss  
 732 of events in half-partition B1 in Figure 5.9, is an inefficiency. Nevertheless, the inefficiency of ap-  
 733 proximately 20 % highlighted in Figure 5.10 by comparing the performance of chamber BARC-161  
 734 in 904 and at GIF without irradiation seems too important to be explained only by the geometri-  
 735 cal acceptance of the setup itself. Simulations have been conducted to show how the setup brings  
 736 inefficiency.

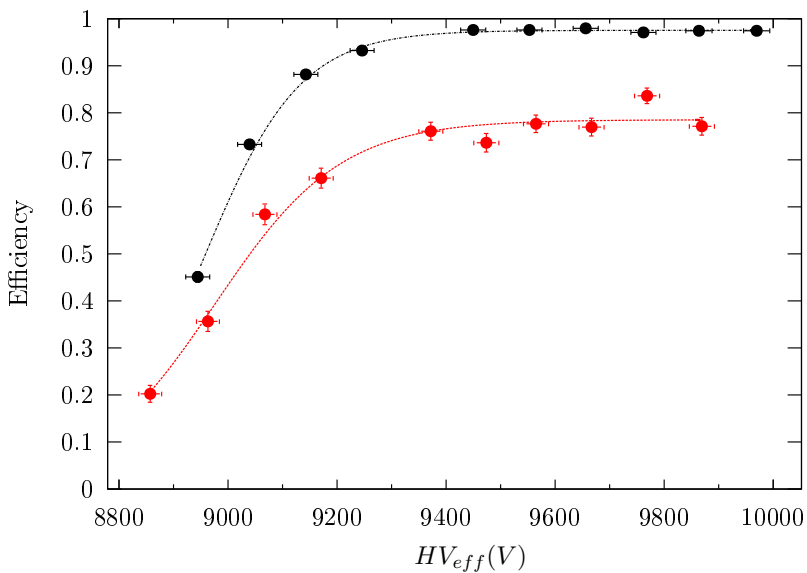
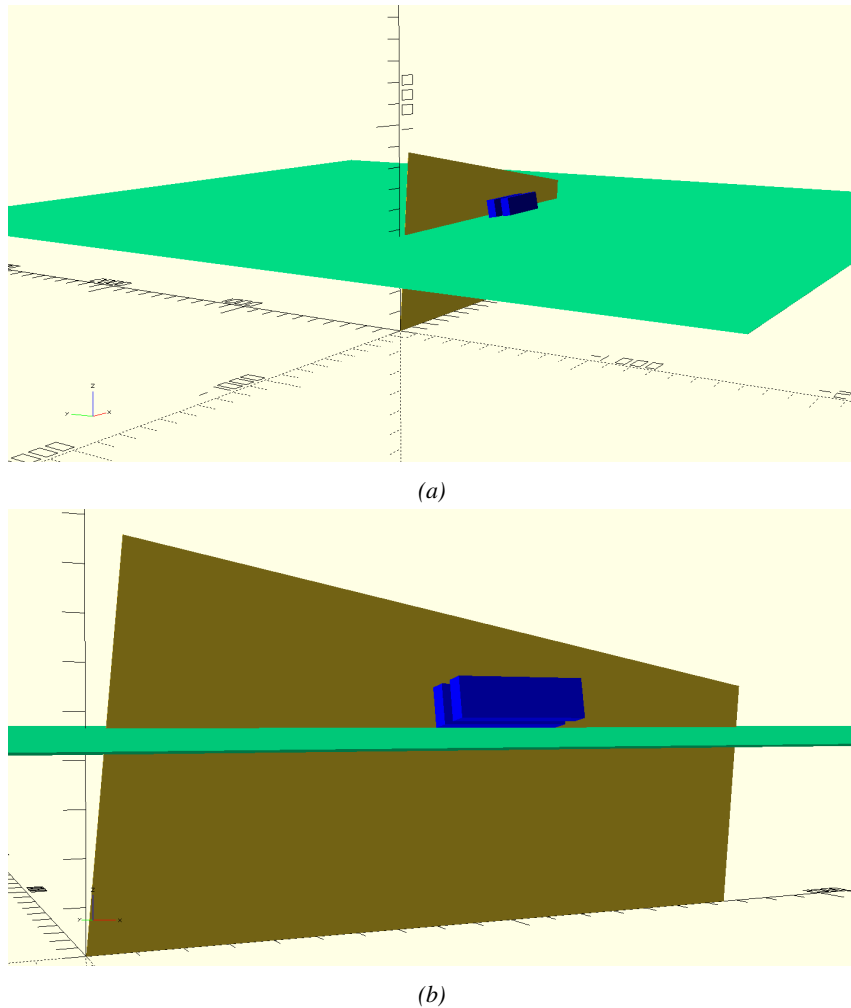


Figure 5.10: Results are derived from data taken on half-partition B2 only. On the 18<sup>th</sup> of June 2014, data has been taken on chamber RE-2-BARC-161 at building 904 (Prevessin Site) with cosmic muons providing us a reference efficiency plateau of  $(97.54 \pm 0.15)\%$  represented by a black curve. A similar measurement has been done at GIF on the 21<sup>st</sup> of July with the same chamber giving a plateau of  $(78.52 \pm 0.94)\%$  represented by a red curve.

### 737 5.2.3.1 Description of the simulation layout

738 The layout of GIF setup has been reproduced and incorporated into a Monte Carlo (MC) simulation  
 739 to study the influence of the disposition of the telescope on the final distribution measured by the  
 740 RPC. A 3D view of the simulated layout is given into Figure 5.11. Muons are generated randomly  
 741 in a horizontal plane located at a height corresponding to the lowest point of the PMTs. This way,  
 742 the needed size of the plane in order to simulate events happening at very big azimuthal angles (i.e.  
 743  $\theta \approx \pi$ ) can be kept relatively small. The muon flux is designed to follow the usual  $\cos^2\theta$  distribution  
 744 for cosmic particle. The goal of the simulation is to look at muons that pass through the muon  
 745 telescope composed of the two scintillators and define their distribution onto the RPC plane. During  
 746 the reconstruction, the RPC plane is then divided into its strips and each muon track is assigned to a  
 747 strip.



*Figure 5.11: Representation of the layout used for the simulations of the test setup. The RPC is represented as a yellow trapezoid while the two scintillators as blue cuboids looking at the sky. A green plane corresponds to the muon generation plane within the simulation. Figure 5.7a shows a global view of the simulated setup. Figure 5.7b shows a zoomed view that allows to see the 2 scintillators as well as the full RPC plane.*

748 In order to further refine the quality of the simulation and understand deeper the results the  
 749 dependance of the distribution has been studied for a range of telescope inclinations. Moreover,  
 750 the threshold applied on the PMT signals has been included into the simulation in the form of a  
 751 cut. In the approximation of uniform scintillators, it has been considered that the threshold can be  
 752 understood as the minimum distance particles need to travel through the scintillating material to give  
 753 a strong enough signal. Particles that travel a distance smaller than the set "threshold" are thus not  
 754 detected by the telescope and cannot trigger the data taking. Finally, the FEE threshold also has  
 755 been considered in a similar way. The mean momentum of horizontal cosmic rays is higher than  
 756 those of vertical ones but the stopping power of matter for momenta ranging from 1 GeV to 1 TeV  
 757 stays comparable. It is then possible to assume that the mean number of primary  $e^-/ion$  pairs per  
 758 unit length will stay similar and thus, depending on the applied discriminator threshold, muons with

759 the shortest path through the gas volume will deposit less charge and induce a smaller signal on the  
 760 pick-up strips that could eventually not be detected. These two thresholds also restrain the overall  
 761 geometrical acceptance of the system.

762 **5.2.3.2 Simulation procedure**

763 The simulation software has been designed using C++ and the output data is saved into ROOT  
 764 histograms. Simulations start for a threshold  $T_{scint}$  varying in a range from 0 to 45 mm in steps  
 765 of 5 mm, where  $T_{scint} = 0$  mm corresponds to the case where there isn't any threshold apply on  
 766 the input signal while  $T_{scint} = 45$  mm, which is the scintillator thickness, is the case where muons  
 767 cannot arrive orthogonally onto the scintillator surface. For a given  $T_{scint}$ , a set of RPC thresholds  
 768 are considered. The RPC threshold,  $T_{RPC}$  varies from 2 mm, the thickness of the gas volume, to  
 769 3 mm in steps of 0.25 mm. For each  $(T_{scint}; T_{RPC})$  pair,  $N_\mu = 10^8$  muons are randomly generated  
 770 inside the muon plane described in the previous paragraph with an azimuthal angle  $\theta$  chosen to follow  
 771 a  $\cos^2\theta$  distribution.

772 Planes are associated to each surface of the scintillators. Knowing muon position into the muon  
 773 plane and its direction allows us, by assuming that muons travel in a straight line, to compute the  
 774 intersection of the muon track with these planes. Applying conditions to the limits of the surfaces  
 775 of the scintillator faces then gives us an answer to whether or not the muon passed through the  
 776 scintillators. In the case the muon has indeed passed through the telescope, the path through each  
 777 scintillator is computed and muons whose path was shorter than  $T_{scint}$  are rejected and are thus  
 778 considered as having not interacted with the setup.

779 On the contrary, if the muon is labeled as good, its position within the RPC plane is computed  
 780 and the corresponding strip, determined by geometrical tests in the case the distance through the  
 781 gas volume was enough not to be rejected because of  $T_{RPC}$ , gets a hit and several histograms  
 782 are filled in order to keep track of the generation point on the muon plane, the intersection points  
 783 of the reconstructed muons within the telescope, or on the RPC plane, the path traveled through  
 784 each individual scintillator or the gas volume, as well as other histograms. Moreover, muons fill  
 785 different histograms whether they are forward or backward coming muons. They are discriminated  
 786 according to their direction components. When a muon is generated, an  $(x, y, z)$  position is assigned  
 787 into the muon plane as well as a  $(\theta; \phi)$  pair that gives us the direction it's coming from. This way,  
 788 muons satisfying the condition  $0 \leq \phi < \pi$  are designated as backward coming muons while muons  
 789 satisfying  $\pi \leq \phi < 2\pi$  as forward coming muons.

790 This simulation is then repeated for different telescope inclinations ranging in between 4 and  $20^\circ$   
 791 and varying in steps of  $2^\circ$ . Due to this inclination and to the vertical position of the detector under  
 792 test, the muon distribution reconstructed in the detector plane is asymmetrical. The choice as been  
 793 made to chose a skew distribution formula to fit the data built as the multiplication of gaussian and  
 794 sigmoidal curves together. A typical gaussian formula is given as 5.1 and has three free parameters  
 795 as  $A_g$ , its amplitude,  $\bar{x}$ , its mean value and  $\sigma$ , its root mean square. Sigmoidal curves as given by  
 796 formula 5.2 are functions converging to 0 and  $A_s$  as  $x$  diverges. The inflection point is given as  $x_i$   
 797 and  $\lambda$  is proportional to the slope at  $x = x_i$ . In the limit where  $\lambda \rightarrow \infty$ , the sigmoid becomes a  
 798 step function.

$$g(x) = A_g e^{-\frac{(x-\bar{x})^2}{2\sigma^2}} \quad (5.1)$$

$$s(x) = \frac{A_s}{1 + e^{-\lambda(x-x_i)}} \quad (5.2)$$

Finally, a possible representation of a skew distribution is given by formula 5.3 and is the product of 5.1 and 5.2. Naturally, here  $A_{sk} = A_g \times A_s$  and represents the theoretical maximum in the limit where the skew tends to a gaussian function.

$$sk(x) = g(x) \times s(x) = A_{sk} \frac{e^{\frac{-(x-\bar{x})^2}{2\sigma^2}}}{1 + e^{-\lambda(x-x_i)}} \quad (5.3)$$

### 5.2.3.3 Results

#### 803 Influence of $T_{scint}$ on the muon distribution

#### 804 Influence of $T_{RPC}$ on the muon distribution

#### 805 Influence of the telescope inclination on the muon distribution

#### 806 Comparison to data taken at GIF without irradiation

### 5.2.4 Photon flux at GIF

#### 808 5.2.4.1 Expectations from simulations

In order to understand and evaluate the  $\gamma$  flux in the GIF area, simulations had been conducted in 1999 and published by S. Agosteo et al [25]. Table 5.1 presented in this article gives us the  $\gamma$  flux for different distances  $D$  to the source. This simulation was done using GEANT and a Monte Carlo N-Particle (MCNP) transport code, and the flux  $F$  is given in number of  $\gamma$  per unit area and unit time along with the estimated error from these packages expressed in %.

Nominal ABS	Photon flux $F$ [ $s^{-1}cm^{-2}$ ]			
	at $D = 50$ cm	at $D = 155$ cm	at $D = 300$ cm	at $D = 400$ cm
1	$0.12 \cdot 10^8 \pm 0.2\%$	$0.14 \cdot 10^7 \pm 0.5\%$	$0.45 \cdot 10^6 \pm 0.5\%$	$0.28 \cdot 10^6 \pm 0.5\%$
2	$0.68 \cdot 10^7 \pm 0.3\%$	$0.80 \cdot 10^6 \pm 0.8\%$	$0.25 \cdot 10^6 \pm 0.8\%$	$0.16 \cdot 10^6 \pm 0.6\%$
5	$0.31 \cdot 10^7 \pm 0.4\%$	$0.36 \cdot 10^6 \pm 1.2\%$	$0.11 \cdot 10^6 \pm 1.2\%$	$0.70 \cdot 10^5 \pm 0.9\%$

Table 5.1: Total photon flux ( $E\gamma \leq 662$  keV) with statistical error predicted considering a  $^{137}Cs$  activity of 740 GBq at different values of the distance  $D$  to the source along the  $x$ -axis of irradiation field [25].

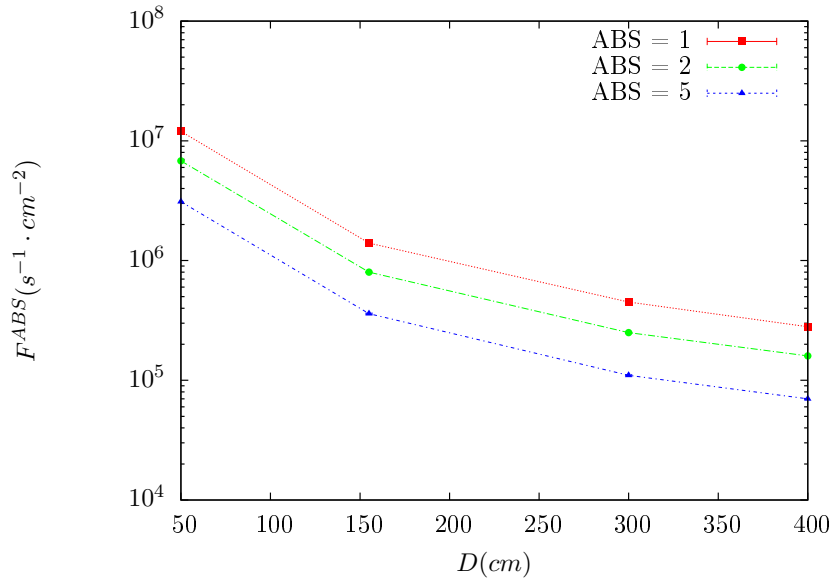


Figure 5.12:  $\gamma$  flux  $F(D)$  is plot using values from table 5.1. As expected, the plot shows similar attenuation behaviours with increasing distance for each absorption factors.

The simulation doesn't directly provides us with an estimated flux at the level of our RPC. First of all, it is needed to extract the value of the flux from the available data contained in the original paper and then to estimate the flux in 2014 at the time the experimentation took place. Figure 5.12 that contains the data from Table 5.1. In the case of a pointlike source emitting isotropic and homogeneous gamma radiations, the gamma flux  $F$  at a distance  $D$  to the source with respect to a reference point situated at  $D_0$  where a known flux  $F_0$  is measured will be expressed like in Equation 5.4, assuming that the flux decreases as  $1/D^2$ , where  $c$  is a fitting factor.

$$F^{ABS} = F_0^{ABS} \times \left( \frac{cD_0}{D} \right)^2 \quad (5.4)$$

By rewriting Equation 5.4, it comes that :

$$c = \frac{D}{D_0} \sqrt{\frac{F^{ABS}}{F_0^{ABS}}} \quad (5.5)$$

$$\Delta c = \frac{c}{2} \left( \frac{\Delta F^{ABS}}{F^{ABS}} + \frac{\Delta F_0^{ABS}}{F_0^{ABS}} \right) \quad (5.6)$$

Finally, using Equation 5.5 and the data in Table 5.1 with  $D_0 = 50$  cm as reference point, we can build Table 5.2. It is interesting to note that  $c$  for each value of  $D$  doesn't depend on the absorption factor.

Nominal ABS	Correction factor $c$		
	at $D = 155$ cm	at $D = 300$ cm	at $D = 400$ cm
1	$1.059 \pm 0.70\%$	$1.162 \pm 0.70\%$	$1.222 \pm 0.70\%$
2	$1.063 \pm 1.10\%$	$1.150 \pm 1.10\%$	$1.227 \pm 0.90\%$
5	$1.056 \pm 1.60\%$	$1.130 \pm 1.60\%$	$1.202 \pm 1.30\%$

Table 5.2: Correction factor  $c$  is computed thanks to formulae 5.5 taking as reference  $D_0 = 50$  cm and the associated flux  $F_0^{ABS}$  for each absorption factor available in table 5.1.

825 For the range of  $D/D_0$  values available, it is possible to use a simple linear fit to get the evolution  
 826 of  $c$ . The linear fit will then use only 2 free parameters,  $a$  and  $b$ , as written in Equation 5.7. This gives  
 827 us the results showed in Figure 5.13. Figure 5.13b confirms that using only a linear fit to extract  $c$  is  
 828 enough as the evolution of the rate that can be obtained superimposes well on the simulation points.

$$c \left( \frac{D}{D_0} \right) = a \frac{D}{D_0} + b \quad (5.7)$$

$$F^{ABS} = F_0^{ABS} \left( a + \frac{bD_0}{D} \right)^2 \quad (5.8)$$

$$\Delta F^{ABS} = F^{ABS} \left[ \frac{\Delta F_0^{ABS}}{F_0^{ABS}} + 2 \frac{\Delta a + \Delta b \frac{D_0}{D}}{a + \frac{bD_0}{D}} \right] \quad (5.9)$$

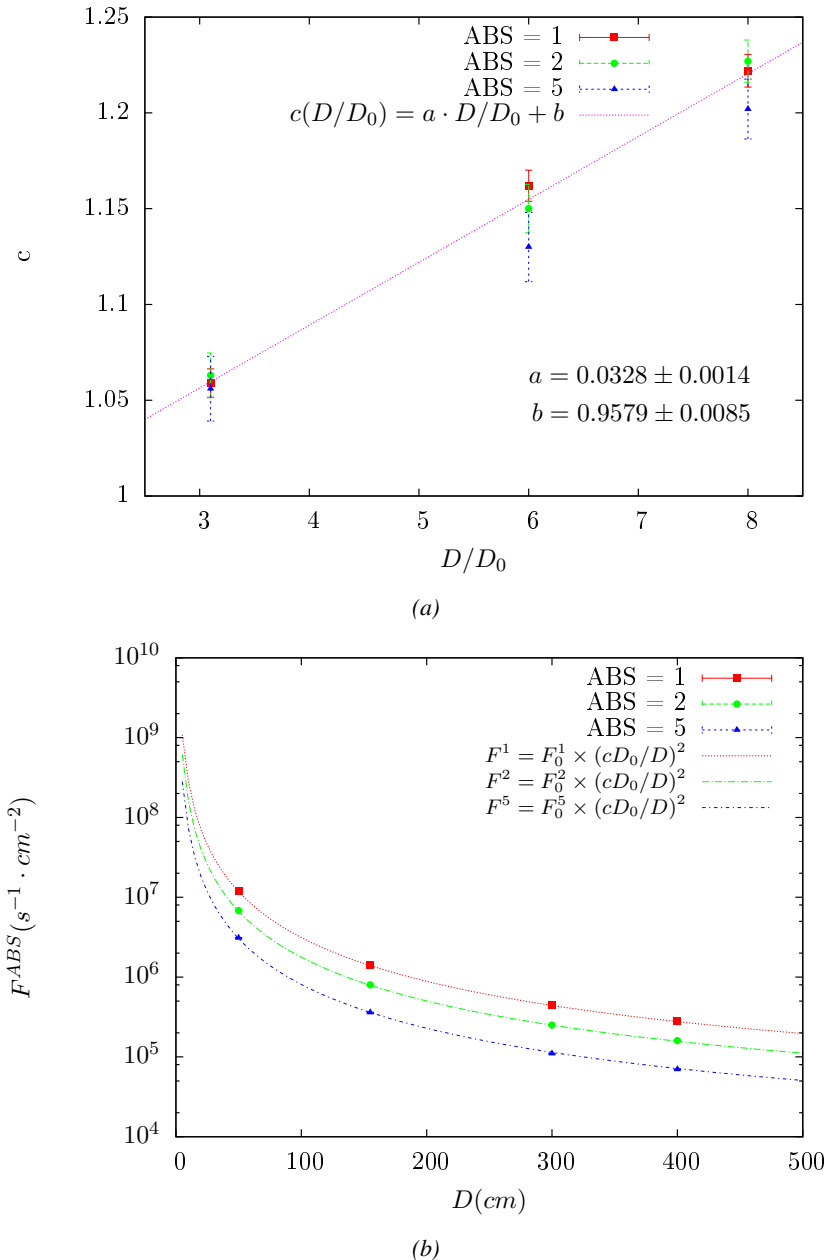


Figure 5.13: Figure 5.13a shows the linear approximation fit done via formulae 5.7 on data from table 5.2. Figure 5.13b shows a comparison of this model with the simulated flux using  $a$  and  $b$  given in figure 5.13a in formulae 5.4 and the reference value  $D_0 = 50\text{cm}$  and the associated flux for each absorption factor  $F_0^{ABS}$  from table 5.1

In the case of the 2014 GIF tests, the RPC plane is located at a distance  $D = 206\text{ cm}$  to the source. Moreover, to estimate the strength of the flux in 2014, it is necessary to consider the nuclear decay through time associated to the Cesium source whose half-life is well known ( $t_{1/2} = (30.05 \pm 0.08)\text{ y}$ ). The very first source activity measurement has been done on the 5<sup>th</sup> of March 1997 while the GIF

833 tests where done in between the 20<sup>th</sup> and the 31<sup>st</sup> of August 2014, i.e. at a time  $t = (17.47 \pm 0.02)$  y  
 834 resulting in an attenuation of the activity from 740 GBq in 1997 to 494 GBq in 2014. All the needed  
 835 information to extrapolate the flux through our detector in 2014 has now been assembled, leading  
 836 to the Table 5.3. It is interesting to note that for a common RPC sensitivity to  $\gamma$  of  $2 \cdot 10^{-3}$ , the  
 837 order of magnitude of the estimated hit rate per unit area is of the order of the kHz for the fully  
 838 opened source. Moreover, taking profit of the two working absorbers, it will be possible to scan  
 839 background rates at 0 Hz,  $\sim 300$  Hz as well as  $\sim 600$  Hz. Without source, a good estimate of the  
 840 intrinsic performance will be available. Then at 300 Hz, the goal will be to show that the detectors  
 841 fulfill the performance certification of CMS RPCs. Then a first idea of the performance of the  
 842 detectors at higher background will be provided with absorption factors 2 ( $\sim 600$  Hz) and 1 (no  
 843 absorption). *[Here I will also put a reference to the plot showing the estimated background rate at  
 844 the level of RE3/1 in the case of HL-LHC but this one being in another chapter, I will do it later.]*

Nominal ABS	Photon flux $F$ [ $s^{-1}cm^{-2}$ ]			Hit rate/unit area [ $Hz cm^{-2}$ ] at $D^{2014} = 206$ cm
	at $D_0^{1997} = 50$ cm	at $D^{1997} = 206$ cm	at $D^{2014} = 206$ cm	
1	$0.12 \cdot 10^8 \pm 0.2\%$	$0.84 \cdot 10^6 \pm 0.3\%$	$0.56 \cdot 10^6 \pm 0.3\%$	$1129 \pm 32$
2	$0.68 \cdot 10^7 \pm 0.3\%$	$0.48 \cdot 10^6 \pm 0.3\%$	$0.32 \cdot 10^6 \pm 0.3\%$	$640 \pm 19$
5	$0.31 \cdot 10^7 \pm 0.4\%$	$0.22 \cdot 10^6 \pm 0.3\%$	$0.15 \cdot 10^6 \pm 0.3\%$	$292 \pm 9$

Table 5.3: The data at  $D_0$  in 1997 is taken from [25]. In a second step, using Equations 5.8 and 5.9, the flux at  $D$  can be estimated in 1997. Then, taking into account the attenuation of the source activity, the flux at  $D$  can be estimated at the time of the tests in GIF in 2014. Finally, assuming a sensitivity of the RPC to  $\gamma$   $s = 2 \cdot 10^{-3}$ , an estimation of the hit rate per unit area is obtained.

845    **5.2.4.2 Dose measurements**

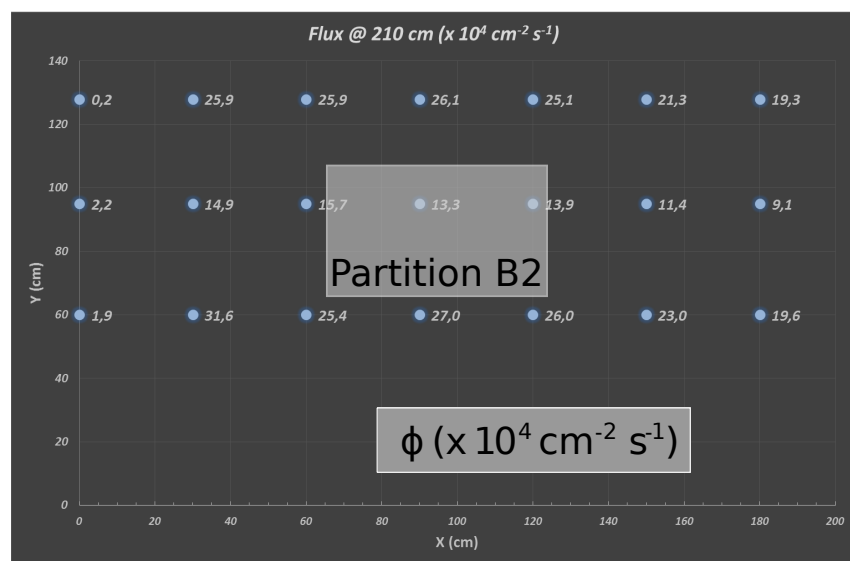


Figure 5.14: Dose measurements has been done in a plane corresponding to the tents front side. This plan is 1900 mm away from the source. As explained in the first chapter, a lens-shaped lead filter provides a uniform photon flux in the vertical plan orthogonal to the beam direction. If the second line of measured fluxes is not taken into account because of lower values due to experimental equipments in the way between the source and the tent, the uniformity of the flux is well showed by the results.

<sup>846</sup> **5.2.5 Results and discussions**

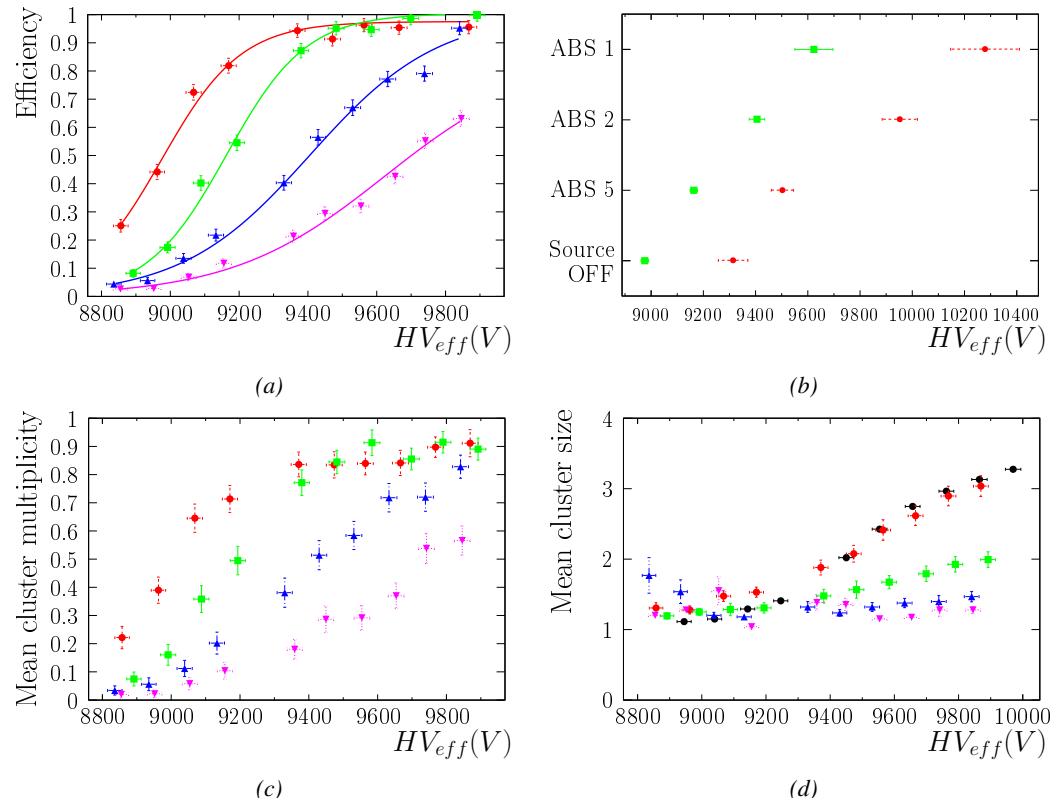


Figure 5.15

### <sup>847</sup> 5.3 Longevity tests at GIF++

<sup>848</sup> Longevity studies imply a monitoring of the performance of the detectors probed using a high inten-  
<sup>849</sup> sity muon beam in a irradiated environment by periodically measuring their rate capability, the dark  
<sup>850</sup> current running through them and the bulk resistivity of the Bakelite composing their electrodes.  
<sup>851</sup> GIF++, with its very intense  $^{137}\text{Cs}$  source, provides the perfect environment to perform such kind  
<sup>852</sup> of tests. Assuming a maximum acceleration factor of 3, it is expected to accumulate the equivalent  
<sup>853</sup> charge in 1.7 years.

<sup>854</sup> As the maximum background is found in the endcap, the choice naturally was made to focus the  
<sup>855</sup> GIF++ longevity studies on endcap chambers. Most of the RPC system was installed in 2007. Nev-  
<sup>856</sup> ertheless, the large chambers in the fourth endcap (RE4/2 and RE4/3) have been installed during  
<sup>857</sup> LS1 in 2014. The Bakelite of these two different productions having different properties, four spare  
<sup>858</sup> chambers of the present system were selected, two RE2,3/2 spares and two RE4/2 spares. Having  
<sup>859</sup> two chambers of each type allows to always keep one of them non irradiated as reference, the per-  
<sup>860</sup> formance evolution of the irradiated chamber being then compared through time to the performance  
<sup>861</sup> of the non irradiated one.

<sup>862</sup> The performance of the detectors under different level of irradiation is measured periodically dur-  
<sup>863</sup> ing dedicated test beam periods using the H4 muon beam. In between these test beam periods, the  
<sup>864</sup> two RE2,3/2 and RE4/2 chambers selected for this study are irradiated by the  $^{137}\text{Cs}$  source in order  
<sup>865</sup> to accumulate charge and the gamma background is monitored, as well as the currents. The two  
<sup>866</sup> remaining chambers are kept non-irradiated as reference detectors. Due to the limited gas flow in  
<sup>867</sup> GIF++, the RE4 chamber remained non-irradiated until end of November 2016 where a new mass  
<sup>868</sup> flow controller has been installed allowing for bigger volumes of gas to flow in the system.

<sup>869</sup> Figures 5.16 and 5.17 give us for different test beam periods, and thus for increasing integrated  
<sup>870</sup> charge through time, a comparison of the maximum efficiency, obtained using a sigmoid-like func-  
<sup>871</sup> tion, and of the working point of both irradiated and non irradiated chambers [27]. No aging is yet  
<sup>872</sup> to see from this data, the shifts in  $\gamma$  rate per unit area in between irradiated and non irradiated detec-  
<sup>873</sup> tors and RE2 and RE4 types being easily explained by a difference of sensitivity due to the various  
<sup>874</sup> Bakelite resistivities of the HPL electrodes used for the electrode production.

<sup>875</sup> Collecting performance data at each test beam period allows us to extrapolate the maximum effi-  
<sup>876</sup> ciency for a background hit rate of  $300\text{ Hz}/\text{cm}^2$  corresponding to the expected HL-LHC conditions.  
<sup>877</sup> Aging effects could emerge from a loss of efficiency with increasing integrated charge over time,  
<sup>878</sup> thus Figure 5.18 helps us understand such degradation of the performance of irradiated detectors in  
<sup>879</sup> comparison with non irradiated ones. The final answer for an eventual loss of efficiency is given in  
<sup>880</sup> Figure 5.19 by comparing for both irradiated and non irradiated detectors the efficiency sigmoids  
<sup>881</sup> before and after the longevity study. Moreover, to complete the performance information, the Bake-  
<sup>882</sup> lite resistivity is regularly measured thanks to  $Ag$  scans (Figure 5.20) and the noise rate is monitored  
<sup>883</sup> weekly during irradiation periods (Figure 5.21). At the end of 2016, no signs of aging were observed  
<sup>884</sup> and further investigation is needed to get closer to the final integrated charge requirements proposed  
<sup>885</sup> for the longevity study of the present CMS RPC sub-system.

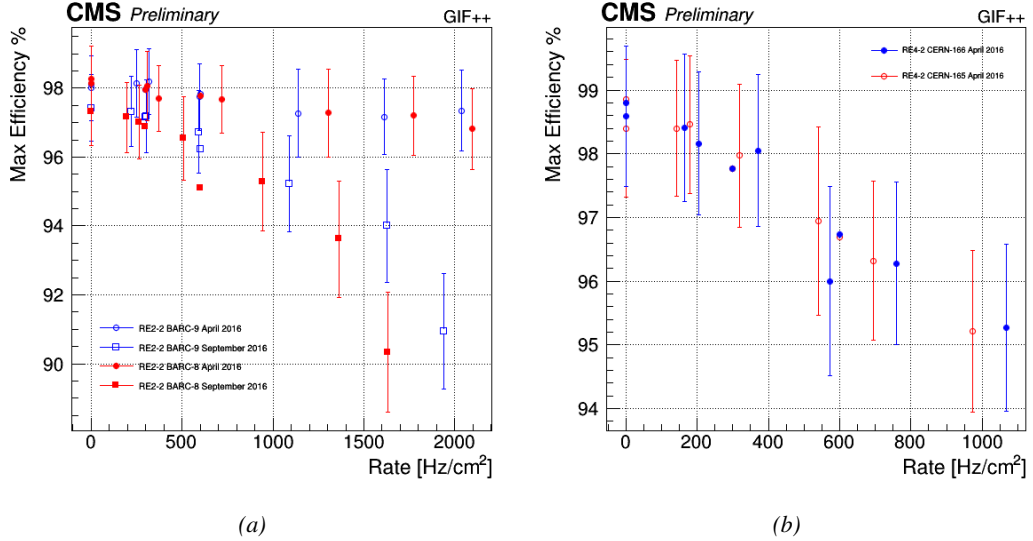


Figure 5.16: Evolution of the maximum efficiency for RE2 (5.16a) and RE4 (5.16b) chambers with increasing extrapolated  $\gamma$  rate per unit area at working point. Both irradiated (blue) and non irradiated (red) chambers are shown.

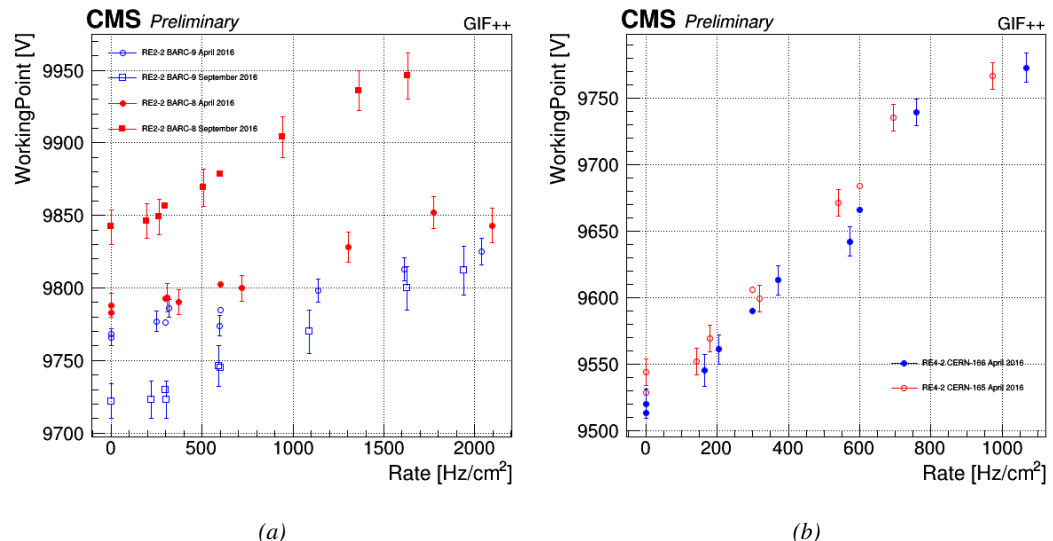
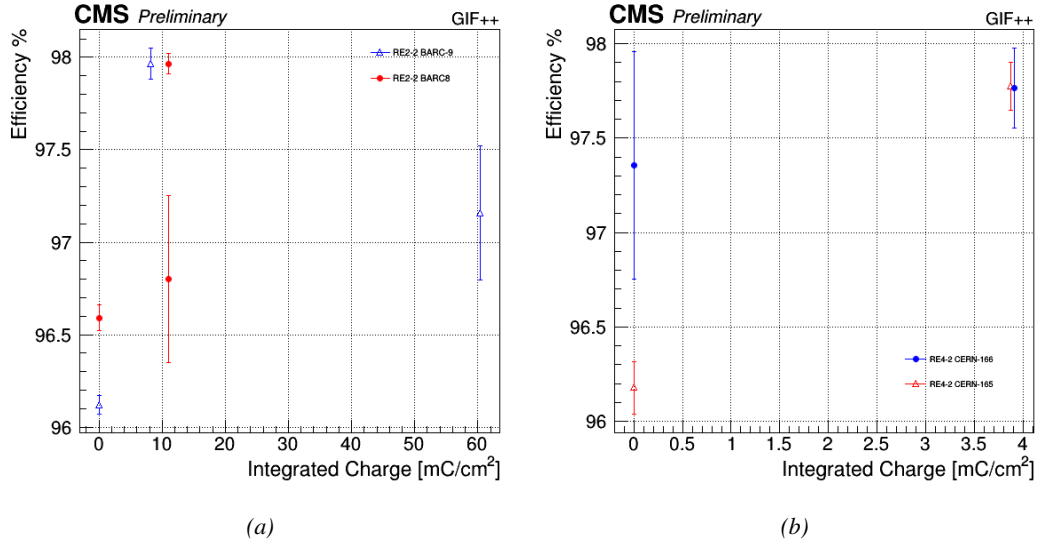
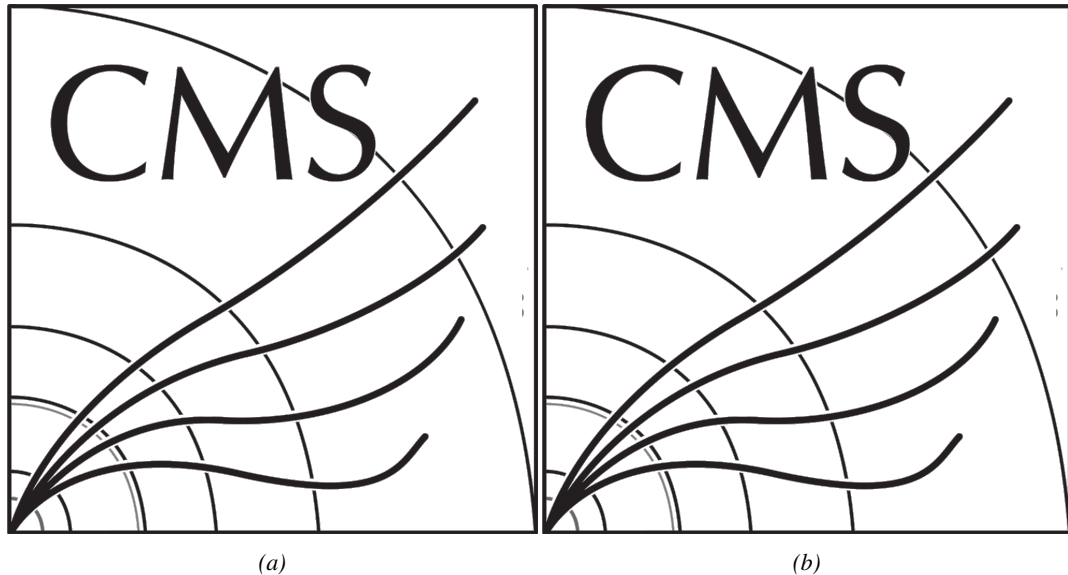


Figure 5.17: Evolution of the working point for RE2 (5.17a) and RE4 (5.17b) with increasing extrapolated  $\gamma$  rate per unit area at working point. Both irradiated (blue) and non irradiated (red) chambers are shown.



*Figure 5.18: Evolution of the maximum efficiency at HL-LHC conditions, i.e. a background hit rate per unit area of 300 Hz/cm<sup>2</sup>, with increasing integrated charge for RE2 (5.18a) and RE4 (5.18b) detectors. Both irradiated (blue) and non irradiated (red) chambers are shown. The integrated charge for non irradiated detectors is recorded during test beam periods and stays small with respect to the charge accumulated in irradiated chambers.*



*Figure 5.19: Comparison of the efficiency sigmoid before (triangles) and after (circles) irradiation for RE2 (5.19a) and RE4 (5.19b) detectors. Both irradiated (blue) and non irradiated (red) chambers are shown.*

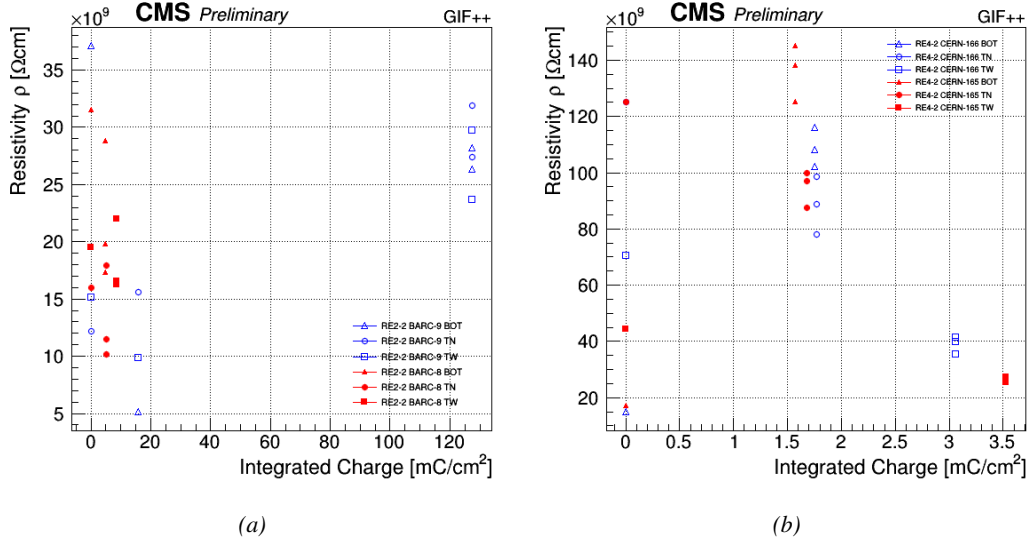


Figure 5.20: Evolution of the Bakelite resistivity for RE2 (5.20a) and RE4 (5.20b) detectors. Both irradiated (blue) and non-irradiated (red) chambers are shown.

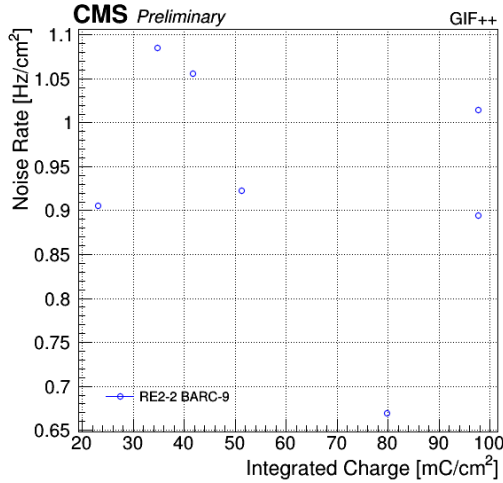


Figure 5.21: Evolution of the noise rate per unit area for the irradiated chamber RE2-2-BARC-9 only.

### 5.3.1 Description of the Data Acquisition

For the longevity studies, four spare chambers of the present system are used. Two spare RPCs of the RE2,3 stations as well as two spare RPCs from the new RE4 stations have been mounted in a Trolley. Six RE4 gaps are also placed in the trolley. The trolley is placed inside the GIFT++ in the upstream region of the bunker, taking the cesium source as a reference. The trolley is oriented for the detection surface of the chambers to be orthogonal to the beam line. The system can be moved along the orthogonal plane in order to have the beam in all  $\eta$ -partitions. For the aging the trolley is

894 moved outside the beam line and is placed in a distance of 5.2 m to the source, which irradiates the  
 895 bunker using an attenuation filter of 2.2 which corresponds to a fluence of  $10^7 \text{ gamma/cm}^2$ .

896 During GIF++ operation, the data collected can be divided into different categories as several  
 897 parameters are monitored in addition to the usual RPC performance data. On one hand, to know  
 898 the performance of a chamber, it is need to measure its efficiency and to know the background  
 899 conditions in which it is operated. To do this, the hit signals from the chamber are recorded and  
 900 stored in a ROOT file via a Data Acquisition (DAQ) software. On the other hand, it is also very  
 901 important to monitor parameters such as environmental pressure and temperature, gas temperature  
 902 and humidity, RPC HV, LV, and currents, or even source and beam status. This is done through the  
 903 GIF++ web Detector Control Software (DCS) that stores this information in a database.

904 Two different types of tests are conducted on RPCs via the DAQ. Indeed, the performance of the  
 905 detectors is measured periodically during dedicated test beam periods using the H4 muon beam. In  
 906 between these test beam periods, when the beam is not available, the chambers are irradiated by the  
 907  $^{137}\text{Cs}$  in order to accumulate deposited charge and the gamma background is measured.

908 RPCs under test are connected through LVDS cables to V1190A Time-to-Digital Converter  
 909 (TDC) modules manufactured by CAEN. These modules, located in the rack area outside of the  
 910 bunker, get the logic signals sent by the chambers and save them into their buffers. Due to the  
 911 limited size of the buffers, the collected data is regularly erased and replaced. A trigger signal is  
 912 needed for the TDC modules to send the useful data to the DAQ computer via a V1718 CAEN USB  
 913 communication module.

914 In the case of performance test, the trigger signal used for data acquisition is generated by the  
 915 coincidence of three scintillators. A first one is placed upstream outside of the bunker, a second one  
 916 is placed downstream outside of the bunker, while a third one is placed in front of the trolley, close by  
 917 the chambers. Every time a trigger is sent to the TDCs, i.e. every time a muon is detected, knowing  
 918 the time delay in between the trigger and the RPC signals, signals located in the right time window  
 919 are extracted from the buffers and saved for later analysis. Signals are taken in a time window of  
 920 400 ns centered on the muon peak (here we could show a time spectrum). On the other hand, in the  
 921 case of background rate measurement, the trigger signal needs to be "random" not to measure muons  
 922 but to look at gamma background. A trigger pulse is continuously generated at a rate of 300 Hz using  
 923 a dual timer. To integrate an as great as possible time, all signals contained within a time window of  
 924 10us prior to the random trigger signal are extracted form the buffers and saved for further analysis  
 925 (here another time spectrum to illustrate could be useful, maybe even place both spectrum together  
 926 as a single Figure).

927 The signals sent to the TDCs correspond to hit collections in the RPCs. When a particle hits  
 928 a RPC, it induce a signal in the pickup strips of the RPC readout. If this signal is higher than the  
 929 detection threshold, a LVDS signal is sent to the TDCs. The data is then organised into 4 branches  
 930 keeping track of the event number, the hit multiplicity for the whole setup, and the time and channel  
 931 profile of the hits in the TDCs.

### 932 **5.3.2 RPC current, environmental and operation parameter monitoring**

933 In order to take into account the variation of pressure and temperature between different data taking  
 934 periods the applied voltage is corrected following the relationship :

$$935 \quad HV_{eff} = HV_{app} \times \left( 0.2 + 0.8 \cdot \frac{P_0}{P} \times \frac{T}{T_0} \right) \quad (5.10)$$

935 where  $T_0$  (=293 K) and  $P_0$  (=990 mbar) are the reference values.

936 **5.3.3 Measurement procedure**

937 Insert a short description of the online tools (DAQ, DCS, DQM).

938 Insert a short description of the offline tools : tracking and efficiency algorithm.

939 Identify long term aging effects we are monitoring the rates per strip.

940 **5.3.4 Longevity studies results**



# 6

941

942

## Investigation on high rate RPCs

943 **6.1 Rate limitations and ageing of RPCs**

944 **6.1.1 Low resistivity electrodes**

945 **6.1.2 Low noise front-end electronics**

946 **6.2 Construction of prototypes**

947 **6.3 Results and discussions**



# 7

948

949

## Conclusions and outlooks

950 **7.1 Conclusions**

951 **7.2 Outlooks**



## References

- 953 [1] CERN. Geneva. LHC Experiments Committee. *The CMS muon project : Technical Design*  
 954 *Report*. Tech. rep. CERN-LHCC-97-032. CMS Collaboration, 1997.
- 955 [2] CERN. Geneva. LHC Experiments Committee. *Technical Proposal for the Phase-II Upgrade*  
 956 *of the CMS Detector*. Tech. rep. CERN-LHCC-2015-010. CMS Collaboration, 2015.
- 957 [3] CERN. Geneva. LHC Experiments Committee. *CMS, the Compact Muon Solenoid : technical*  
 958 *proposal*. Tech. rep. CERN-LHCC-94-38. CMS Collaboration, 1994.
- 959 [4] R. Santonico and R. Cardarelli. “Development of resistive plate counters”. In: *Nucl. Instr.*  
 960 *Meth. Phys. Res.* 187 (1981), pp. 377–380.
- 961 [5] Yu.N. Pestov and G.V. Fedotovich. *A picosecond time-of-flight spectrometer fot eh VEPP-2M*  
 962 *based on local-discharge spark counter*. Tech. rep. SLAC-TRANS-0184. SLAC, 1978.
- 963 [6] W.W. Ash, ed. *Spark Counter With A Localized Discharge*. Vol. SLAC-R-250. 1982, pp. 127–  
 964 131.
- 965 [7] I. Crotty et al. “The non-spark mode and high rate operation of resistive parallel plate cham-  
 966 bers”. In: *NIMA* 337 (1993), pp. 370–381.
- 967 [8] I. Crotty et al. “Further studies of avalanche mode operation of resistive parallel plate cham-  
 968 bers”. In: *NIMA* 346 (1994), pp. 107–113.
- 969 [9] R. Cardarelli et al. “Avalanche and streamer mode operation of resistive plate chambers”. In:  
 970 *NIMA* 382 (1996), pp. 470–474.
- 971 [10] E. Cerron Zeballos et al. “A new type of resistive plate chamber: The multigap RPC”. In:  
 972 *NIMA* 374 (1996), pp. 132–135.
- 973 [11] M.C.S.Williams. “The development of the multigap resistive plate chamber”. In: *Nucl. Phys.*  
 974 *B* 61 (1998), pp. 250–257.
- 975 [12] H. Czyrkowski et al. “New developments on resistive plate chambers for high rate operation”.  
 976 In: *NIMA* 419 (1998), pp. 490–496.
- 977 [13] P. Camarri et al. “Streamer suppression with SF6 in RPCs operated in avalanche mode”. In:  
 978 *NIMA* 414 (1998), pp. 317–324.
- 979 [14] E. Cerron Zeballos et al. “Effect of adding SF6 to the gas mixture in a multigap resistive plate  
 980 chamber”. In: *NIMA* 419 (1998), pp. 475–478.
- 981 [15] CERN. Geneva. LHC Experiments Committee. *ATLAS muon spectrometer: Technical design*  
 982 *report*. Tech. rep. CERN-LHCC-97-22. ATLAS Collaboration, 1997.
- 983 [16] CERN. Geneva. LHC Experiments Committee. *ALICE Time-Of-Flight system (TOF) : Tech-*  
 984 *nical Design Report*. Tech. rep. CERN-LHCC-2000-012. ALICE Collaboration, 2000.
- 985 [17] The CALICE collaboration. “First results of the CALICE SDHCAL technological proto-  
 986 type”. In: *JINST* 11 (2016).

- 987 [18] PoS, ed. *Density Imaging of Volcanoes with Atmospheric Muons using GRPCs*. International  
988 Europhysics Conference on High Energy Physics - HEP 2011. 2011.
- 989 [19] C. Lippmann. “Detector Physics of Resistive Plate Chambers”. PhD thesis. Johann Wolfgang  
990 Goethe-Universität, 2003.
- 991 [20] W. Riegler. “Induced signals in resistive plate chambers”. In: *NIMA* 491 (2002), pp. 258–271.
- 992 [21] M. Abbrescia et al. “Properties of C<sub>2</sub>H<sub>2</sub>F<sub>4</sub>-based gas mixture for avalanche mode operation  
993 of resistive plate chambers”. In: *NIMA* 398 (1997), pp. 173–179.
- 994 [22] G.Battistoni et al. “Sensitivity of streamer mode to single ionization electrons”. In: *NIMA*  
995 235 (1985), pp. 91–97.
- 996 [23] M. Abbrescia et al. “Study of long-term performance of CMS RPC under irradiation at the  
997 CERN GIF”. In: *NIMA* 533 (2004), pp. 102–106.
- 998 [24] H.C. Kim et al. “Quantitative aging study with intense irradiation tests for the CMS forward  
999 RPCs”. In: *NIMA* 602 (2009), pp. 771–774.
- 1000 [25] S. Agosteo et al. “A facility for the test of large-area muon chambers at high rates”. In: *NIMA*  
1001 452 (2000), pp. 94–104.
- 1002 [26] PoS, ed. *CERN GIF ++ : A new irradiation facility to test large-area particle detectors for  
1003 the high-luminosity LHC program*. Vol. TIPP2014. 2014, pp. 102–109.
- 1004 [27] M. Abbrescia et al. “Cosmic ray tests of double-gap resistive plate chambers for the CMS  
1005 experiment”. In: *NIMA* 550 (2005), pp. 116–126.
- 1006 [28] A. Fagot. *GIF++ DAQ v4.0*. 2017. URL: [https://github.com/afagot/GIF\\_DAQ](https://github.com/afagot/GIF_DAQ).
- 1007 [29] CAEN. *Mod. V1190-VX1190 A/B, 128/64 Ch Multihit TDC*. 14th ed. 2016.
- 1008 [30] CAEN. *Mod. VI718 VME USB Bridge*. 9th ed. 2009.
- 1009 [31] W-Ie-Ne-R. *VME 6021-23 VXI*. 5th ed. 2016.
- 1010 [32] Wikipedia. *INI file*. 2017. URL: [https://en.wikipedia.org/wiki/INI\\_file](https://en.wikipedia.org/wiki/INI_file).
- 1011 [33] S. Carrillo A. Fagot. *GIF++ Offline Analysis v6*. 2017. URL: [https://github.com/afagot/GIF\\_OfflineAnalysis](https://github.com/afagot/GIF_OfflineAnalysis).

# A

1013

1014

1015

## A data acquisition software for CAEN VME TDCs

1016 Certifying detectors in the perspective of HL-LHC required to develop tools for the GIF++ experiment.  
1017 Among them was the C++ Data Acquisition (DAQ) software that allows to make the communications  
1018 in between a computer and TDC modules in order to retrieve the RPC data [28]. In this  
1019 appendix, details about this software, as of how the software was written, how it functions and how  
1020 it can be exported to another similar setup, will be given.

### 1021 A.1 GIF++ DAQ file tree

1022 GIF++ DAQ source code is fully available on github at [https://github.com/afagot/GIF\\_DAQ](https://github.com/afagot/GIF_DAQ). The software requires 3 non-optional dependencies:

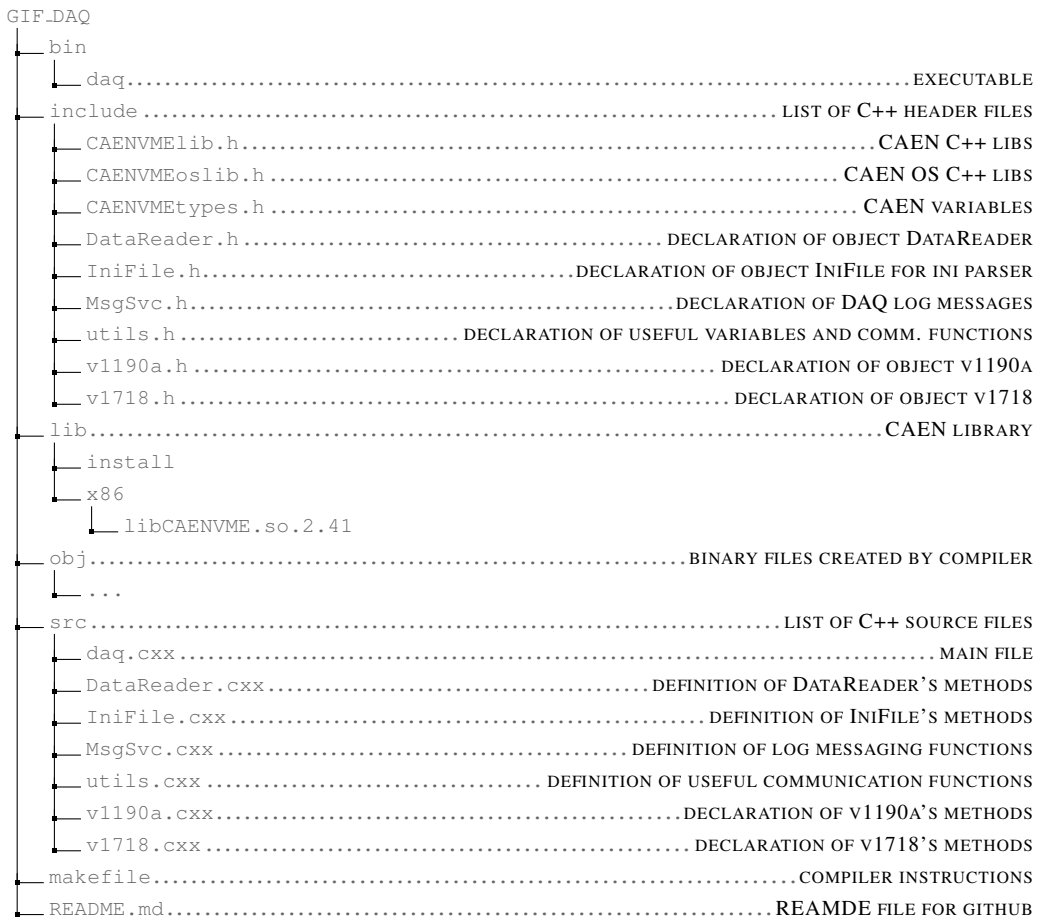
- 1024 • CAEN USB Driver, to mount the VME hardware,  
1025 • CAEN VME Library, to communicate with the VME hardware, and  
1026 • ROOT, to organize the collected data into a TTree.

1027 The CAEN VME library will not be packaged by distributions and will need to be installed man-  
1028 ually. To compile the GIF++ DAQ project via a terminal, from the DAQ folder use the command:

1029      make

1031 The source code tree is provided below along with comments to give an overview of the files' con-  
1032 tent. The different objects created for this project (`v1718`, `v1190a`, `IniFile` & `DataReader`) will be  
1033 described in details in the following sections.

1034



## 1035 A.2 Usage of the DAQ

1036 GIF++ DAQ, as used in GIF++, is not a standalone software. Indeed, the system being more complexe,  
 1037 the DAQ only is a sub-layer of the software architecture developped to control and monitor  
 1038 the RPCs that are placed into the bunker for performance study in an irradiated environment. The top  
 1039 layer of GIF++ is a Web Detector Control System (webDCS) application. The DAQ is only called  
 1040 by the webDCS when data needs to be acquired. The webDCS operates the DAQ through command  
 1041 line. To start the DAQ, the webDCS calls:

1042  
 1043   bin/daq /path/to/the/log/file/in/the/output/data/folder

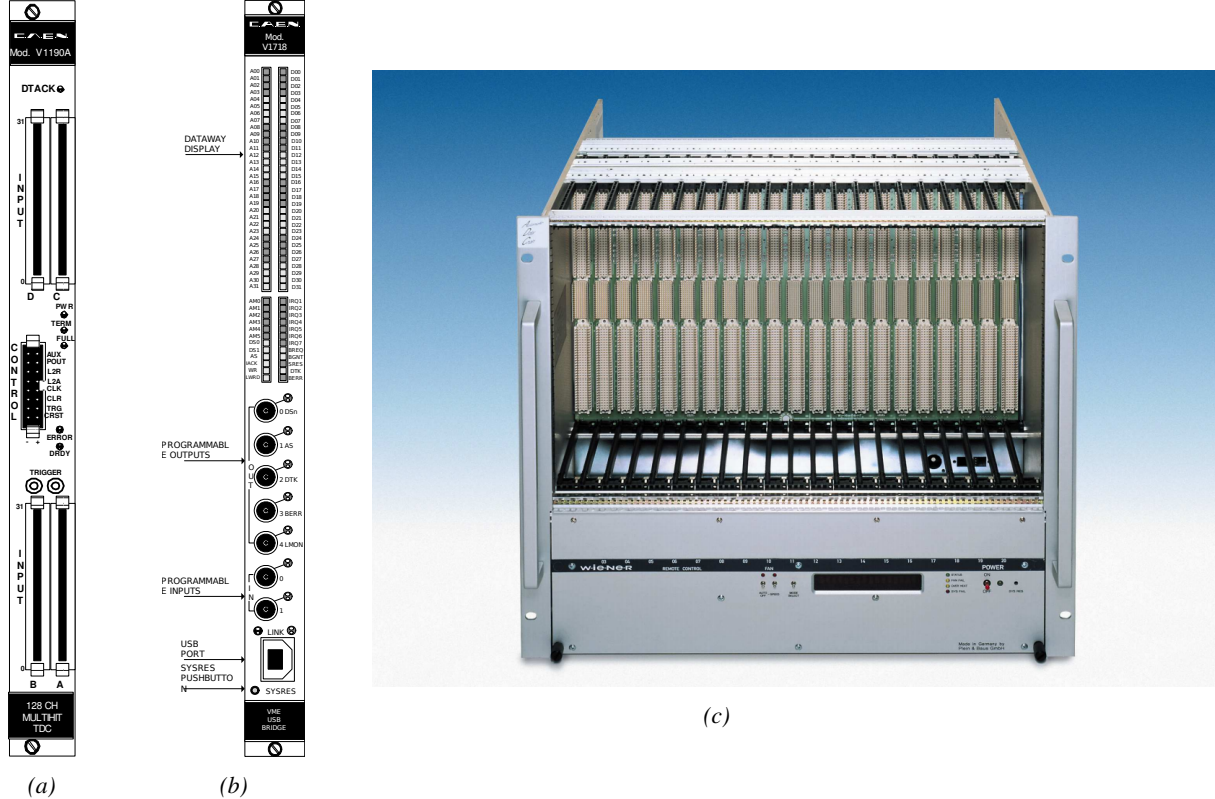
1044 where /path/to/the/log/file/in/the/output/data/folder is the only argument required. This  
 1045 log file is important for the webDCS as this file contains all the content of the communication of the  
 1046 webDCS and the different systems monitored by the webDCS. Its content is constantly displayed  
 1047 during data taking for the users to be able to follow the operations. The communication messages  
 1048 are normally sent to the webDCS log file via the functions declared in file MsgSvc.h, typically  
 1049 MSG\_INFO(string message).

1050

### 1051 A.3 Description of the readout setup

1052 The CMS RPC setup at GIF++ counts 5 V1190A Time-to-Digital Converter (TDC) manufactured  
 1053 by CAEN [29]. V1190A are VME units accepting 128 independent Multi-Hit/Multi-Event TDC  
 1054 channels whose signals are treated by 4 100 ps high performance TDC chips developed by CERN  
 1055 / ECP-MIC Division. The communication between the computer and the TDCs to transfer data is  
 1056 done via a V1718 VME master module also manufactured by CAEN and operated from a USB  
 1057 port [30]. These VME modules are all hosted into a 6U VME 6021 powered crate manufactured by  
 1058 W-Ie-Ne-R than can accommodate up to 21 VME bus cards [31]. These 3 components of the DAQ  
 1059 setup are shown in Figure A.1.

1060



1064 that comes as an input of the DAQ software.

1065

#### 1066 A.4.1 V1190A TDCs

1067 The DAQ used at GIF takes profit of the *Trigger Matching Mode* offered by V1190A modules.  
 1068 This setting is enabled through the method `v1190a::SetTrigMatching (int ntdcs)` where `ntdcs`  
 1069 is the total number of TDCs in the setup this setting needs to be enabled for (Source Code A.1). A  
 1070 trigger matching is performed in between a trigger time tag, a trigger signal sent into the TRIGGER  
 1071 input of the TDC visible on Figure A.1a, and the channel time measurements, signals recorded from  
 1072 the detectors under test in our case. Control over this data acquisition mode, explained through  
 1073 Figure A.2, is offered via 4 programmable parameters:

- 1074 • **match window:** the matching between a trigger and a hit is done within a programmable time  
 1075 window. This is set via the method

1076   `void v1190a::SetTrigWindowWidth(Uint windowHeight, int ntdcs)`

- 1077 • **window offset:** temporal distance between the trigger tag and the start of the trigger matching  
 1078 window. This is set via the method

1079   `void v1190a::SetTrigWindowWidth(Uint windowHeight, int ntdcs)`

- 1080 • **extra search margin:** an extended time window is used to ensure that all matching hits are  
 1081 found. This is set via the method

1082   `void v1190a::SetTrigSearchMargin(Uint searchMargin, int ntdcs)`

- 1083 • **reject margin:** older hits are automatically rejected to prevent buffer overflows and to speed  
 1084 up the search time. This is set via the method

1085   `void v1190a::SetTrigRejectionMargin(Uint rejectMargin, int ntdcs)`

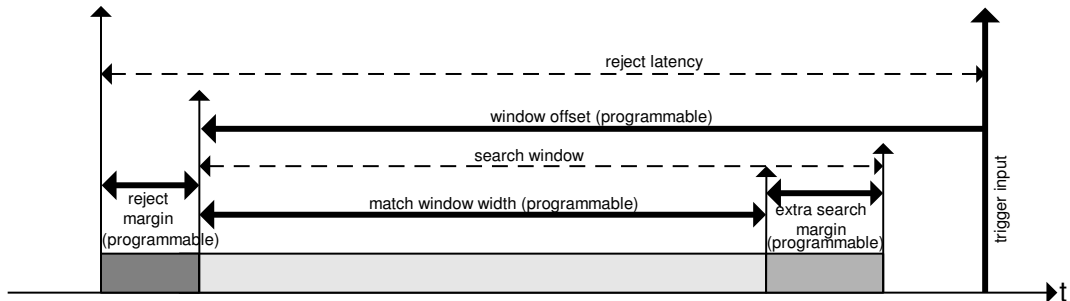


Figure A.2: Module V1190A Trigger Matching Mode timing diagram [29].

1086 Each of these 4 parameters are given in number of clocks, 1 clock being 25 ns long. It is easy to  
 1087 understand at this level that there are 3 possible functioning settings:

- 1088 • **1:** the match window is entirely contained after the trigger signal,

- 1089 • **2:** the match window overlaps the trigger signal, or

- 1090 • **3:** the match window is entirely contained before the trigger signal as displayed on Figure A.2.

1091 In both the first and second cases, the sum of the window width and of the offset can be set to  
1092 a maximum of 40 clocks, which corresponds to 1  $\mu$ s. Evidently, the offset can be negative, allowing  
1093 for a longer match window, with the constraint of having the window ending at most 1  $\mu$ s after the  
1094 trigger signal. In the third case, the maximum negative offset allowed is of 2048 clocks (12 bit) cor-  
1095 responding to 51.2  $\mu$ s, the match window being strictly smaller than the offset. In the case of GIF++,  
1096 the choice has been made to use this last setting by delaying the trigger signal. During the studies  
1097 performed in GIF++, both the efficiency of the RPCs, probed using a muon beam, and the noise or  
1098 gamma background rate are monitored. The extra search and reject margins are left unused.  
1099 To probe the efficiency of RPC detectors, the trigger time tag is provided by the coïncidence of  
1100 scintillators when a bunch of muons passes through GIF++ area is used to trigger the data acquisi-  
1101 tion. For this measurement, it is useful to reduce the match window width only to contain the muon  
1102 information. Indeed, the delay in between a trigger signal and the detection of the corresponding  
1103 muon in the RPC being very contant (typically a few tens of ns due to jitter and cable length), the  
1104 muon signals are very localised in time. Thus, due to a delay of approximalety 325 ns in between  
1105 the muons and the trigger, the settings where chosen to have a window width of 24 clocks (600 ns)  
1106 centered on the muon peak thanks to a negative offset of 29 clocks (725 ns).  
1107 On the otherhand, monitoring the rates don't require for the DAQ to look at a specific time window.  
1108 It is important to integrate enough time to have a robust measurement of the rate as the number of  
1109 hits per time unit. The triggerring signal is provided by a pulse generator at a frequency of 300 Hz  
1110 to ensure that the data taking occurs in a random way, with respect to beam physics, to probe only  
1111 the irradiation spectrum on the detectors. The match window is set to 400 clocks (10  $\mu$ s) and the  
1112 negative offset to 401 clocks as it needs to exceed the value of the match window.

```

1113 class v1190a
{
    private :
        long             Handle;
        vector<Data32>   Address;
        CVDataWidth      DataWidth;
        CVAddressModifier AddressModifier;

    public:

        v1190a(long handle, IniFile *inifile, int ntdcs);
        ~v1190a();
        Data16 write_op_reg(Data32 address, int code, string error);
        Data16 read_op_reg(Data32 address, string error);
        void Reset(int ntdcs);
        void Clear(int ntdcs);
        void TestWR(Data16 value,int ntdcs);
        void CheckTDCStatus(int ntdcs);
        void CheckCommunication(int ntdcs);
        void SetTDCTestMode(Data16 mode,int ntdcs);
        void SetTrigMatching(int ntdcs);
        void SetTrigTimeSubtraction(Data16 mode,int ntdcs);
        void SetTrigWindowWidth(Uint windowHeight,int ntdcs);
        void SetTrigWindowOffset(Uint windowOffset,int ntdcs);
        void SetTrigSearchMargin(Uint searchMargin,int ntdcs);
        void SetTrigRejectionMargin(Uint rejectMargin,int ntdcs);
        void GetTrigConfiguration(int ntdcs);
        void SetTrigConfiguration(IniFile *inifile,int ntdcs);
        void SetTDCDetectionMode(Data16 mode,int ntdcs);
        void SetTDCResolution(Data16 lsb,int ntdcs);
        void SetTDCDeadTime(Data16 time,int ntdcs);
        void SetTDCHeadTrailer(Data16 mode,int ntdcs);
        void SetTDCEventSize(Data16 size,int ntdcs);
        void SwitchChannels(IniFile *inifile,int ntdcs);
        void SetIRQ(Data32 level, Data32 count,int ntdcs);
        void SetBlockTransferMode(Data16 mode,int ntdcs);
        void Set(IniFile *inifile,int ntdcs);
        void CheckStatus(CVErrorCodes status) const;
        int ReadBlockD32(Uint tdc, const Data16 address,
                         Data32 *data, const Uint words, bool ignore_berr);
        Uint Read(RAWData *DataList,int ntdcs);
};

1114
1115

```

*Source Code A.1: Description of C++ object v1190a.*

1116     The v1190a object, defined in the DAQ software as in Source Code A.1, offers the possibility to  
 1117     concatenate all TDCs in the readout setup into a single object containing a list of hardware addresses  
 1118     (addresses to access the TDCs' buffer through the VME crate) and each constructor and method acts  
 1119     on the list of TDCs.  
 1120

#### 1121     A.4.2 DataReader

1122     Enabled thanks to v1190a::SetBlockTransferMode(Data16 mode, int ntdcs), the data transfer  
 1123     is done via Block Transfer (BLT). Using BLT allows to tranfer a fixed number of events called a  
 1124     *block*. This is used together with an Almost Full Level (AFL) of the TDCs' output buffers, defined

1125 through `v1190a::SetIRQ(Data32 level, Data32 count, int ntdcs)`. This AFL gives the maximum amount of 32735 words (16 bits, corresponding to the depth of a TDC output buffer) that can  
 1126 written in a buffer before an Interrupt Request (IRQ) is generated and seen by the VME Bridge,  
 1127 stopping the data acquisition to transfer the content of each TDC buffers before resuming. For each  
 1128 trigger, 6 words or more are written into the TDC buffer:

- 1130     • a **global header** providing information of the event number since the beginning of the data  
       acquisition,
- 1132     • a **TDC header**,
- 1133     • the **TDC data** (*if any*), 1 for each hit recorded during the event, providing the channel and the  
       time stamp associated to the hit,
- 1135     • a **TDC error** providing error flags,
- 1136     • a **TDC trailer**,
- 1137     • a **global trigger time tag** that provides the absolute trigger time relatively to the last reset,  
       and
- 1139     • a **global trailer** providing the total word count in the event.

1140     As previously described in Section 4.4.3, CMS RPC FEEs provide us with 100 ns long LVDS  
 1141 output signals that are injected into the TDCs' input. Any avalanche signal that gives a signal above  
 1142 the FEEs threshold is thus recorded by the TDCs as a hit within the match window. Each hit is  
 1143 assigned to a specific TDC channel with a time stamp, with a precision of 100 ps. The reference  
 1144 time,  $t_0 = 0$ , is provided by the beginning of the match window. Thus for each trigger, coming from  
 1145 a scintillator coïncidence or the pulse generator, a list of hits is stored into the TDCs' buffers and  
 1146 will then be transferred into a ROOT Tree.

1147     When the BLT is used, it is easy to understand that the maximum number of words that have  
 1148 been set as ALF will not be a finite number of events or, at least, the number of events that would  
 1149 be recorded into the TDC buffers will not be a multiple of the block size. In the last BLT cycle to  
 1150 transfer data, the number of events to transfer will most probably be lower than the block size. In that  
 1151 case, the TDC can add fillers at the end of the block but this option requires to send more data to the  
 1152 computer and is thus a little slower. Another solution is to finish the transfer after the last event by  
 1153 sending a bus error that states that the BLT reached the last event in the pile. This method has been  
 1154 chosen in GIF++.

1156     Due to irradiation, an event in GIF++ can count up to 300 words per TDC. A limit of 4096 words  
 1157 (12 bits) has been set to generate IRQ which represent from 14 to almost 700 events depending on  
 1158 the average of hits collected per event. Then the block size has been set to 100 events with enabled  
 1159 bus errors. When an AFL is reached for one of the TDCs, the VME bridge stops the acquisition by  
 1160 sending a BUSY signal.

1162

1163     The data is then transferred one TDC at a time into a structure called `RAWData` (Source Code A.2).

```
1164
1165 struct RAWData{
1166     vector<int>           *EventList;
1167     vector<int>           *NHitsList;
1168     vector<int>           *QFlagList;
1169     vector<vector<int>> > *Channellist;
1170     vector<vector<float>> > *TimeStampList;
1171 };
1172
```

1166                 *Source Code A.2: Description of data holding C++ structure `RAWData`.*

1167     In order to organize the data transfer and the data storage, an object called `DataReader` was  
1168     created (Source Code A.3). On one hand, it has `v1718` and `v1190a` objects as private members for  
1169     communication purposes, such as VME modules settings via the configuration file `*iniFile` or data  
1170     read-out through `v1190a::Read()` and on the other hand, it contains the structure `RAWData` that allows  
1171     to organise the data in vectors reproducing the tree structure of a ROOT file.

```
1172
1173 class DataReader
1174 {
1175     private:
1176     bool      StopFlag;
1177     IniFile *iniFile;
1178     Data32  MaxTriggers;
1179     v1718   *VME;
1180     int       nTDCs;
1181     v1190a  *TDCs;
1182     RAWData TDCData;
1183
1184     public:
1185     DataReader();
1186     virtual ~DataReader();
1187     void      SetIniFile(string inifilename);
1188     void      SetMaxTriggers();
1189     Data32  GetMaxTriggers();
1190     void      SetVME();
1191     void      SetTDC();
1192     int       GetQFlag(Uint it);
1193     void      Init(string inifilename);
1194     void      FlushBuffer();
1195     void      Update();
1196     string  GetFileName();
1197     void      WriteRunRegistry(string filename);
1198     void      Run();
1199 }
```

1174                 *Source Code A.3: Description of C++ object `DataReader`.*

1175     Each event is transferred from `TDCData` and saved into branches of a ROOT `TTree` as 3 integers  
1176     that represent the event ID (`EventCount`), the number of hits read from the TDCs (`nHits`), and the  
1177     quality flag that provides information for any problem in the data transfer (`qflag`), and 2 lists of  
1178     `nHits` elements containing the fired TDC channels (`TDCCh`) and their respective time stamps (`TDCTS`),  
1179     as presented in Source Code A.4. The ROOT file file is named using information contained into  
1180     the configuration file, presented in section A.5.2. The needed information is extracted using method  
1181     `DataReader::GetFileName()` and allow to build the output filename format `ScanXXXXXX_HVX_DAQ.root`

1182 where ScanXXXXXX is a 6 digit number representing the scan number into GIFT++ database and HVX  
 1183 the HV step within the scan that can be more than a single digit. An example of ROOT data file is  
 1184 provided with Figure A.3.

```
1185
RAWData TDCData;
TFile *outputFile = new TFile(outputFileName.c_str(),"recreate");
TTree *RAWDataTree = new TTree("RAWData","RAWData");

int EventCount = -9;
int nHits = -8;
int qflag = -7;
vector<int> TDCCh;
vector<float> TDCTS;

RAWDataTree->Branch("EventNumber",&EventCount, "EventNumber/I");
RAWDataTree->Branch("number_of_hits",&nHits,"number_of_hits/I");
RAWDataTree->Branch("Quality_flag",&qflag,"Quality_flag/I");
RAWDataTree->Branch("TDC_channel",&TDCCh);
RAWDataTree->Branch("TDC_TimeStamp",&TDCTS);

1186
//...
//Here read the TDC data using v1190a::Read() and place it into
//TDCData for as long as you didn't collect the requested amount
//of data.
//...

for(Uint i=0; i<TDCData.EventList->size(); i++){
    EventCount = TDCData.EventList->at(i);
    nHits = TDCData.NHitsList->at(i);
    qflag = TDCData.QFlagList->at(i);
    TDCCh = TDCData.ChannelList->at(i);
    TDCTS = TDCData.TimeStampList->at(i);
    RAWDataTree->Fill();
}
```

1187 *Source Code A.4: Highlight of the data transfer and organisation within DataReader::Run() after the data has been collected into TDCData.*

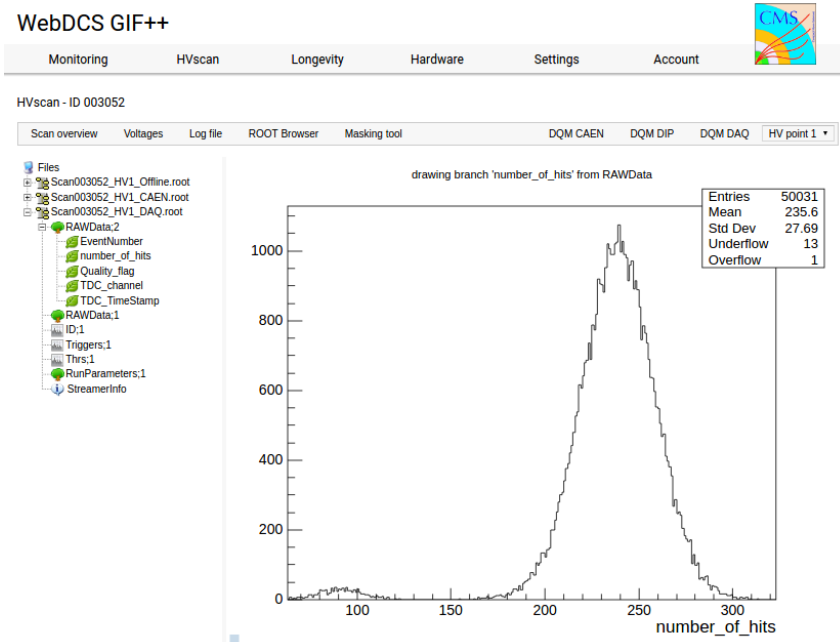


*Figure A.3: Structure of the ROOT output file generated by the DAQ. The 5 branches (EventNumber, number\_of\_hits, Quality\_flag, TDC\_channel and TDC\_TimeStamp) are visible on the left panel of the ROOT browser. On the right panel is visible the histogram corresponding to the variable nHits. In this specific example, there were approximately 50k events recorded to measure the gamma irradiation rate on the detectors. Each event is stored as a single entry in the TTree.*

#### 1188    A.4.3 Data quality flag

1189    Among the parameters that are recorded for each event, the quality flag, defined in Source Code A.5,  
 1190    is determined on the fly by checking the data recorded by every single TDC. From method v1190a::Read(),  
 1191    it can be understood that the content of each TDC buffer is readout one TDC at a time. Entries are  
 1192    created in the data list for the first TDC and then, when the second buffer is readout, events corre-  
 1193    sponding to entries that have already been created to store data for the previous TDC are added to  
 1194    the existing list element. On the contrary, when an event entry has not been yet created in the data  
 1195    list, a new entry is created.

```
1196
typedef enum _QualityFlag {
 1197   GOOD      = 1,
  CORRUPTED = 0
} QualityFlag;
```

1198    *Source Code A.5: Definition of the quality flag enum.*

1199    It is possible that each TDC buffer contains a different number of events. In cases where the first  
 1200    element in the buffer list is an event for corresponds to a new entry, the difference in between the  
 1201    entry from the buffer and the last entry in the data list is recorded and checked. If it is greater than 1,  
 1202    what should never be the case, the quality flag is set to CORRUPTED for this TDC and an empty entry  
 1203    is created in the place of the missing ones. Missing entries are believe to be the result of a bad hold

1204 on the TDC buffers at the moment of the readout. Indeed, the software hold is effective only on 1  
 1205 TDC at a time and no solution as been found yet to completely block the writting in the buffers when  
 1206 an IRQ is received.

1207 At the end of each BLT cycle, the ID of the last entry stored for each TDC buffer is not recorded.  
 1208 When starting the next cycle, if the first entry in the pile corresponds to an event already existing  
 1209 in the list, the readout will start from this list element and will not be able to check the difference  
 1210 in between this entry's ID and the one of the last entry that was recorded for this TDC buffer in  
 1211 the previous cycle. In the case events were missing, the flag stays at its initial value of 0, which is  
 1212 similar to CORRUPTED and it is assumed that then this TDC will not contribute to `number_of_hits`,  
 1213 `TDC_channel` or `TDC_TimeStamp`.

1214 Finally, since there will be 1 `RAWData` entry per TDC for each event (meaning `nTDCs` entries,  
 1215 referring to `DataReader` private attribute), the individual flags of each TDC will be added together.  
 1216 The final format is an integer composed `nTDCs` digits where each digit is the flag of a specific TDC.  
 1217 This is constructed using powers of 10 like follows:

```
1218     TDC 0: QFlag = 100 × _QualityFlag
1219     TDC 1: QFlag = 101 × _QualityFlag
1220     ...
1221     TDC N: QFlag = 10N × _QualityFlag
```

1222 and the final flag to be with N digits:

```
1223     QFlag = n....3210
```

1224 each digit being 1 or 0. Below is given an example with a 4 TDCs setup.

1225 If all TDCs were good : `QFlag = 1111`,

1226 but if TDC 2 was corrupted : `QFlag = 1011`.

1227 When data taking is over and the data contained in the dynamical `RAWData` structure is transferred  
 1228 to the ROOT file, all the 0s are changed into 2s by calling the method `DataReader::GetQFlag()`.  
 1229 This will help translating the flag without knowing the number of TDCs beforehand. Indeed, a flag  
 1230 111 could be due to a 3 TDC setup with 3 good individual TDC flags or to a more than 3 TDC setup  
 1231 with TDCs those ID is greater than 2 being CORRUPTED, thus giving a 0.

1232 The quality flag has been introduced quite late, in October 2017 only, to the list of GIFT++ DAQ  
 1233 parameters to be recorded into the output ROOT file. Before this addition, the missing data, corrupting  
 1234 the quality for the offline analysis, was contributing to artificially fill data with lower multiplicity.  
 1235 Looking at `TBranch number_of_hits` provides an information about the data of the full GIFT++  
 1236 setup. When a TDC is not able to transfer data for a specific event, the effect is a reduction of the  
 1237 total number of hits recorded in the full setup, this is what can be seen from Figure A.4. After offline  
 1238 reconstruction detector by detector, the effect of missing events can be seen in the artificially filled  
 1239 bin at multiplicity 0 shown in Figure A.5. Nonetheless, for data with high irradiation levels, as it is  
 1240 the case for Figure A.5a, discarding the fake multiplicity 0 data can be done easily during the offline  
 1241 analysis. At lower radiation, the missing events contribution becomes more problematic as the mul-  
 1242 tiplicity distribution overlaps the multiplicity 0 and that in the same time the proportion of missing

events decreases. Attempts to fit the distribution with a Poisson or skew distribution function were not conclusive and this very problem has been at the origin of the quality flag that allows to give a non ambiguous information about each event quality.

1246

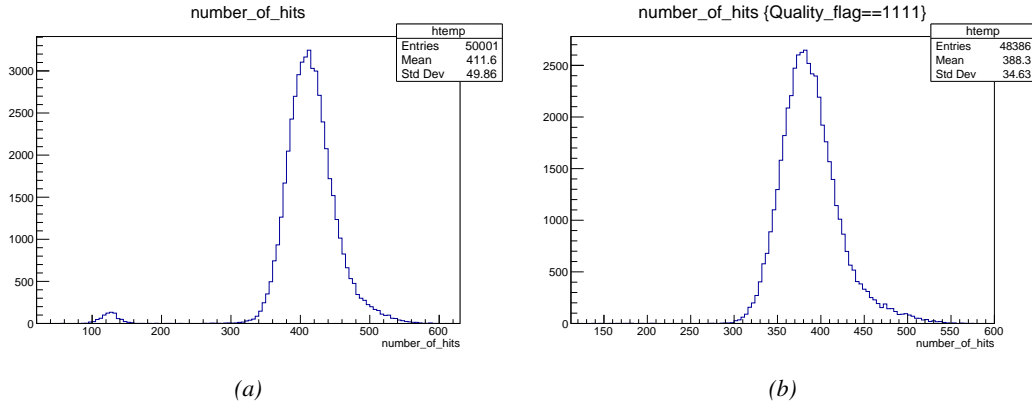


**Figure A.4:** The effect of the quality flag is explained by presenting the content of `TBranch number_of_hits` of a data file without `Quality_flag` in Figure A.4a and the content of the same `TBranch` for data corresponding to a `Quality_flag` where all TDCs were labelled as `GOOD` in Figure A.4b taken with similar conditions. It can be noted that the number of entries in Figure A.4b is slightly lower than in Figure A.4a due to the excluded events.

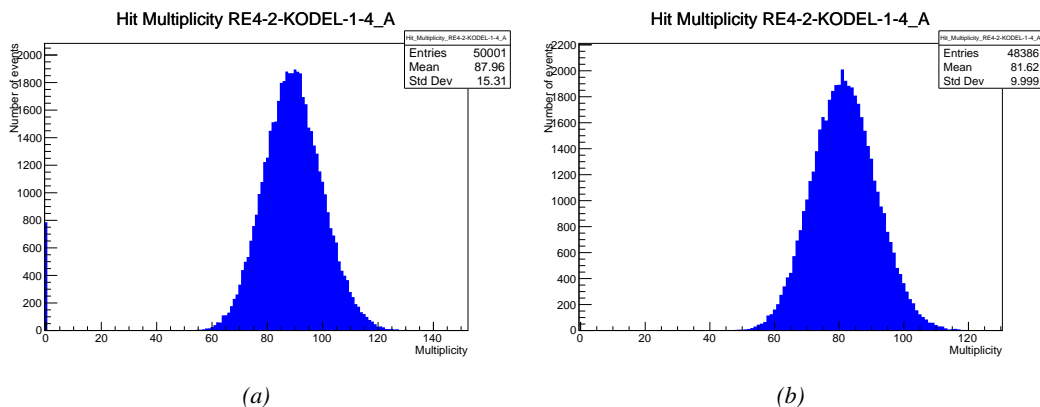


**Figure A.5:** Using the same data as previously showed in Figure A.4, the effect of the quality flag is explained by presenting the reconstructed hit multiplicity of a data file without `Quality_flag` in Figure A.5a and the reconstructed content of the same RPC partition for data corresponding to a `Quality_flag` where all TDCs were labelled as `GOOD` in Figure A.5b taken with similar conditions. The artificial high content of bin 0 is completely suppressed.

## A.5 Communications

To ensure data readout and dialog in between the machine and the TDCs or in between the webDCS and the DAQ, different communication solutions were used. First of all, it is important to have a

1250 module to allow the communication in between the TDCs and the computer from which the DAQ  
 1251 operates. When this communication is effective, shifters using the webDCS to control data taking  
 1252 can thus send instructions to the DAQ.

1253

### 1254 A.5.1 V1718 USB Bridge

1255 In the previous section, the data transfer has been discussed. The importance of the `v1718` object  
 1256 (Source Code A.6), used as private member of `DataReader`, was not explicated. VME master  
 1257 modules are used for communication purposes as they host the USB port that connects the pow-  
 1258 ered crate buffer to the computer where the DAQ is installed. From the source code point of view,  
 1259 this object is used to control the communication status, by reading the returned error codes with  
 1260 `v1718::CheckStatus()`, or to check for IRQs coming from the TDCs through `v1718::CheckIRQ()`.  
 1261 Finally, to ensure that triggers are blocked at the hardware level, a NIM pulse is sent out of one of the  
 1262 5 programmable outputs (`v1718::SendBUSY()`) to the VETO of the coincidence module where the  
 1263 trigger signals originate from. As long as this signal is ON, no trigger can reach the TDCs anymore.

1264

```
class v1718{
    private:
        int Handle;
        Data32 Data;           // Data
        CVIRQLevels Level;    // Interrupt level
        CVAddressModifier AM;  // Addressing Mode
        CVDataWidth dataSize; // Data Format
        Data32 BaseAddress;   // Base Address

    public:
        v1718(IniFile *inifile);
        ~v1718();
        long GetHandle(void) const;
        int SetData(Data16 data);
        Data16 GetData(void);
        int SetLevel(CVIRQLevels level);
        CVIRQLevels GetLevel(void);
        int SetAM(CVAddressModifier am);
        CVAddressModifier GetAM(void);
        int SetDatasize(CVDataWidth datasize);
        CVDataWidth GetDataSize(void);
        int SetBaseAddress(Data16 baseaddress);
        Data16 GetBaseAddress(void);
        void CheckStatus(CVErrorCodes status) const;
        void CheckIRQ();
        void SetPulsers();
        void SendBUSY(BusyLevel level);
};
```

1265

*Source Code A.6: Description of C++ object v1718.*

### 1267 A.5.2 Configuration file

1268 The DAQ software takes as input a configuration file written using INI standard [32]. This file is  
 1269 partly filled with the information provided by the shifters when starting data acquisition using the  
 1270 webDCS, as shown by Figure A.6. This information is written in section [`General`] and will later

1271 be stored in the ROOT file that contains the DAQ data as can be seen from Figure A.3. Indeed,  
 1272 another `TTree` called `RunParameters` as well as the 2 histograms `ID`, containing the scan number,  
 1273 start and stop time stamps, and `Triggers`, containing the number of triggers requested by the shifter,  
 1274 are available in the data files. Moreover, `ScanID` and `HV` are then used to construct the file name  
 1275 thanks to the method `DataReader::GetFileName()`.

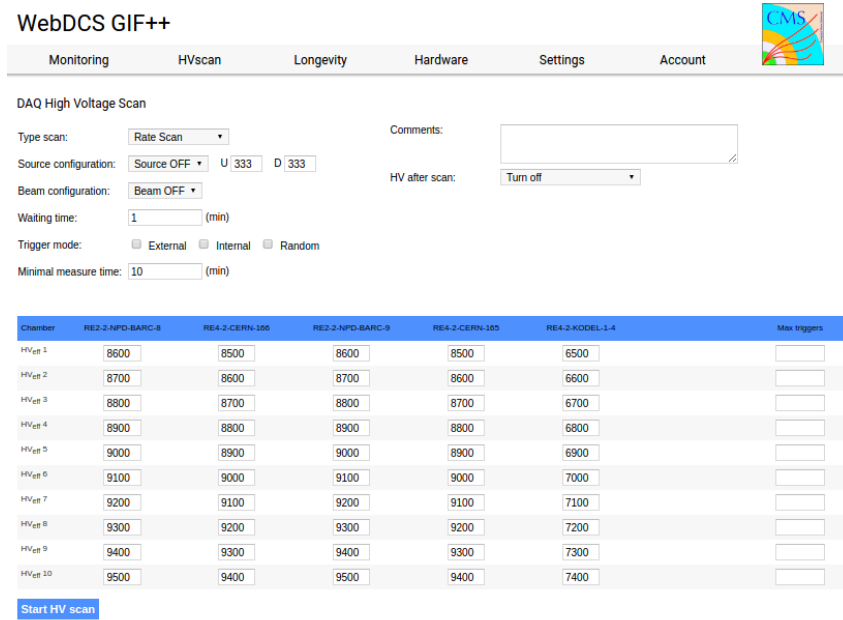


Figure A.6: WebDCS DAQ scan page. On this page, shifters need to choose the type of scan (Rate, Efficiency or Noise Reference scan), the gamma source configuration at the moment of data taking, the beam configuration, and the trigger mode. These information will be stored in the DAQ ROOT output. Are also given the minimal measurement time and waiting time after ramping up of the detectors is over before starting the data acquisition. Then, the list of HV points to scan and the number of triggers for each run of the scan are given in the table underneath.

1276 The rest of the information is written beforehand in the configuration file template, as explicated  
 1277 in Source Code A.7, and contains the hardware addresses to the different VME modules in the  
 1278 setup as well as settings for the TDCs. As the TDC settings available in the configuration file are not  
 1279 supposed to be modified, an improvement would be to remove them from the configuration file and  
 1280 to hardcode them inside of the DAQ code itself or to place them into a different INI file that would  
 1281 host only the TDC settings to lower the probability for a bad manipulation of the configuration file  
 1282 that can be modified from one of webDCS' menus.

1283

```

[General]
TdcS=4
ScanID=$scanid
HV=$HV
RunType=$runtype
MaxTriggers=$maxtriggers
Beam=$beam
[VMEInterface]
Type=V1718
BaseAddress=0xFF0000
Name=VmeInterface
[TDC0]
Type=V1190A
BaseAddress=0x00000000
Name=Tdc0
StatusA00-15=1
StatusA16-31=1
StatusB00-15=1
StatusB16-31=1
StatusC00-15=1
StatusC16-31=1
StatusD00-15=1
StatusD16-31=1
[TDC1]
Type=V1190A
BaseAddress=0x11110000
Name=Tdc1
StatusA00-15=1
StatusA16-31=1
StatusB00-15=1
StatusB16-31=1
StatusC00-15=1
StatusC16-31=1
StatusD00-15=1
StatusD16-31=1
[TDC2]
Type=V1190A
BaseAddress=0x22220000
Name=Tdc2
StatusA00-15=1
StatusA16-31=1
StatusB00-15=1
StatusB16-31=1
StatusC00-15=1
StatusC16-31=1
StatusD00-15=1
StatusD16-31=1
[TDC3]
Type=V1190A
BaseAddress=0x44440000
Name=Tdc3
StatusA00-15=1
StatusA16-31=1
StatusB00-15=1
StatusB16-31=1
StatusC00-15=1
StatusC16-31=1
StatusD00-15=1
StatusD16-31=1
[TDCSettings]
TriggerExtraSearchMargin=0
TriggerRejectMargin=0
TriggerTimeSubtraction=0b1
TdcDetectionMode=0b01
TdcResolution=0b10
TdcDeadTime=0b00
TdcHeadTrailer=0b1
TdcEventSize=0b1001
TdcTestMode=0b0
BLTMode=1

```

1284

*Source Code A.7: INI configuration file template for 4 TDCs. In section [General], the number of TDCs is explicitated and information about the ongoing run is given. Then, there are sections for each and every VME modules. There buffer addresses are given and for the TDCs, the list of channels to enable is given. Finally, in section [TDCSettings], a part of the TDC settings are given.*

1286     In order to retrieve the information of the configuration file, the object `IniFile` has been developed  
 1287     to provide an INI parser, presented in Source Code A.8. It contains private methods returning a  
 1288     boolean to check the type of line written in the file, whether a comment, a group header or a key line  
 1289     (`IniFile::CheckIfComment()`, `IniFile::CheckIfGroup()` and `IniFile::CheckIfToken()`). The  
 1290     key may sometimes be referred to as *token* in the source code. Moreover, the private element  
 1291     `FileData` is a map of `const string` to `string` that allows to store the data contained inside the  
 1292     configuration file via the public method `IniFile::GetFileData()` following the formatting (see  
 1293     method `IniFile::Read()`):

```
1294
1295     string group, token, value;
    // Get the field values for the 3 strings.
    // Then concatenate group and token together as a single string
    // with a dot separation.
    token = group + "." + token;
    FileData[token] = value;
```

1296     More methods have been written to translate the different keys into the right variable format  
 1297     when used by the DAQ. For example, to get a `float` value out of the configuration file data, knowing  
 1298     the group and the key needed, the method `IniFile::floatType()` can be used. It takes 3 arguments  
 1299     being the group name and key name (both `string`), and a default `float` value used as exception in  
 1300     the case the expected combination of group and key cannot be found in the configuration file. This  
 1301     default value is then used and the DAQ continues on working after sending an alert in the log file for  
 1302     further debugging.

```

1303 typedef map< const string, string > IniFileData;
1304
class IniFile{
    private:
        bool          CheckIfComment (string line);
        bool          CheckIfGroup(string line, string& group);
        bool          CheckIfToken(string line, string& key, string& value);
        string         FileName;
        IniFileData   FileData;
        int           Error;

    public:
        IniFile();
        IniFile(string filename);
        virtual      ~IniFile();

        // Basic file operations
        void          SetFileName(string filename);
        int           Read();
        int           Write();
        IniFileData GetFileData();

        // Data readout methods
        Data32         addressType (string groupname, string keyname, Data32
→     defaultvalue);
        long          intType     (string groupname, string keyname, long
→     defaultvalue);
        long long    longType    (string groupname, string keyname, long long
→     defaultvalue );
        string         stringType  (string groupname, string keyname, string
→     defaultvalue );
        float         floatType   (string groupname, string keyname, float
→     defaultvalue );

        // Error methods
        string         GetErrorMsg();
    };

```

1305       *Source Code A.8: Description of C++ object `IniFile` used as a parser for INI file format.*

### 1306     A.5.3 WebDCS/DAQ intercommunication

1307     When shifters send instructions to the DAQ via the configuration file, it is the webDCS itself that  
 1308     gives the start command to the DAQ and then the 2 softwares use inter-process communication  
 1309     through file to synchronise themselves. This communication file is represented by the variable **const**  
 1310     string \_\_runstatuspath.

1311     On one side, the webDCS sends commands or status that are readout by the DAQ:

- 1312       • INIT, status sent when launching a scan and read via function `CtrlRunStatus(...)`,
- 1313       • START, command to start data taking and read via function `CheckSTART()`,
- 1314       • STOP, command to stop data taking at the end of the scan and read via function `CheckSTOP()`,  
 1315        and
- 1316       • KILL, command to kill data taking sent by user and read via function `CheckKILL()`

1317 and on the other, the DAQ sends status that are controled by the webDCS:

- 1318     ● `DAQ_RDY`, sent with `SendDAQReady()` to signify that the DAQ is ready to receive commands  
1319       from the webDCS,
- 1320     ● `RUNNING`, sent with `SendDAQRunning()` to signify that the DAQ is taking data,
- 1321     ● `DAQ_ERR`, sent with `SendDAQError()` to signify that the DAQ didn't receive the expected com-  
1322       mand from the webDCS or that the launch command didn't have the right number of argu-  
1323       ments,
- 1324     ● `RD_ERR`, sent when the DAQ wasn't able to read the communication file, and
- 1325     ● `WR_ERR`, sent when the DAQ wasn't able to write into the communication file.

#### 1326     **A.5.4 Example of inter-process communication cycle**

1327 Under normal conditions, the webDCS and the DAQ processes exchange commands and status via  
1328 the file hosted at the address `__runstatuspath`, as explained in subsection A.5.3. An example of  
1329 cycle is given in Table A.1. In this example, the steps 3 to 5 are repeated as long as the webDCS tells  
1330 the DAQ to take data. A data taking cycle is the equivalent as what is called a *Scan* in GIFT++ jargon,  
1331 referring to a set a runs with several HV steps. Each repetition of steps 3 to 5 is then equivalent to a  
1332 single *Run*.

1333

1334 At any moment during the data taking, for any reason, the shifter can decide that the data taking  
1335 needs to be stopped before it reached the end of the scheduled cycle. Thus at any moment on the  
1336 cycle, the content of the inter-process communication file will be changed to `KILL` and the DAQ will  
1337 shut down right away. The DAQ checks for `KILL` signals every 5s after the TDCs configuration is  
1338 over. So far, the function `CheckKILL()` has been used only inside of the data taking loop of method  
1339 `DataReader::Run()` and thus, if the shifter decides to KILL the data taking during the TDC con-  
1340 figuration phase or the HV ramping in between 2 HV steps, the DAQ will not be stopped smoothly  
1341 and a *force kill* command will be sent to stop the DAQ process that is still awake on the computer.  
1342 Improvements can be brought on this part of the software to make sure that the DAQ can safely  
1343 shutdown at any moment.

1344

#### 1345     **A.6 Software export**

1346 In section A.2 was discussed the fact that the DAQ as written in its last version is not a standalone  
1347 software. It is possible to make it a standalone program that could be adapted to any VME setup  
1348 using V1190A and V1718 modules by creating a GUI for the software or by printing the log mes-  
1349 sages that are normally printed in the webDCS through the log file, directly into the terminal. This  
1350 method was used by the DAQ up to version 3.0 moment where the webDCS was completed. Also, it  
1351 is possible to check branches of DAQ v2.X to have example of communication through a terminal.

1352

1353     DAQ v2.X is nonetheless limited in it's possibilities and requires a lot of offline manual interven-  
1354     tions from the users. Indeed, there is no communication of the software with the detectors' power  
1355     supply system that would allow for a user a predefine a list of voltages to operate the detectors at

step	actions of webDCS	status of DAQ	<code>__runstatuspath</code>
1	launch DAQ ramp voltages ramping over wait for currents stabilization	readout of IniFile configuration of TDCs	INIT
2		configuration done send DAQ ready wait for START signal	DAQ_RDY
3	waiting time over send START		START
4	wait for run to end monitor DAQ run status	data taking ongoing check for KILL signal	RUNNING
5		run over send DAQ_RDY wait for next DCS signal	DAQ_RDY
6	ramp voltages ramping over wait for currents stabilization		DAQ_RDY
3	waiting time over send START		START
4	wait for run to end monitor DAQ run status	update IniFile information data taking ongoing check for KILL signal	RUNNING
5		run over send DAQ_RDY wait for next DCS signal	DAQ_RDY
7	send command STOP	DAQ shuts down	STOP

Table A.1: Inter-process communication cycles in between the webDCS and the DAQ through file string signals.

1356 and loop over to take data without any further manual intervention. In v2.X, the data is taken for a  
1357 single detector setting and at the end of each run, the softwares asks the user if he intends on taking  
1358 more runs. If so, the software invites the user to set the operating voltages accordingly to what is  
1359 necessary and to manual update the configuration file in consequence. This working mode can be a  
1360 very first approach before an evolution and has been successfully used by colleagues from different  
1361 collaborations.

1362  
1363 For a more robust operation, it is recommended to develop a GUI or a web application to inter-  
1364 face the DAQ. Moreover, to limit the amount of manual interventions, and thus the probability to  
1365 make mistakes, it is also recommended to add an extra feature into the DAQ by installing the HV  
1366 Wrapper library provided by CAEN of which an example of use in a similar DAQ software devel-  
1367 opped by a master student of UGent, and called TinyDAQ, is provided on UGent's github. Then, this  
1368 HV Wrapper will help you communicating with and give instructions to a CAEN HV powered crate  
1369 and can be added into the DAQ at the same level where the communication with the user was made  
1370 in DAQ v2.X. In case you are using another kind of power system for your detectors, it is stringly  
1371 adviced to use HV modules or crates that can be remotely controled via a using C++ libraries.  
1372

# B

1373

1374

## Details on the offline analysis package

1375 The data collected in GIF++ thanks to the DAQ described in Appendix A is difficult to interpret by  
1376 a human user that doesn't have a clear idea of the raw data architecture of the ROOT data files. In  
1377 order to render the data human readable, a C++ offline analysis tool was designed to provide users  
1378 with detector by detector histograms that give a clear overview of the parameters monitored during  
1379 the data acquisition [33]. In this appendix, details about this software in the context of GIF++, as of  
1380 how the software was written and how it functions will be given.

### 1381 B.1 GIF++ Offline Analysis file tree

1382 GIF++ Offline Analysis source code is fully available on github at [https://github.com/aafagot/GIF\\_OfflineAnalysis](https://github.com/aafagot/GIF_OfflineAnalysis). The software requires ROOT as non-optionnal dependency  
1383 as it takes ROOT files in input and write an output ROOT file containing histograms. To compile the  
1384 GIF++ Offline Analysis project is compiled with cmake. To compile, first a build/ directory must  
1385 be created to compile from there:

```
1387 mkdir build
1388 cd build
1389 cmake ..
1390 make
1391 make install
```

1389 To clean the directory and create a new build directory, the bash script cleandir.sh can be used:

```
1390
1391 ./cleandir.sh
```

1392 The source code tree is provided below along with comments to give an overview of the files' con-  
1393 tent. The different objects created for this project (`Infrastructure`, `Trolley`, `RPC`, `Mapping`, `RPCHit`,  
1394 `RPCCluster` and `Inifile`) will be described in details in the following sections.

1395

```

GIF_OfflineAnalysis
├── bin
│   └── offlineanalysis ..... EXECUTABLE
├── build..... CMAKE COMPILATION DIRECTORY
└── ...
    ├── include..... LIST OF C++ HEADER FILES
    │   ├── Cluster.h..... DECLARATION OF OBJECT RPCCLUSTER
    │   ├── Current.h..... DECLARATION OF GETCURRENT ANALYSIS MACRO
    │   ├── GIFTrolley.h..... DECLARATION OF OBJECT TROLLEY
    │   ├── Infrastructure.h..... DECLARATION OF OBJECT INFRASTRUCTURE
    │   ├── IniFile.h..... DECLARATION OF OBJECT INI FILE FORINI PARSER
    │   ├── Mapping.h..... DECLARATION OF OBJECT MAPPING
    │   ├── MsgSvc.h..... DECLARATION OF OFFLINE LOG MESSAGES
    │   ├── OfflineAnalysis.h..... DECLARATION OF DATA ANALYSIS MACRO
    │   ├── RPCTracker.h..... DECLARATION OF OBJECT RPC
    │   ├── RPCHit.h..... DECLARATION OF OBJECT RPCHIT
    │   ├── types.h..... DEFINITION OF USEFUL VARIABLE TYPES
    │   └── utils.h..... DECLARATION OF USEFUL FUNCTIONS
    ├── obj..... BINARY FILES CREATED BY COMPILER
    └── ...
        ├── src..... LIST OF C++ SOURCE FILES
        │   ├── Cluster.cc..... DEFINITION OF OBJECT RPCCLUSTER
        │   ├── Current.cc .....

```

## 1396 B.2 Usage of the Offline Analysis

1397 In order to use the Offline Analysis tool, it is necessary to know the Scan number and the HV Step  
 1398 of the run that needs to be analysed. This information needs to be written in the following format:

1399

1400 Scan00XXXX\_HVY

1401 where XXXX is the scan ID and y is the high voltage step (in case of a high voltage scan, data will be  
 1402 taken for several HV steps). This format corresponds to the base name of data files in the database

1403 of the GIF++ webDCS. Usually, the offline analysis tool is automatically called by the webDCS at  
 1404 the end of data taking or by a user from the webDCS panel if an update of the tool was brought.  
 1405 Nonetheless, an expert can locally launch the analysis for tests on the GIF++ computer, or a user can  
 1406 get the code on its local machine from github and download data from the webDCS for its own anal-  
 1407 ysis. To launch the code, the following command can be used from the `GIF_OfflineAnalysis` folder:

1408  
 1409     `bin/offlineanalysis /path/to/Scan00XXXX_HVY`

1410 where, `/path/to/Scan00XXXX_HVY` refers to the local data files. Then, the offline tool will by itself  
 1411 take care of finding all available ROOT data files present in the folder, as listed below:

- 1412     ● `Scan00XXXX_HVY_DAQ.root` containing the TDC data as described in Appendix ?? (events, hit  
 1413         and timestamp lists), and
- 1414     ● `Scan00XXXX_HVY_CAEN.root` containing the CAEN mainframe data recorded by the monitor-  
 1415         ing tool webDCS during data taking (HVs and currents of every HV channels). This file is  
 1416         created independently of the DAQ.

## 1417     **B.2.1 Output of the offline tool**

### 1418     **B.2.1.1 ROOT file**

1419 The analysis gives in output ROOT datafiles that are saved into the data folder and called using the  
 1420 naming convention `Scan00XXXX_HVY_Offline.root`. Inside those, a list of `TH1` histograms can be  
 1421 found. Its size will vary as a function of the number of detectors in the setup as each set of histograms  
 1422 is produced detector by detector. For each partition of each chamber, can be found:

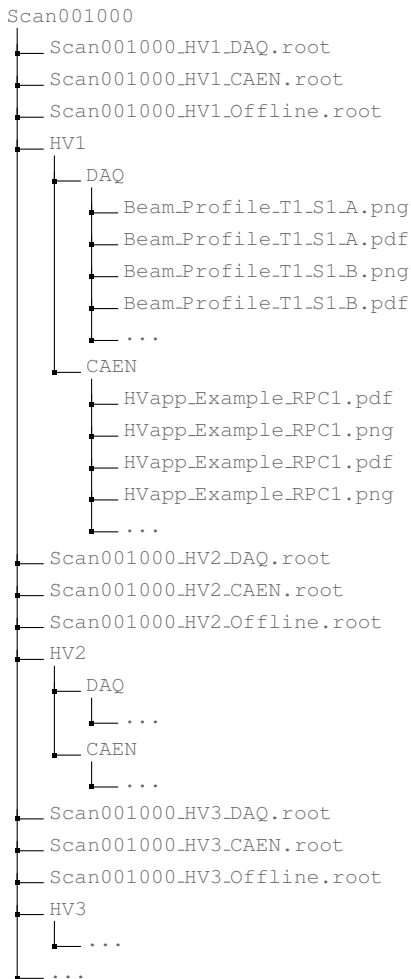
- 1423     ● `Time_Profile_Tt_Sc_p` shows the time profile of all recorded events (number of events per  
 1424         time bin),
- 1425     ● `Hit_Profile_Tt_Sc_p` shows the hit profile of all recorded events (number of events per chan-  
 1426         nel),
- 1427     ● `Hit_Multiplicity_Tt_Sc_p` shows the hit multiplicity (number of hits per event) of all recorded  
 1428         events (number of occurrences per multiplicity bin),
- 1429     ● `Strip_Mean_Noise_Tt_Sc_p` shows noise/gamma rate per unit area for each strip in a se-  
 1430         lected time range. After filters are applied on `Time_Profile_Tt_Sc_p`, the filtered version  
 1431         of `Hit_Profile_Tt_Sc_p` is normalised to the total integrated time and active detection area  
 1432         of a single channel,
- 1433     ● `Strip_Activity_Tt_Sc_p` shows noise/gamma activity for each strip (normalised version of  
 1434         previous histogram - strip activity = strip rate / average partition rate),
- 1435     ● `Strip_Homogeneity_Tt_Sc_p` shows the *homogeneity* of a given partition ( $\text{homogeneity} = \exp(-\text{strip rates standard deviation(strip rates in partition/average partition rate)})$ ),
- 1436     ● `mask_Strip_Mean_Noise_Tt_Sc_p` shows noise/gamma rate per unit area for each masked  
 1437         strip in a selected time range. Offline, the user can control the noise/gamma rate and decide to  
 1438         mask the strips that are judged to be noisy or dead. This is done via the *Masking Tool* provided  
 1439         by the webDCS,

- 1441     ● `mask_Strip_Activity_Tt_Sc_p` shows noise/gamma activity per unit area for each masked  
1442       strip with respect to the average rate of active strips,
- 1443     ● `NoiseCSize_H_Tt_Sc_p` shows noise/gamma cluster size, a cluster being constructed out of  
1444       adjacent strips giving a signal at the *same time* (hits within a time window of 25 ns),
- 1445     ● `NoiseCMult_H_Tt_Sc_p` shows noise/gamma cluster multiplicity (number of reconstructed  
1446       clusters per event),
- 1447     ● `Chip_Mean_Noise_Tt_Sc_p` shows the same information than `Strip_Mean_Noise_Tt_Scp` us-  
1448       ing a different binning (1 chip corresponds to 8 strips),
- 1449     ● `Chip_Activity_Tt_Sc_p` shows the same information than `Strip_Activity_Tt_Scp` using  
1450       chip binning,
- 1451     ● `Chip_Homogeneity_Tt_Sc_p` shows the homogeneity of a given partition using chip binning,
- 1452     ● `Beam_Profile_Tt_Sc_p` shows the estimated beam profile when taking efficiency scan. This  
1453       is obtained by filtering `Time_Profile_Tt_Sc_p` to only consider the muon peak where the  
1454       noise/gamma background has been subtracted. The resulting hit profile corresponds to the  
1455       beam profile on the detector channels,
- 1456     ● `L0_Efficiency_Tt_Sc_p` shows the level 0 efficiency that was estimated **without** muon track-  
1457       ing,
- 1458     ● `MuonCSize_H_Tt_Sc_p` shows the level 0 muon cluster size that was estimated **without** muon  
1459       tracking, and
- 1460     ● `MuonCMult_H_Tt_Sc_p` shows the level 0 muon cluster multiplicity that was estimated **without**  
1461       muon tracking.

1462     In the histogram labels, *t* stands for the trolley number (1 or 3), *c* for the chamber slot label in  
1463     trolley *t* and *p* for the partition label (A, B, C or D depending on the chamber layout) as explained  
1464     in Chapter 5.3.

1465     In the context of GIF++, an extra script called by the webDCS is called to extract the histograms  
1466     from the ROOT files. The histograms are then stored in PNG and PDF formats into the correspond-  
1467     ing folder (a single folder per HV step, so per ROOT file). the goal is to then display the histograms  
1468     on the Data Quality Monitoring (DQM) page of the webDCS in order for the users to control the  
1469     quality of the data taking at the end of data taking. An example of histogram organisation is given  
1470     below:

1471  
1472



1473     *Here can put some screens from the webDCS to show the DQM and the plots available to users.*  
 1474

1475     **B.2.1.2 CSV files**

1476     Moreover, up to 3 CSV files can be created depending on which ones of the 3 input files were in the  
 1477     data folder:

- 1478       ● `Offline-Corrupted.csv` , is used to keep track of the amount of data that was corrupted and  
 1479       removed from old data format files that don't contain any data quality flag.
- 1480       ● `Offline-Current.csv` , contains the summary of the currents and voltages applied on each  
 1481       RPC HV channel.
- 1482       ● `Offline-L0-EffC1.csv` , is used to write the efficiencies, cluster size and cluster multiplicity  
 1483       of efficiency runs. Note that `L0` refers here to *Level 0* and means that the results of efficiency and  
 1484       clusterization are a first approximation calculated without performing any muon tracking in

1485 between the different detectors. This offline tool provides the user with a preliminar calculation  
 1486 of the efficiency and of the muon event parameters. Another analysis software especially  
 1487 dedicated to muon tracking is called on selected data to retrieve the results of efficiency and  
 1488 muon clusterization using a tracking algorithm to discriminate noise or gamma from muons  
 1489 as muons are the only particles that pass through the full setup, leaving hits than can be used  
 1490 to reconstruct their tracks.

- 1491     ● `Offline-Rate.csv`, is used to write the noise or gamma rates measured in the detector readout  
 1492 partitions.

1493     Note that these 4 CSV files are created along with their *headers* (`Offline-[...]-Header.csv`  
 1494 containing the names of each data columns) and are automatically merged together when the offline  
 1495 analysis tool is called from the webDCS, contrary to the case where the tool is runned locally from  
 1496 the terminal as the merging bash script is then not called. Thus, the resulting files, used to make  
 1497 official plots, are:

- 1498         ● `Corrupted.csv`,  
 1499         ● `Current.csv`,  
 1500         ● `L0-EffCl.csv`.  
 1501         ● `Rate.csv`.

## 1502     **B.3 Analysis inputs and information handling**

1503     The usage of the Offline Analysis tool as well as its output have been presented in the previous section.  
 1504     It is now important to dig further and start looking at the source code and the inputs necessary  
 1505 for the tool to work. Indeed, other than the raw ROOT data files that are analysed, more information  
 1506 needs to be imported inside of the program to perform the analysis such as the description of the  
 1507 setup inside of GIFT++ at the time of data taking (number of trolleys, of RPCs, dimensions of the  
 1508 detectors, etc...) or the mapping that links the TDC channels to the coresponding RPC channels in  
 1509 order to translate the TDC information into human readable data. 2 files are used to transmit all this  
 1510 information:  
 1511

- 1512         ● `Dimensions.ini`, that provides the necessary setup and RPC information, and  
 1513         ● `ChannelsMapping.csv`, that gives the link between the TDC and RPC channels as well as the  
 1514         *mask* for each channel (masked or not?).

### 1515     **B.3.1 Dimensions file and InFile parser**

1516     This input file, present in every data folder, allows the analysis tool to know of the number of active  
 1517 trolleys, the number of active RPCs in those trolleys, and the details about each RPCs such as  
 1518 the number of RPC gaps, the number of pseudo-rapidity partitions (for CMS-like prototypes), the  
 1519 number of strips per partion or the dimensions. To do so, there are 3 types of groups in the INI file  
 1520 architecture. A first general group, appearing only once at the head of the document, gives information  
 1521 about the number of active trolleys as well as their IDs, as presented in Source Code B.1. For

1522 each active trolley, a group similar to Source Code B.2 can be found containing information about  
 1523 the number of active detectors in the trolley and their IDs. Each trolley group as a `Tt` name format,  
 1524 where `t` is the trolley ID. Finally, for each detector stored in slots of an active trolley, there is a group  
 1525 providing information about their names and dimensions, as shown in Source Code B.3. Each slot  
 1526 group as a `TtSs` name format, where `s` is the slot ID of trolley `t` where the active RPC is hosted.

```
1527
1528 [General]
nTrolleys=2
TrolleysID=13
```

1529 *Source Code B.1: Example of `[General]` group as might be found in `Dimensions.ini`. In Gif++, only 2  
 trolleys are available to hold RPCs and place them inside of the bunker for irradiation. The IDs of the trolleys  
 are written in a single string as "13" and then read character by character by the program.*

```
1530
1531 [T1]
nSlots=4
SlotsID=1234
```

1531 *Source Code B.2: Example of trolley group as might be found in `Dimensions.ini`. In this example, the file  
 tells that there are 4 detectors placed in the holding slots of the trolley `T1` and that their IDs, written as a single  
 string variable, are 1, 2, 3 and 4.*

```
1532
1533 [T1S1]
Name=RE2-2-NPD-BARC-8
Partitions=3
Gaps=3
Gap1=BOT
Gap2=TN
Gap3=TW
AreaGap1=11694.25
AreaGap2=6432
AreaGap3=4582.82
Strips=32
ActiveArea-A=157.8
ActiveArea-B=121.69
ActiveArea-C=93.03
```

1533 *Source Code B.3: Example of slot group as might be found in `Dimensions.ini`. In this example, the file  
 provides information about a detector named `RE2-2-NPD-BARC-8`, having 3 pseudo-rapidity readout partitions  
 and stored in slot `S1` of trolley `T1`. This is a CMS RE2-2 type of detector. This information will then be used for  
 example to compute the rate per unit area calculation.*

1534 This information is readout and stored in a C++ object called `IniFile`, that parses the information  
 1535 in the INI input file and stores it into a local buffer for later use. This INI parser is the exact same  
 1536 one that was previously developed for the Gif++ DAQ and described in Appendix A.5.2.

### 1537 B.3.2 TDC to RPC link file and Mapping

1538 The same way the INI dimension file information is stored using `map`, the channel mapping and mask  
 1539 information is stored and accessed through `map`. First of all, the mapping CSV file is organised into  
 1540 3 columns separated by tabulations (and not by commas, as expected for CSV files as it is easier using  
 1541 streams to read tab or space separated data using C++):

1542

1543      RPC\_channel            TDC\_channel            mask

1544      using as formatting for each field:

1545  
1546      TSCCC                TCCC                M

1547      TSCCC is a 5-digit integer where  $T$  is the trolley ID,  $s$  the slot ID in which the RPC is held insite  
1548      the trolley  $T$  and CCC is the RPC channel number, or *strip* number, that can take values up to  
1549      3-digits depending on the detector,

1550      TCCC is a 4 digit integer where  $T$  is the TDC ID, CCC is the TDC channel number that can take values  
1551      in between 0 and 127, and

1552      M is a 1-digit integer indicating if the channel should be considered ( $M = 1$ ) or discarded ( $M = 0$ )  
1553      during analysis.

1554      This mapping and masking information is readout and stored thanks to the object `Mapping`, pre-  
1555      sented in Source Code B.4. Similarly to `IniFile` objects, this class has private methods. The first  
1556      one, `Mapping::CheckIfNewLine()` is used to find the newline character '`\n`' or return character  
1557      '`\r`' (depending on which kind of operating system interacted with the file). This is used for the  
1558      simple reason that the masking information has been introduced only during the year 2017 but the  
1559      channel mapping files exist since 2015 and the very beginning of data taking at GIF++. This means  
1560      that in the older data folders, before the upgrade, the channel mapping file only had 2 columns, the  
1561      RPC channel and the TDC channel. For compatibility reasons, this method helps controling the  
1562      character following the readout of the 2 first fields of a line. In case any end of line character is  
1563      found, no mask information is present in the file and the default  $M = 1$  is used. On the contrary, if  
1564      the next character was a tabulation or a space, the mask information is present.

1565      Once the 3 fields have been readout, the second private method `Mapping::CheckIfTDCCh()` is  
1566      used to control that the TDC channel is an existing TDC channel. Finally, the information is stored  
1567      into 3 different maps (`Link`, `ReverseLink` and `Mask`) thanks to the public method `Mapping::Read()`.  
1568      `Link` allows to get the RPC channel by knowing the TDC channel while `ReverseLink` does the op-  
1569      posite by returning the TDC channel by knowing the RPC channel. Finally, `Mask` returns the mask  
1570      associated to a given RPC channel.

```

1571 typedef map<Uint,Uint> MappingData;

1572 class Mapping {
1573     private:
1574         bool          CheckIfNewLine(char next);
1575         bool          CheckIfTDCCh(Uint channel);
1576         string        FileName;
1577         MappingData  Link;
1578         MappingData  ReverseLink;
1579         MappingData  Mask;
1580         int           Error;
1581
1582     public:
1583         Mapping();
1584         Mapping(string baseName);
1585         ~Mapping();
1586
1587         void SetFileName(const string filename);
1588         int  Read();
1589         Uint GetLink(Uint tdcchannel);
1590         Uint GetReverse(Uint rpcchannel);
1591         Uint GetMask(Uint rpcchannel);
1592     };

```

1573 *Source Code B.4: Description of C++ object Mapping used as a parser for the channel mapping and mask file.*

## 1574 B.4 Description of GIF++ setup within the Offline Analysis tool

1575 In the previous section, the tool input files have been discussed. The dimension file information is  
 1576 stored in a map hosted by the `IniFile` object. But this information is then used to create a series of  
 1577 new objects that helps defining the GIF++ infrastructure directly into the Offline Analysis. Indeed,  
 1578 from the `RPC`, to the more general `Infrastructure`, every element of the GIF++ infrastrucutre is  
 1579 recreated for each data analysis based on the information provided in input. All this information  
 1580 about the infrastructure will be used to assign each hit signal to a specific strip channel of a specific  
 1581 detector, and having a specific active area. This way, rate per unit area calculation is possible.  
 1582

### 1583 B.4.1 RPC objects

1584 `RPC` objects have been developped to represent physical active detectors in GIF++ at the moment  
 1585 of data taking. Thus, there are as many `RPC` objects created during the analysis than there were  
 1586 active RPCs tested during a run. Each `RPC` hosts the information present in the corresponding INI  
 1587 slot group, as shown in B.3, and organises it using a similar architecture. This can be seen from  
 1588 Source B.5.

1589 To make the object more compact, the lists of gap labels, of gap active areas and strip active  
 1590 areas are stored into `vector` dynamical containers. `RPC` objects are always contructed thanks to the  
 1591 dimension file information stored into the `IniFILE` and their ID, using the format `TtSs`. Using the  
 1592 `RPC` ID, the constructor calls the methods of `IniFILE` to initialise the `RPC`. The other constructors  
 1593 are not used but exist in case of need. Finally, some getters have been written to access the different  
 1594 private parameters storing the detector information.

```

1595
class RPC{
    private:
        string      name;           //RPC name as in webDCS database
        Uint        nGaps;          //Number of gaps in the RPC
        Uint        nPartitions;    //Number of partitions in the RPC
        Uint        nStrips;         //Number of strips per partition
        vector<string> gaps;       //List of gap labels (BOT, TOP, etc...)
        vector<float>  gapGeo;        //List of gap active areas
        vector<float>  stripGeo;      //List of strip active areas

    public:
        RPC();
        RPC(string ID, IniFile* geofile);
        RPC(const RPC& other);
        ~RPC();
        RPC& operator=(const RPC& other);

        string GetName();
        Uint GetNGaps();
        Uint GetNPartitions();
        Uint GetNStrips();
        string GetGap(Uint g);
        float GetGapGeo(Uint g);
        float GetStripGeo(Uint p);
};

1596

```

<sup>1597</sup> *Source Code B.5: Description of C++ objects RPC that describe each active detectors used during data taking.*

## <sup>1598</sup> B.4.2 Trolley objects

<sup>1599</sup> Trolley objects have been developped to represent physical active trolleys in GIFT++ at the moment  
<sup>1600</sup> of data taking. Thus, there are as many trolley objects created during the analysis than there were  
<sup>1601</sup> active trolleys hosting tested RPCs during a run. Each Trolley hosts the information present in the  
<sup>1602</sup> corresponding INI trolley group, as shown in B.2, and organises it using a similar architecture. In  
<sup>1603</sup> addition to the information hosted in the INI file, these object have a dynamical container of RPC  
<sup>1604</sup> objects, representing the active detectors the active trolley was hosting at the time of data taking.  
<sup>1605</sup> This can been seen from Source Code B.6.

<sup>1606</sup> Trolley objects are always contructed thanks to the dimension file information stored into the  
<sup>1607</sup> IniFILE and their ID, using the format Tt. Using the Trolley ID, the constructor calls the methods  
<sup>1608</sup> of IniFILE to initialise the Trolley. Retrieving the information of the RPC IDs via SlotsID, a new  
<sup>1609</sup> RPC is constructed and added to the container RPCs for each character in the ID string. The other  
<sup>1610</sup> constructors are not used but exist in case of need. Finally, some getters have been written to access  
<sup>1611</sup> the different private parameters storing the trolley and detectors information.

```

1612
class Trolley{
    private:
        Uint           nSlots; //Number of active RPCs in the considered trolley
        string         SlotsID; //Active RPC IDs written into a string
        vector<RPC*> RPCs;   //List of active RPCs

    public:
        //Constructors, destructor and operator =
        Trolley();
        Trolley(string ID, IniFile* geofile);
        Trolley(const Trolley& other);
        ~Trolley();
        Trolley& operator=(const Trolley& other);

        //Get GIFTrolley members
        Uint   GetNSlots();
        string GetSlotsID();
        Uint   GetSlotID(Uint s);

        //Manage RPC list
        RPC*   GetRPC(Uint r);
        void   DeleteRPC(Uint r);

        //Methods to get members of RPC objects stored in RPCs
        string GetName(Uint r);
        Uint   GetNGaps(Uint r);
        Uint   GetNPartitions(Uint r);
        Uint   GetNStrips(Uint r);
        string GetGap(Uint r, Uint g);
        float  GetGapGeo(Uint r, Uint g);
        float  GetStripGeo(Uint r, Uint p);
    };

```

Source Code B.6: Description of C++ objects `Trolley` that describe each active trolley used during data taking.

### 1615 B.4.3 Infrastructure object

1616 The `Infrastructure` object has been developped to represent the GIFT++ bunker area dedicated to  
 1617 CMS RPC experiments. With this very specific object, all the information about the CMS RPC  
 1618 setup within GIFT++ at the moment of data taking is stored. It hosts the information present in the  
 1619 corresponding INI general group, as shown in B.1, and organises it using a similar architecture. In  
 1620 addition to the information hosted in the INI file, this object have a dynamical container of `Trolley`  
 1621 objects, representing the active tolleys in GIFT++ area. This can be seen from Source Code B.7.

1622 The `Infrastructure` object is always contructed thanks to the dimension file information stored  
 1623 into the `IniFILE`. Retrieving the information of the trolley IDs via `TrolleysID`, a new `Trolley` is  
 1624 constructed and added to the container `Trolleys` for each character in the ID `string`. By extension,  
 1625 it is easy to understand that the process described in Section B.4.2 for the construction of RPCs  
 1626 takes place when a trolley is constructed. The other constructors are not used but exist in case of  
 1627 need. Finally, some getters have been written to access the different private parameters storing the  
 1628 infrastructure, tolleys and detectors information.

```

1629 class Infrastructure {
1630     private:
1631         Uint             nTrolleys;    //Number of active Trolleys in the run
1632         string          TrolleysID;   //Active trolley IDs written into a string
1633         vector<Trolley*> Trolleys;   //List of active Trolleys (struct)
1634
1635     public:
1636         //Constructors and destructor
1637         Infrastructure();
1638         Infrastructure(IniFile* geofile);
1639         Infrastructure(const Infrastructure& other);
1640         ~Infrastructure();
1641         Infrastructure& operator=(const Infrastructure& other);
1642
1643         //Get Infrastructure members
1644         Uint  GetNTrolleys();
1645         string GetTrolleysID();
1646         Uint   GetTrolleyID(Uint t);
1647
1648         //Manage Trolleys
1649         Trolley* GetTrolley(Uint t);
1650         void    DeleteTrolley(Uint t);
1651
1652         //Methods to get members of GIFTrolley objects stored in Trolleys
1653         Uint  GetNSlots(Uint t);
1654         string GetSlotsID(Uint t);
1655         Uint   GetSlotID(Uint t, Uint s);
1656         RPC*  GetRPC(Uint t, Uint r);
1657
1658         //Methods to get members of RPC objects stored in RPCs
1659         string GetName(Uint t, Uint r);
1660         Uint   GetNGaps(Uint t, Uint r);
1661         Uint   GetNPartitions(Uint t, Uint r);
1662         Uint   GetNStrips(Uint t, Uint r);
1663         string GetGap(Uint t, Uint r, Uint g);
1664         float  GetGapGeo(Uint t, Uint r, Uint g);
1665         float  GetStripGeo(Uint t, Uint r, Uint p);
1666     };

```

*Source Code B.7: Description of C++ object Infrastructure that contains the full information about CMS RPC experiment in GIF++.*

## B.5 Handeling of data

1632 As discussed in Appendix A.4.2, the raw data as a `TTree` architecture where every entry is related to  
 1633 a trigger signal provided by a muon or a random pulse, whether the goal of the data taking was to  
 1634 measure the performance of the detector or the noise/gamma background respectively. Each of these  
 1635 entries, referred also as events, contain a more or less full list of hits in the TDC channels to which  
 1636 the detectors are connected. To this list of hits corresponds a list of time stamps, marking the arrival  
 1637 of the hits within the TDC channel.  
 1638 The infrastructure of the CMS RPC experiment within GIF++ being defined, combining the  
 1639 information about the raw data with the information provided by both the mapping/mask file and the  
 1640 dimension file allows to build new physical objects that will help in computing efficiency or rates.  
 1641

### 1642 B.5.1 RPC hits

1643 The raw data stored in the ROOT file as output of the GIFT++ DAQ, is readout by the analysis tool  
 1644 using the structure `RAWData` presented in Source Code B.9 that differs from the structure presented  
 1645 in Appendix A.4.2 as it is not meant to hold all of the data contained in the ROOT file. In this sense,  
 1646 this structure is in the case of the offline analysis tool not a dynamical object and will only be storing  
 1647 a single event contained in a single entry of the `TTree`.

```
1648
1649 class RPCHit {
1650     private:
1651         Uint Channel;      //RPC channel according to mapping (5 digits)
1652         Uint Trolley;      //0, 1 or 3 (1st digit of the RPC channel)
1653         Uint Station;      //Slot where is held the RPC in Trolley (2nd digit)
1654         Uint Strip;        //Physical RPC strip where the hit occurred (last 3
1655         →   digits)
1656         Uint Partition;    //Readout partition along eta segmentation
1657         float TimeStamp;   //Time stamp of the arrival in TDC
1658
1659     public:
1660         //Constructors, destructor & operator =
1661         RPCHit();
1662         RPCHit(Uint channel, float time, Infrastructure* Infra);
1663         RPCHit(const RPCHit& other);
1664         ~RPCHit();
1665         RPCHit& operator=(const RPCHit& other);
1666
1667         //Get RPCHit members
1668         Uint GetChannel();
1669         Uint GetTrolley();
1670         Uint GetStation();
1671         Uint GetStrip();
1672         Uint GetPartition();
1673         float GetTime();
1674     };
1675
1676     typedef vector<RPCHit> HitList;
1677     typedef struct GIFHitList { HitList rpc[NTROLLEYS][NSLOTS][NPARTITIONS]; } →
1678     →   GIFHitList;
1679
1680     bool SortHitbyStrip(RPCHit h1, RPCHit h2);
1681     bool SortHitbyTime(RPCHit h1, RPCHit h2);

```

1650 *Source Code B.8: Description of C++ object RPCHit.*

```
1651
1652     struct RAWData{
1653         int iEvent;          //Event i
1654         int TDCNHits;       //Number of hits in event i
1655         int QFlag;           //Quality flag list (1 flag digit per TDC)
1656         vector<Uint> *TDCCh; //List of channels giving hits per event
1657         vector<float> *TDCTS; //List of the corresponding time stamps
1658     };

```

1652 *Source Code B.9: Description of C++ structure RAWData.*

1653 Each member of the structure is then linked to the corresponding branch of the ROOT data tree,  
 1654 as shown in the example of Source Code B.10, and using the method `GetEntry(int i)` of the ROOT  
 1655 class `TTree` will update the state of the members of `RAWData`.

```

1656 TTree* dataTree = (TTree*)dataFile.Get("RAWData");
1657 RAWData data;
1658
1659 dataTree->SetBranchAddress("EventNumber", &data.iEvent);
1660 dataTree->SetBranchAddress("number_of_hits", &data.TDCNHits);
1661 dataTree->SetBranchAddress("Quality_flag", &data.QFlag);
1662 dataTree->SetBranchAddress("TDC_channel", &data.TDCCh);
1663 dataTree->SetBranchAddress("TDC_TimeStamp", &data.TDCTS);

```

1658       *Source Code B.10: Example of link in between RAWData and TTree.*

1659       The data is then analysed entry by entry and to each element of the TDC channel list, a `RPCHit` is  
 1660       constructed by linking each TDC channel to the corresponding RPC channel thanks to the `Mapping`  
 1661       object. The information carried by the RPC channel format allows to easily retrieve the trolley and  
 1662       slot from which the hit was recorded (see section B.3.2). Using these 2 values, the readout partition  
 1663       can be found by knowing the strip channel and comparing it with the number of partitions and strips  
 1664       per partition stored into the `Infrastructure` object.

1665       Thus `RPCHit` objects are then stored into 3D dynamical list called `GIFHitList` (Source Code B.9)  
 1666       where the 3 dimensions refer to the 3 layers of the readout in `GIF++` : in the bunker there are *trolleys*  
 1667       ( $\tau$ ) holding detectors in *slots* ( $s$ ) and each detector readout is divided into 1 or more pseudo-rapidity  
 1668       *partitions* ( $p$ ). Using these 3 information allows to assign an address to each readout partition and  
 1669       this address will point to a specific hit list.

1670

## 1671       **B.5.2 Clusters of hits**

1672       All the hits contained in the ROOT file have been sorted into the different hit lists through the  
 1673       `GIFHitList`. At this point, it is possible to start looking for clusters. A cluster is a group of adjacent  
 1674       strips getting hits within a time window of 25 ns. These strips are then assumed to be part of the same  
 1675       physical avalanche signal generated by a muon passing through the chamber or by the interaction of  
 1676       a gamma stopping into the electrodes of the RPCs.

1677       To keep the cluster information, `RPCCluster` objects have been defined as shown in Source  
 1678       Code B.11. Using the information of each individual `RPCHit` taken out of the hit list, it stores  
 1679       the cluster size (number of adjacent strips composing the cluster), the first and last hit, the center for  
 1680       spatial reconstruction and finally the start and stop time stamps as well as te time spread in between  
 1681       the first and last hit.

```

1682
class RPCCluster{
    private:
        Uint ClusterSize; //Size of cluster #ID
        Uint FirstStrip; //First strip of cluster #ID
        Uint LastStrip; //Last strip of cluster #ID
        float Center; //Center of cluster #ID ((first+last)/2)
        float StartStamp; //Time stamp of the earliest hit of cluster #ID
        float StopStamp; //Time stamp of the latest hit of cluster #ID
        float TimeSpread; //Time difference between earliest and latest hits
                           //of cluster #ID

    public:
        //Constructors, destructor & operator =
        RPCCluster();
        RPCCluster(HitList List, Uint cID, Uint cSize, Uint first, Uint firstID);
        RPCCluster(const RPCCluster& other);
        ~RPCCluster();
        RPCCluster& operator=(const RPCCluster& other);

        //Get Cluster members
        Uint GetID();
        Uint GetSize();
        Uint GetFirstStrip();
        Uint GetLastStrip();
        float GetCenter();
        float GetStart();
        float GetStop();
        float GetSpread();
};

typedef vector<RPCCluster> ClusterList;

//Other functions to build cluster lists out of hit lists
void BuildClusters(HitList &cluster, ClusterList &clusterList);
void Clusterization(HitList &hits, TH1 *hcSize, TH1 *hcMult);

```

*Source Code B.11: Description of C++ object cluster.*

To investigate the hit list of a given detector partition, the function `Clusterization()` defined in `include/Cluster.h` needs the hits in the list to be time sorted. This is achieved by calling function `sort()` of library `<algorithm>` using the comparator `SortHitbyTime(RPCHit h1, RPCHit h2)` defined in `include/RPCHit.h` that returns `true` if the time stamp of hit `h1` is lower than that of `h2`. A first isolation of strips is made only based on time information. All the hits within the 25 ns window are taken separately from the rest. Then, this sub-list of hits is sorted this time by ascending strip number, using this time the comparator `SortHitbyStrip(RPCHit h1, RPCHit h2)`. Finally, the groups of adjacent strips are used to construct `RPCCluster` objects that are then stored in a temporary list of clusters that is at the end of the process used to know how many clusters were reconstructed and to fill their sizes into an histogram that will allows to know the mean size of muon or gamma clusters.

1697 B.6 DAQ data Analysis

1698 All the ingredients to analyse GIF++ data have been defined. This section will focus on the different  
1699 part of the analysis performed on the data, from determining the type of data the tool is dealing with

<sup>1700</sup> to calculating the rate in each detector or reconstructing muon or gamma clusters.

### <sup>1701</sup> B.6.1 Determination of the run type

<sup>1702</sup> In GIF++, both the performance of the detectors in detecting muons in an irradiated environment and  
<sup>1703</sup> the gamma background can be independantly measured. These corresponds to different run types  
<sup>1704</sup> and thus, to different TDC settings giving different data to look at.

<sup>1705</sup>

<sup>1706</sup> In the case of performance measurements, the trigger for data taking is provided by the coïncidence  
<sup>1707</sup> of several scintillators when muons from the beam passing through the area are detected. Data  
<sup>1708</sup> is collected in a 600 ns wide window around the arrival of muons in the RPCs. The expected time  
<sup>1709</sup> distribution of hits is shown in Figure B.1a. The muon peak is clearly visible in the center of the  
<sup>1710</sup> distribution and is to be extracted from the gamma background that composes the flat part of the  
<sup>1711</sup> distribution.

<sup>1712</sup> On the other hand, gamma background or noise measurements are focussed on the non muon  
<sup>1713</sup> related physics and the trigger needs to be independant from the muons to give a good measurement  
<sup>1714</sup> of the gamma/noise distribution as seen by the detectors. The trigger is then provided by a pulse  
<sup>1715</sup> generator at a frequency of 300 Hz whose pulse is not likely to be on time with a muon. In order  
<sup>1716</sup> to increase the integrated time without increasing the acquisition time too much, the width of the  
<sup>1717</sup> acquisition windows are increased to 10  $\mu$ s. The time distribution of the hits is expected to be flat, as  
<sup>1718</sup> shown by Figure B.1b.

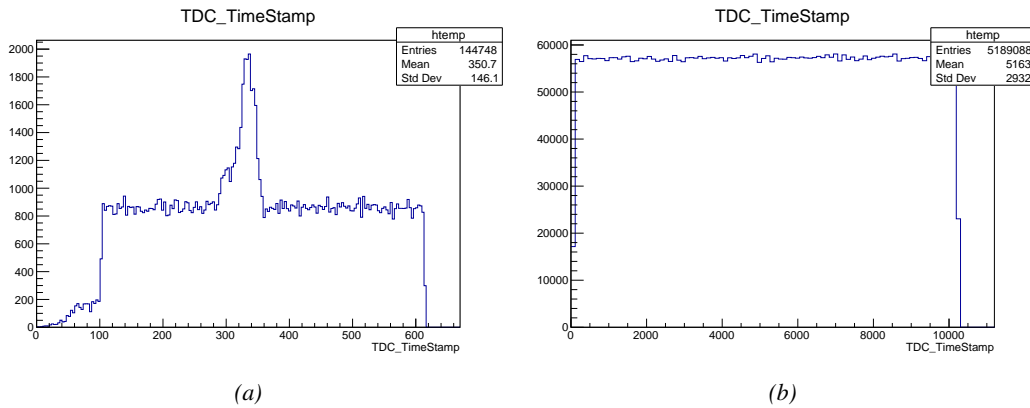


*Figure B.1: Example of expected hit time distributions in the cases of efficiency (Figure B.1a) and noise/gamma rate per unit area (Figure B.1b) measurements as extracted from the raw ROOT files. The unit along the x-axis corresponds to ns. The fact that "the" muon peak is not well defined in Figure B.1a is due to the contribution of all the RPCs being tested at the same time that don't necessarily have the same signal arrival time. Each individual peak can have an offset with the ones of other detectors. The inconsistency in the first 100 ns of both time distributions is an artefact of the TDCs and are systematically rejected during the analysis.*

<sup>1719</sup> The ROOT files include a TTree called RunParameters containing, among other things, the in-  
<sup>1720</sup> formation related to the type of run. The run type can then be accessed as described by Source  
<sup>1721</sup> Code B.12 and the function IsEfficiencyRun() is then used to determine if the run file is an effi-  
<sup>1722</sup> ciency run or, on the contrary, another type of run (noise or gamma measurement).

```

1723
1724     TTree* RunParameters = (TTree*)dataFile.Get("RunParameters");
1725     TString* RunType = new TString();
1726     RunParameters->SetBranchAddress("RunType", &RunType);
1727     RunParameters->GetEntry(0);

```

1725       *Source Code B.12: Access to the run type contained in TTree\* RunParameters.*

1726       Finally, the data files will have a slightly different content whether it was collected before or after  
1727       October 2017 and the upgrade of the DAQ software that brought a new information into the ROOT  
1728       output. This is discussed in Appendix A.4.3 and implies that the analysis will differ a little depending  
1729       on the data format. Indeed, as no information on the data quality is stored, in older data files, the cor-  
1730       rections for missing events has to be done at the end of the analysis. The information about the type  
1731       of data format is stored in the variable **bool** `isNewFormat` by checking the list of branches contained  
1732       in the data tree via the methods `TTree::GetListOfBranches()` and `TCollection::Contains()`.

### 1733     **B.6.2 Beam time window calculation for efficiency runs**

1734       Knowing the run type is important first of all to know the width of the acquisition window to be used  
1735       for the rate calculation and finally to be able to seek for muons. Indeed, the peak that appears in the  
1736       time distribution for each detectors is then fitted to extract the most probable time window in which  
1737       the tool should look for muon hits. The data outside of this time window is then used to evaluate the  
1738       noise or gamma background the detector was subjected to during the data taking. Computing the  
1739       position of the peak is done calling the function `SetBeamWindow()` defined in file `src/RPCHit.cc` that  
1740       loops a first time on the data. The data is first sorted in a 3D array of 1D histograms (`GIFH1Array`, see  
1741       `include/types.h`). Then the location of the highest bin is determined using `TH1::GetMaximumBin()`  
1742       and is used to define a window in which a gaussian fit will be applied to compute the peak width.  
1743       This window is a 80 ns defined by Formula B.1 around the central bin.

$$t_{center}(ns) = bin \times width_{bin}(ns) \quad (\text{B.1a})$$

$$[t_{low}; t_{high}] = [t_{center} - 40; t_{center} + 40] \quad (\text{B.1b})$$

1744       Before the fit is performed, the average number of noise/gamma hits per bin is evaluated using  
1745       the data outside of the fit window. Excluding the first 100 ns, the average number of hits per bin  
1746       due to the noise or gamma is defined by Formula B.2 after extracting the amount of hits in the time  
1747       windows  $[100; t_{low}]$  and  $[t_{high}; 600]$  thanks to the method `TH1::Integral()`. This average number  
1748       of hits is then subtracted to every bin of the 1D histogram, in order to *clean* it from the noise or  
1749       gamma contribution as much as possible to improve the fit quality. Bins where  $\langle n_{hits} \rangle$  is greater  
1750       than the actual bin content are set to 0.

$$\Delta t_{noise}(ns) = 600 \overbrace{-t_{high} + t_{low}}^{-80ns} - 100 = 420ns \quad (\text{B.2a})$$

$$\langle n_{hits} \rangle = width_{bin}(ns) \times \frac{\sum_{t=100}^{t_{low}} + \sum_{t=t_{high}}^{600}}{\Delta t_{noise}(ns)} \quad (\text{B.2b})$$

1751       Finally, the fit parameters are extracted and saved for each detector in 3D arrays of **float**  
1752       (`muonPeak`, see `include/types.h`), a first one for the mean arrival time of the muons, `PeakTime`,

1753 and a second one for the width of the peak, `PeakWidth`. The width is defined as  $6\sigma$  of the gaussian  
 1754 fit. The same settings are applied to every partitions of the same detector. To determine which one  
 1755 of the detector's partitions is directly illuminated by the beam, the peak height of each partition is  
 1756 compared and the highest one is then used to define the peak settings.

### 1757 **B.6.3 Data loop and histogram filling**

1758 3D arrays of histogram are created to store the data and display it on the DQM of GIF++ webDCS  
 1759 for the use of shifters. These histograms, presented in section B.2.1.1, are filled while looping on  
 1760 the data. Before starting the analysis loop, it is necessary to control the entry quality for the new  
 1761 file formats featuring `QFlag`. If the `QFlag` value for this entry shows that 1 TDC or more have a  
 1762 `CORRUPTED` flag, then this event is discarded. The loss of statistics is low enough to be neglected.  
 1763 `QFlag` is controled using the function `IsCorruptedEvent()` defined in `src/utils.cc`. As explained  
 1764 in Appendix A.4.3, each digit of this integer represent a TDC flag that can be 1 or 2. Each 2 is  
 1765 the sign of a `CORRUPTED` state. Then, the data is accessed entry by entry in the ROOT `TTree` using  
 1766 `RAWData` and each hit in the hit list is assigned to a detector channel and saved in the corresponding  
 1767 histograms. In the first part of the analysis, in which the loop over the ROOT file's content is  
 1768 performed, the different steps are:

1769 **1- RPC channel assignment and control:** a check is done on the RPC channel extracted thanks  
 1770 to the mapping via the method `Mapping::GetLink()`. If the channel is not initialised and is 0, or if  
 1771 the TDC channel was greater than 5127, the hit is discarded. This means there was a problem in the  
 1772 mapping. Often a mapping problem leads to the crash of the offline tool.

1773 **2- Creation of a `RPCHit` object:** to easily get the trolley, slot and partition in which the hit has  
 1774 been assigned, this object is particularly helpful.

1775 **3- General histograms are filled:** the hit is filled into the time distribution and the general hit  
 1776 distribution histograms, and if the arrival time is within the first 100 ns, it is discarded and nothing  
 1777 else happens and the loop proceeds with the next hit in the list.

1778 **4- Multiplicity counter:** the hit multiplicity counter of the corresponding detectors incremented.

1779 **5-a- Efficiency runs - Is the hit within the peak window? :** if the peak is contained in the peak  
 1780 window previously defined in section B.6.2, the hit is filled into the beam hit profile histogram of  
 1781 the corresponding chamber, added into the list of muon hits and increments the counter of *in time*  
 1782 hits. The term *in time* here refers to the hits that are likely to be muons by arriving in the expected  
 1783 time window. If the hit is outside of the peak window, it is filled into the noise profile histogram  
 1784 of the corresponding detector, added into the list of noise/gamma hits and increments the counter of  
 1785 noise/gamma hits.

1786 **5-b- Noise/gamma rate runs - Noise histograms are filled:** the hit is filled into the noise profile  
 1787 histogram of the corresponding detector, added into the list of noise/gamma hits and increments the  
 1788 counter of noise/gamma hits.

1790 After the loop on the hit list of the entry is over, the next step is to clusterize the 3D lists filled  
 1791 in the previous steps. A 3D loop is then started over the active trolley, slot and RPC partitions to  
 1792 access these objects. Each `NoiseHitList` and `MuonHitList`, in case of efficiency run, are clusterized  
 1793 as described in section B.5.2. There corresponding cluster size and multiplicity histograms are filled  
 1794 at the end of the clustering process. Then, the efficiency histogram is filled in case of efficiency run.  
 1795 The selection is simply made by checking whether the RPC detected signals in the peak window  
 1796 during this event. Nevertheless, it is useful to highlight that at this level, it is not possible yet to  
 1797 discriminate in between a muon hit and noise or gamma hit. Thus, `MuonCSize_H`, `MuonCMult_H`  
 1798 and `Efficiency0_H` are subjected to noise and gamma contamination. This contamination will be  
 1799 estimated and corrected at the moment the results will be written into output CSV files. Finally, the  
 1800 loop ends on the filling of the general hit multiplicity histogram.

#### 1801 **B.6.4 Results calculation**

1802 As mentioned in section B.2.1, the analysis of DAQ data provides the user with 3 CSV files and  
 1803 a ROOT file associated to each and every ROOT data file. The fourth CSV file is provided by the  
 1804 extraction of the CEAN main frame data monitored during data taking and will be discussed later.  
 1805 After looping on the data in the previous part of the analysis macro, the output files are created and a  
 1806 3D loop on each RPC readout partitions is started to extract the histograms parameters and compute  
 1807 the final results.

1808

##### 1809 **B.6.4.1 Rate normalisation**

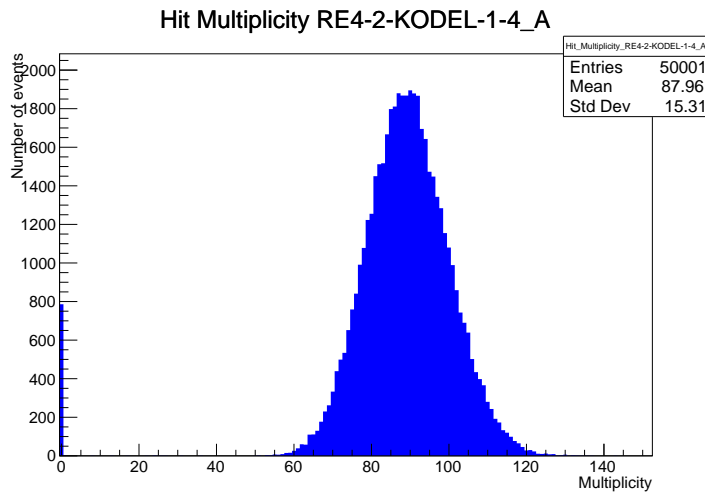


Figure B.2: The effect of the quality flag is explained by presenting the reconstructed hit multiplicity of a data file without `Quality_flag`. The artificial high content of bin 0 is the effect of corrupted data.

1810 To analyse old data format files, not containing any quality flag, it is needed to estimate the amount  
 1811 of corrupted data via a fit as the corrupted data will always fill events with a fake "0 multiplicity".  
 1812 Indeed, as no hits were stored in the DAQ ROOT files, these events artificially contribute to fill  
 1813 the bin corresponding to a null multiplicity, as shown in Figure B.2. In the case the mean of the

hit multiplicity distribution is high, the contribution of the corrupted data can easily be evaluated for later correction by comparing the level of the bin at multiplicity 0 and of a skew fit curve that should indicate a value consistent with 0. A skew fit has been chosen over a Poisson fit as it was giving better results for lower mean multiplicity values. Nevertheless, for low irradiation cases, as explained in Appendix A.4.3, the hit multiplicity distribution mean is, on the contrary, rather small and the probability to record events without hits can't be considered small anymore, leading to a difficult and non-reliable estimation of the corruption. As can be seen in Source Code B.13, conditions have been applied to prevent bad fits and wrong corruption estimation in cases where :

- The difference in between the data for multiplicity 1 and the corresponding fit value should be lower than 1% of the total amount of data :  $\frac{|n_{m=1} - sk(1)|}{N_{tot}} < 0.01$  where  $n_{m=1}$  is the number of entries with multiplicity 1,  $sk(1)$  the value of the skew fit, as defined by Formula 5.3, for multiplicity 1 and  $N_{tot}$  the total number of entries.

- The amount of data contained in the multiplicity 0 bin should not exceed 40% :  $\frac{n_{m=0}}{N_{tot}} \leq 0.4$  where  $n_{m=0}$  is the number of entries with multiplicity 0. This number has been determined to be the maximum to be able to separate the excess of data due to corruption from the hit multiplicity distribution.

Those 2 conditions need to be fulfilled to estimate the corruption of old data format files. If the fit was successful, the level of corruption is written in `Offline-Corrupted.csv` and the number of corrupted entries, refered as the integer `nEmptyEvent`, is subtracted from the total number of entries when the rate normalisation factor is computed as explicit in Source Code B.13. Note that for new data format files, the number of corrupted entries being set to 0, the definition of `rate_norm` stays valid.

```

1836 if(!isNewFormat){
    TF1* GaussFit = new TF1("gaussfit","[0]*exp(-0.5*((x-[1])/[2])**2)",0,Xmax);
    GaussFit->SetParameter(0,100);
    GaussFit->SetParameter(1,10);
    GaussFit->SetParameter(2,1);
    HitMultiplicity_H.rpc[T][S][p]->Fit(GaussFit,"LIQR","",0.5,Xmax);

    TF1* SkewFit = new TF1("skewfit","[0]*exp(-0.5*((x-[1])/[2])**2) / (1 +
→ exp(-[3]*(x-[4])))",0,Xmax);
    SkewFit->SetParameter(0,GaussFit->GetParameter(0));
    SkewFit->SetParameter(1,GaussFit->GetParameter(1));
    SkewFit->SetParameter(2,GaussFit->GetParameter(2));
    SkewFit->SetParameter(3,1);
    SkewFit->SetParameter(4,1);
    HitMultiplicity_H.rpc[T][S][p]->Fit(SkewFit,"LIQR","",0.5,Xmax);

    double fitValue = SkewFit->Eval(1,0,0,0);
    double dataValue = (double)HitMultiplicity_H.rpc[T][S][p]->GetBinContent(2);
    double difference = TMath::Abs(dataValue - fitValue);
    double fitTOdataVSentries_ratio = difference / (double)nEntries;
    bool isFitGOOD = fitTOdataVSentries_ratio < 0.01;

1837     double nSinglehit = (double)HitMultiplicity_H.rpc[T][S][p]->GetBinContent(1);
     double lowMultRatio = nSinglehit / (double)nEntries;
     bool isMultLOW = lowMultRatio > 0.4;

     if(isFitGOOD && !isMultLOW){
         nEmptyEvent = HitMultiplicity_H.rpc[T][S][p]->GetBinContent(1);
         nPhysics = (int)SkewFit->Eval(0,0,0,0);
         if(nPhysics < nEmptyEvent)
             nEmptyEvent = nEmptyEvent-nPhysics;
     }
 }

double corrupt_ratio = 100.*(double)nEmptyEvent / (double)nEntries;
outputCorrCSV << corrupt_ratio << '\t';

float rate_norm = 0.;
float stripArea = GIFIInfra->GetStripGeo(tr,sl,p);

if(IsEfficiencyRun(RunType)){
    float noiseWindow = BMTDCWINDOW - TIMEREJECT - 2*PeakWidth.rpc[T][S][p];
    rate_norm = (nEntries-nEmptyEvent)*noiseWindow*1e-9*stripArea;
} else
    rate_norm = (nEntries-nEmptyEvent)*RDMNOISEWDW*1e-9*stripArea;

```

*Source Code B.13: Definition of the rate normalisation variable. It takes into account the number of non corrupted entries and the time window used for noise calculation, to estimate the total integrated time, and the strip active area to express the result as rate per unit area.*

#### 1839 B.6.4.2 Rate and activity

1840 At this point, the strip rate histograms, StripNoiseProfile\_H.rpc[T][S][p], only contain an in-  
 1841 formation about the total number of noise or rate hits each channel received during the data taking.  
 1842 As described in Source Code B.14, a loop on the strip channels will be used to normalise the content  
 1843 of the rate distribution histogram for each detector partitions. The initial number of hits recorded for  
 1844 a given bin will be extracted and 2 values will be computed:

- 1845     ● the strip rate, defined as the number of hits recorded in the bin normalised like described in  
 1846               the previous section, using the variable `rate_norm`, and

- 1847     ● the strip activity, defined as the number of hits recorded in the bin normalised to the average  
 1848               number of hits per bin contained in the partition histogram, using the variable `averageNhit`.  
 1849               This value provides an information on the homogeneity of the detector response to the gamma  
 1850               background or of the detector noise. An activity of 1 corresponds to an average response.  
 1851               Above 1, the channel is more active than the average and bellow 1, the channel is less active.

```

int nNoise = StripNoiseProfile_H.rpc[T][S][p]->GetEntries();
float averageNhit = (nNoise>0) ? (float)(nNoise/nStripsPart) : 1.;

for(Uint st = 1; st <= nStripsPart; st++){
    float stripRate =
        StripNoiseProfile_H.rpc[T][S][p]->GetBinContent(st)/rate_norm;
    float stripAct =
        StripNoiseProfile_H.rpc[T][S][p]->GetBinContent(st)/averageNhit;

    StripNoiseProfile_H.rpc[T][S][p]->SetBinContent(st,stripRate);
    StripActivity_H.rpc[T][S][p]->SetBinContent(st,stripAct);
}

```

1853     *Source Code B.14: Description of the loop that allows to set the content of each strip rate and strip activity  
 channel for each detector partition.*

1854     On each detector partitions, which are readout by a single FEE, all the channels are not processed  
 1855     by the same chip. Each chip can give a different noise response and thus, histograms using a chip  
 1856     binning are used to investigate chip related noise behaviours. The average values of the strip rate  
 1857     or activity grouped into a given chip are extracted using the using the function `GetChipBin()` and  
 1858     stored in dedicated histograms as described in Source Codes B.15 and B.16 respectively.

```

float GetChipBin(TH1* H, Uint chip){
    Uint start = 1 + chip*NSTRIPSCHIP;
    int nActive = NSTRIPSCHIP;
    float mean = 0.;

    for(Uint b = start; b <= (chip+1)*NSTRIPSCHIP; b++){
        float value = H->GetBinContent(b);
        mean += value;
        if(value == 0.) nActive--;
    }

    if(nActive != 0) mean /= (float)nActive;
    else mean = 0.;

    return mean;
}

```

1861     *Source Code B.15: Function used to compute the content of a bin for an histogram using chip binning.*

```

1862   for(UInt ch = 0; ch < (nStripsPart/NSTRIPSCHIP); ch++) {
1863     ChipMeanNoiseProf_H.rpc[T][S][p]->
1864       SetBinContent(ch+1,GetChipBin(StripNoiseProfile_H.rpc[T][S][p],ch));
1865     ChipActivity_H.rpc[T][S][p]->
1866       SetBinContent(ch+1,GetChipBin(StripActivity_H.rpc[T][S][p],ch));
1867   }

```

*Source Code B.16: Description of the loop that allows to set the content of each chip rate and chip activity bins for each detector partition knowing the information contained in the corresponding strip distribution histograms.*

The activity variable is used to evaluate the homogeneity of the detector response to background or of the detector noise. The homogeneity  $h_p$  of each detector partition can be evaluated using the formula  $h_p = \exp(-\sigma_p^R / \langle R \rangle_p)$ , where  $\langle R \rangle_p$  is the partition mean rate and  $\sigma_p^R$  is the rate standard deviation calculated over the partition channels. The more homogeneously the rates are distributed and the smaller will  $\sigma_p^R$  be, and the closer to 1 will  $h_p$  get. On the contrary, if the standard deviation of the channel's rates is large,  $h_p$  will rapidly get to 0. This value is saved into histograms as shown in Source Code B.17 and could in the future be used to monitor through time, once extracted, the evolution of every partition homogeneity. This could be of great help to understand the apparition of eventual hot spots due to ageing of the chambers subjected to high radiation levels. The monitored homogeneity information could then be combined with a monitoring of the activity of each individual channel in order to have a finer information. Monitoring tools have been suggested and need to be developed for this purpose.

```

1876   float MeanPartSDev = GetTH1StdDev(StripNoiseProfile_H.rpc[T][S][p]);
1877   float strip_homog = (MeanPartRate==0)
1878     ? 0.
1879     : exp(-MeanPartSDev/MeanPartRate);
1880   StripHomogeneity_H.rpc[T][S][p]->Fill("exp -#left(#frac{\#sigma_{Strip}
1881     \rightarrow Rate}{\#mu_{Strip Rate}}\#right)",strip_homog);
1882   StripHomogeneity_H.rpc[T][S][p]->GetYaxis()->SetRangeUser(0.,1.);
1883
1884   float ChipStDevMean = GetTH1StdDev(ChipMeanNoiseProf_H.rpc[T][S][p]);
1885   float chip_homog = (MeanPartRate==0)
1886     ? 0.
1887     : exp(-ChipStDevMean/MeanPartRate);
1888   ChipHomogeneity_H.rpc[T][S][p]->Fill("exp -#left(#frac{\#sigma_{Chip}
1889     \rightarrow Rate}{\#mu_{Chip Rate}}\#right)",chip_homog);
1890   ChipHomogeneity_H.rpc[T][S][p]->GetYaxis()->SetRangeUser(0.,1.);

```

*Source Code B.17: Storage of the homogeneity into dedicated histograms.*

#### 1879 B.6.4.3 Strip masking tool

The offline tool is automatically called at the end of each data taking to analyse the data and offer the shifter DQM histograms to control the data quality. After the histograms have been published online in the DQM page, the shifter can decide to mask noisy or dead channels that will contribute to bias the final rate calculation by editing the mask column of `ChannelsMapping.csv` as can be seen in Figure B.3.

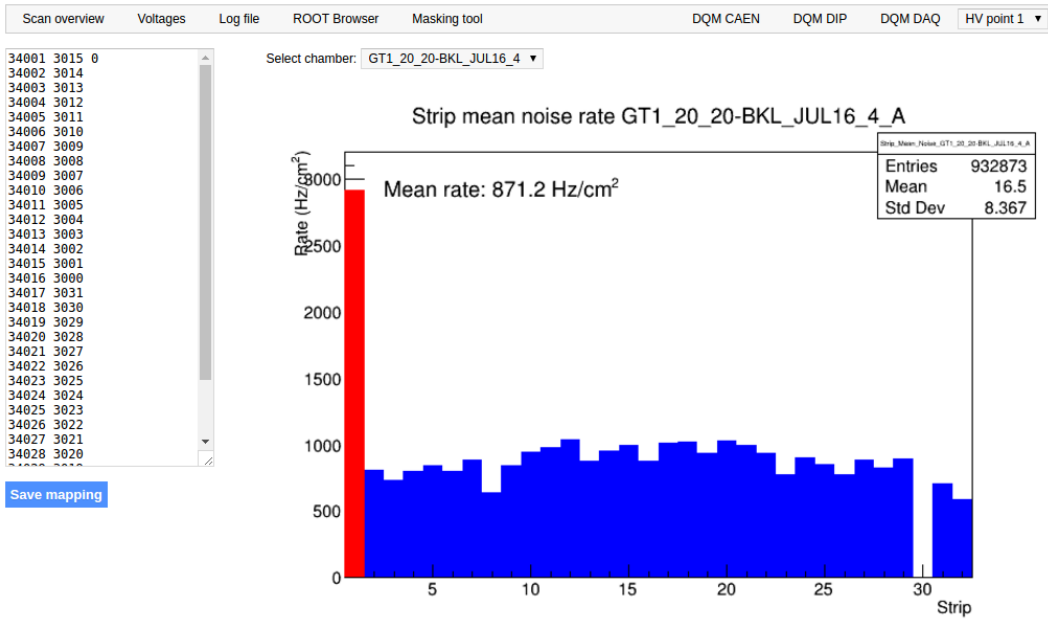


*Figure B.3: Display of the masking tool page on the webDCS. The window on the left allows the shifter to edit ChannelsMapping.csv. To mask a channel, it only is needed to set the 3rd field corresponding to the strip to mask to 0. It is not necessary for older mapping file formats to add a 1 for each strip that is not masked as the code is versatile and the default behaviour is to consider missing mask fields as active strips. The effect of the mask is directly visible for noisy channels as the corresponding bin turns red. The global effect of masking strips will be an update of the rate value showed on the histogram that will take into consideration the rejected channels.*

1885 From the code point of view, the function `GetTH1Mean()` is used to retrieve the mean rate par-  
 1886 tition by partition after the rates have been calculated strip by strip and filled into the histograms  
 1887 `StripNoiseProfile_H.rpc[T][S][p]`, as described through Source Code B.18.

1888 Once the mask for each rejected channel has been updated, the shifter can manually run the of-  
 1889 fline tool again to update the DQM plots, now including the masked strips, as well the rate results  
 1890 written in the output CSV file `Offline-Rate.csv`. If not done during the shifts, the strip masking  
 1891 procedure needs to be carefully done by the person in charge of data analysis on the scans that were  
 1892 selected to produce the final results.

```

1893   float GetTH1Mean(TH1* H) {
1894     int nBins = H->GetNbinsX();
1895     int nActive = nBins;
1896     float mean = 0.;
1897
1898     for(int b = 1; b <= nBins; b++) {
1899       float value = H->GetBinContent(b);
1900       mean += value;
1901       if(value == 0.) nActive--;
1902     }
1903
1904     if(nActive != 0) mean /= (float)nActive;
1905     else mean = 0.;
1906
1907     return mean;
1908   }

```

*Source Code B.18: The function `GetTH1Mean()` is used to return the mean along the y-axis of `TH1` histograms containing rate information. In order to take into account masked strips whose rate is set to 0, the function looks for masked channels and decrement the number of active channels for each null value found.*

#### 1896 B.6.4.4 Output CSV files filling

1897 All the histograms have been filled. Parameters will then be extracted from them to compute the  
 1898 final results that will later be used to produce plots. Once the results have been computed, the very  
 1899 last step of the offline macro is to write these values into the corresponding CSV outputs. Aside of  
 1900 the file `Offline-Corrupted.csv`, 2 CSV files are being written by the macro `offlineAnalysis()`,  
 1901 `Offline-Rates.csv` and `Offline-L0-EffCl.csv` that respectively contain information about noise  
 1902 or gamma rates, cluster size and multiplicity, and about level 0 reconstruction of the detector effi-  
 1903 ciency, muon cluster size and multiplicity. Details on the computation and file writing are respec-  
 1904 tively given in Sources Codes B.19 and B.20.

1905 **Noise/gamma background variables** are computed and written in the output file for each detector  
 1906 partitions. A detector average of the hit and cluster rate is also provided, as shown through Sources  
 1907 Code B.19. The variables that are written for each partition are:

- 1908 • The mean partition hit rate per unit area, `MeanPartRate`, that is extracted from the histogram  
 1909 `StripNoiseProfile_H` as the mean value along the y-axis, as described in section B.6.4.3. No  
 1910 error is recorded for the hit rate as this is considered a single measurement. No statistical error  
 1911 can be associated to it and the systematics are unknown.
- 1912 • The mean cluster size, `cSizePart`, is extracted from the histogram `NoiseCSize_H` and it's  
 1913 statistical error, `cSizePartErr`, is taken to be  $2\sigma$  of the total distribution.
- 1914 • The mean cluster multiplicity per trigger, `cMultPart`, is extracted from the histogram `NoiseCMult_H`  
 1915 and it's statistical error, `cMultPartErr`, is taken to be  $2\sigma$  of the total distribution. It is impor-  
 1916 tant to point to the fact that this variable gives an information that is dependent on the buffer  
 1917 window width used for each trigger for the calculation.
- 1918 • The mean cluster rate per unit area, `ClustPartRate`, is defined as the mean hit rate normalised

1919 to the mean cluster size and it's statistical error, `ClustPartRateErr`, is then obtained using the  
 1920 relative statistical error on the mean cluster size.

```

for (UInt tr = 0; tr < GIFInfra->GetNTrolleys(); tr++) {
    UInt T = GIFInfra->GetTrolleyID(tr);

    for (UInt sl = 0; sl < GIFInfra->GetNSlots(tr); sl++) {
        UInt S = GIFInfra->GetSlotID(tr,sl) - 1;

        float MeanNoiseRate = 0.;
        float ClusterRate = 0.;
        float ClusterSDev = 0.;

        for (UInt p = 0; p < GIFInfra->GetNPartitions(tr,sl); p++) {
            float MeanPartRate = GetTH1Mean(StripNoiseProfile_H.rpc[T][S][p]);
            float cSizePart = NoiseCSize_H.rpc[T][S][p]->GetMean();
            float cSizePartErr = (NoiseCSize_H.rpc[T][S][p]->GetEntries()==0)
                ? 0.
                : 2*NoiseCSize_H.rpc[T][S][p]->GetStdDev() /
                    sqrt(NoiseCSize_H.rpc[T][S][p]->GetEntries());
            float cMultPart = NoiseCMult_H.rpc[T][S][p]->GetMean();
            float cMultPartErr = (NoiseCMult_H.rpc[T][S][p]->GetEntries()==0)
                ? 0.
                : 2*NoiseCMult_H.rpc[T][S][p]->GetStdDev() /
                    sqrt(NoiseCMult_H.rpc[T][S][p]->GetEntries());
            float ClustPartRate = (cSizePart==0) ? 0.
                : MeanPartRate/cSizePart;
            float ClustPartRateErr = (cSizePart==0) ? 0.
                : ClustPartRate * cSizePartErr/cSizePart;

            outputRateCSV << MeanPartRate << '\t'
                << cSizePart << '\t' << cSizePartErr << '\t'
                << cMultPart << '\t' << cMultPartErr << '\t'
                << ClustPartRate << '\t' << ClustPartRateErr << '\t';

            RPCarea += stripArea * nStripsPart;
            MeanNoiseRate += MeanPartRate * stripArea * nStripsPart;
            ClusterRate += ClustPartRate * stripArea * nStripsPart;
            ClusterSDev += (cSizePart==0)
                ? 0.
                : ClusterRate*cSizePartErr/cSizePart;
        }

        MeanNoiseRate /= RPCarea;
        ClusterRate /= RPCarea;
        ClusterSDev /= RPCarea;

        outputRateCSV << MeanNoiseRate << '\t'
            << ClusterRate << '\t' << ClusterSDev << '\t';
    }
}

```

1922 *Source Code B.19: Description of rate result calculation and writing into the CSV output Offline-Rate.csv. Are saved into the file for each detector, the mean partition rate, cluster size and cluster mutiplicity, along with their errors, for each partition and as well as a detector average.*

1923 **Muon performance variables** are computed and written in the output file for each detector parti-  
 1924 tions as shown through Sources Code B.20. The variables that are written for each partition are:

- 1925     • The muon efficiency, `eff`, extracted from the histogram `Efficiency0_H`. It is reminded that  
1926       this offline tool doesn't include any tracking algorithm to identify muons from the beam and  
1927       only relies on the hits arriving in the time window corresponding to the beam time. The con-  
1928       tent of the efficiency histogram is thus biased by the noise/gamma background contribution  
1929       into this window and is thus corrected by estimating the muon data content in the peak re-  
1930       gion knowing the noise/gamma content in the rate calculation region. Both time windows  
1931       being different, the choice was made to normalise the noise/gamma background calculation  
1932       window to it's equivalent beam window in order to have comparable values using the variable  
1933       `windowRatio`. Finally, to estimate the data ratio in the peak region, the variable `DataRatio`  
1934       is defined as the ratio in between the estimated mean cluster multiplicity of the muons in the  
1935       peak region, `MuonCM`, and of the total mean cluster multiplicity in the peak region, `PeakCM`.  
1936       `MuonCM` is itself defined as the difference in between the total mean cluster multiplicity in the  
1937       peak region and the normalised mean noise/gamma cluster multiplicity calculated outside of  
1938       the peak region. The statistical error related to the efficiency, `eff_err`, is computed using a  
1939       binomial distribution, as the efficiency measure the probability of "success" and "failure" to  
1940       detect muons.
- 1941     • The mean muon cluster size, `MuonCS`, is calculated using the total mean cluster size and multi-  
1942       plicity in the peak region, respectively extracted from histograms `MuonCSize_H` and `MuonCMult_H`,  
1943       the noise/gamma background mean cluster size and normalised multiplicity, extracted from  
1944       `NoiseCSize_H` and `NoiseCMult_H`, and of the estimated muon cluster multiplicity `MuonCM` pre-  
1945       viously explicated. The associated statistical error, `MuonCM_err`, is calculated using the propa-  
1946       gation of errors of the mentioned variables.
- 1947     • The mean muon cluster multiplicity in the peak region, `MuonCM`, explicated above whose sta-  
1948       tistical error, `MuonCM_err`, is the sum of statistical error associated to the total mean clus-  
1949       ter multiplicity in the peak reagion, `PeakCM_err`, and of the mean noise/gamma cluster size,  
1950       `NoiseCM_err`.

1951       In addition to these 2 CSV files, the histograms are saved in ROOT file `Scan00XXXX_HVY_Offline.root`  
1952       as explained in section B.2.1.1.

1953

```

for (UInt tr = 0; tr < GIFInfra->GetNTrolleys(); tr++) {
    UInt T = GIFInfra->GetTrolleyID(tr);
    for (UInt sl = 0; sl < GIFInfra->GetNSlots(tr); sl++) {
        UInt S = GIFInfra->GetSlotID(tr,sl) - 1;
        for (UInt p = 0; p < GIFInfra->GetNPartitions(tr,sl); p++) {
            float noiseWindow =
                BMTDCWINDOW - TIMEREJECT - 2*PeakWidth.rpc[T][S][p];
            float peakWindow = 2*PeakWidth.rpc[T][S][p];
            float windowRatio = peakWindow/noiseWindow;

            float PeakCM = MuonCMult_H.rpc[T][S][p]->GetMean();
            float PeakCS = MuonCSize_H.rpc[T][S][p]->GetMean();
            float NoiseCM = NoiseCMult_H.rpc[T][S][p]->GetMean() *windowRatio;
            float NoiseCS = NoiseCSize_H.rpc[T][S][p]->GetMean();
            float MuonCM = (PeakCM<NoiseCM) ? 0. : PeakCM-NoiseCM;
            float MuonCS = (MuonCM==0 || PeakCM*PeakCS<NoiseCM*NoiseCS)
                ? 0.
                : (PeakCM*PeakCS-NoiseCM*NoiseCS) / MuonCM;
            float PeakCM_err = (MuonCMult_H.rpc[T][S][p]->GetEntries()==0.)
                ? 0.
                : 2*MuonCMult_H.rpc[T][S][p]->GetStdDev() /
                    sqrt(MuonCMult_H.rpc[T][S][p]->GetEntries());
            float PeakCS_err = (MuonCSize_H.rpc[T][S][p]->GetEntries()==0.)
                ? 0.
                : 2*MuonCSize_H.rpc[T][S][p]->GetStdDev() /
                    sqrt(MuonCSize_H.rpc[T][S][p]->GetEntries());
            float NoiseCM_err = (NoiseCMult_H.rpc[T][S][p]->GetEntries()==0.)
                ? 0.
                : windowRatio*2*NoiseCMult_H.rpc[T][S][p]->GetStdDev() /
                    sqrt(NoiseCMult_H.rpc[T][S][p]->GetEntries());
            float NoiseCS_err = (NoiseCSize_H.rpc[T][S][p]->GetEntries()==0.)
                ? 0.
                : 2*NoiseCSize_H.rpc[T][S][p]->GetStdDev() /
                    sqrt(NoiseCSize_H.rpc[T][S][p]->GetEntries());
            float MuonCM_err = (MuonCM==0) ? 0. : PeakCM_err+NoiseCM_err;
            float MuonCS_err = (MuonCS==0 || MuonCM==0) ? 0.
                : (PeakCS*PeakCM_err + PeakCM*PeakCS_err +
                    NoiseCS*NoiseCM_err + NoiseCM*NoiseCS_err +
                    MuonCS*MuonCM_err) / MuonCM;

            float DataRatio = MuonCM/PeakCM;
            float DataRatio_err = (MuonCM==0) ? 0.
                : DataRatio*(MuonCM_err/MuonCM + PeakCM_err/PeakCM);
            float eff = DataRatio*Efficiency0_H.rpc[T][S][p]->GetMean();
            float eff_err = DataRatio*2*Efficiency0_H.rpc[T][S][p]->GetStdDev() /
                sqrt(Efficiency0_H.rpc[T][S][p]->GetEntries()) +
                Efficiency0_H.rpc[T][S][p]->GetMean()*DataRatio_err;

            outputEffCSV << eff << '\t' << eff_err << '\t'
                << MuonCS << '\t' << MuonCS_err << '\t'
                << MuonCM << '\t' << MuonCM_err << '\t';
        }
    }
}

```

1954

*Source Code B.20: Description of efficiency result calculation and writing into the CSV output Offline-L0-EffCl.csv. Are saved into the file for each detector, the efficiency, corrected taking into account the background in the peak window of the time profile, muon cluster size and muon cluster multiplicity, along with their errors, for each partition and as well as a detector average.*

1955

## 1956 B.7 Current data Analysis

1957 Detectors under test at GIF++ are connected both to a CAEN HV power supply and to a CAEN  
1958 ADC that reads the currents inside of the RPC gaps bypassing the supply cable. During data tak-  
1959 ing, the webDCS records into a ROOT file called `Scan00XXXX_HVY_CAEN.root` histograms with the  
1960 monitored parameters of both CAEN devices. Are recorded for each RPC channels (in most cases,  
1961 a channel corresponds to an RPC gap):

- 1962 • the effective voltage,  $HV_{eff}$ , set by the webDCS using the PT correction on the CAEN power  
1963 supply,
- 1964 • the applied voltage,  $HV_{app}$ , monitored by the CAEN power supply, and the statistical error  
1965 related to the variations of this value through time to follow the variation of the environmental  
1966 parameters defined as the RMS of the histogram divided by the square root of the number of  
1967 recorded points,
- 1968 • the monitored current,  $I_{mon}$ , monitored by the CAEN power supply, and the statistical error  
1969 related to the variations of this value through time to follow the variation of the environmental  
1970 parameters defined as the RMS of the histogram divided by the square root of the number of  
1971 recorded points,
- 1972 • the corresponding current density,  $J_{mon}$ , defined as the monitored current per unit area,  
1973  $J_{mon} = I_{mon}/A$ , where  $A$  is the active area of the corresponding gap,
- 1974 • the ADC current,  $I_{ADC}$ , recorded through the CAEN ADC module that monitors the dark  
1975 current in the gap itself. First of all, the resolution of such a module is better than that of  
1976 CAEN power supplies and moreover, the current is not read-out through the HV supply line  
1977 but directly at the chamber level giving the real current inside of the detector. The statistical  
1978 error is defined as the RMS of the histogram distribution divided by the square root of the  
1979 number of recorded points.

1980 Once extracted through a loop over the element of GIF++ infrastructure via the C++ macro  
1981 `GetCurrent()`, these parameters, organised in 9 columns per detector HV supply line, are written in  
1982 the output CSV file `Offline-Current.csv`. The macro can be found in the file `Current.cc`.